To the Graduate Council:

I am submitting herewith a dissertation written by Kirk Townsend Lowe entitled "Direct Cooled Ceramic Substrate for Thermal Control of Automotive Power Electronics." I have examined the final electronic copy of this dissertation for form and content and recommend that it be accepted in partial fulfillment of the requirements for the degree of Doctor of Philosophy, with a major in Mechanical Engineering.

Rao V. Arimilli, Major Professor

We have read this dissertation
and recommend its acceptance:

Jay Frankel

Majid Keyhani

Leon Tolbert

Acceptance for the Council

Carolyn R. Hodges
Vice Provost and Dean of the Graduate School

(Original signatures are on file with official student records.)

Direct Cooled Ceramic Substrate for Thermal Control of Automotive Power Electronics

A Dissertation
Presented for the
Doctor of Philosophy
Degree
The University of Tennessee, Knoxville

Kirk Townsend Lowe
December 2009

Acknowledgments

I would like to thank the staff at the Power Electronics and Electric Machinery Research Center at Oak Ridge National Laboratory (ORNL) for their support in my research endeavors over the past five years. I would especially like to recognize Randy Wiles, Curt Ayers, and Chester Coomer who have sponsored much of my research support.

I would also like to acknowledge Dr. Rao Arimilli and Dr. Leon Tolbert. Dr. Arimilli has provided guidance in my academic endeavors and professional development since my undergraduate degree. Dr. Tolbert played a crucial role in providing the opportunity for me to work in association with Oak Ridge National Laboratory. Special thanks are extended to Dr. Majid Keyhani and Dr. Jay Frankel for serving on my dissertation committee.

This work was funded by Oak Ridge National Laboratory through the Vehicle Technologies Program under the Department of Energy's FreedomCAR program.

Abstract

As electric vehicle technology develops, manufacturers would like to move toward hotter coolants for power electronic components to reduce system level costs. Thus, unique designs of inverter designs were sought to enable operation with 105°C coolant. The proposed solution in this research incorporated flow channels into the ceramic layer of the direct-bonded copper substrate typically found in power electronic packages. The focus of this research details the design and analysis of the direct cooled ceramic substrate from the perspective of its thermal performance and innovative packaging concept.

The research was directed to pursue alumina as the substrate ceramic because of its low cost. Alumina, which has the lowest thermal conductivity among four materials considered, requires a larger substrate cross-sectional area to result in a viable design. Based on preliminary model parameters, two flow channel designs with larger alumina substrates were shown to meet the design goals. Experiments were conducted to characterize the pressure drop across metal foam inserts which were used to enhance the heat transfer in the flow channels. Other experiments were conducted to validate the thermal performance and model configuration. The results of thermal validation experiment showed that the assumed effective thermal conductivity of the metal foam – fluid matrix was too large. The small contact area between the metal foam inserts and ceramic substrate reduces the effective thermal conductivity.

Based on the data reduction method, the model parameters were modified to produce temperature distributions that better reflected the experimental data. Simulations were updated with the modified model parameters. These models showed that the cross-sectional area of the alumina substrate had to increase further in order to adequately manage the heat load.

In parallel efforts, the overall inverter package was considered. A linear manifold package resulted in the highest power density. Technical review of the inverter package raised concerns about stray inductance. Incorporating the entire inverter leg on one

substrate would alleviate these losses. Future research can use the parameters determined in this work to more confidently predict the performance of direct cooled ceramic substrate designs.

Table of Contents

List of Figures

List of Tables

Nomenclature

A	area
a	rectangular duct width
a	electrical phase
AC	alternating-current
AlN	aluminum nitride
b	rectangular duct height
b	electrical phase
BeO	beryllium oxide
C_f	Forchheimer drag coefficient
c	electrical phase
c_1	empirical constant
c_p	specific heat capacity
D	diameter of duct
D_h	hydraulic diameter of duct
DBC	direct bonded copper
DC	direct-current
DMM	digital multimeter
d_p	pore diameter
EMI	electromagnetic interference
$f_{F,app}$	apparent friction factor for developing flow
f_{FP}	Poiseuille friction factor = $16/Re_D$
f_κ	friction factor based on permeability = $-\nabla p\sqrt{\kappa}/\rho u^2$
FEA	finite element analysis
Gz	Graetz number = $Re_D Pr/(x/D)$
HEV	hybrid electric vehicle
H	depth of rectangular duct
h	heat transfer coefficient
I	current

$\mathbf{I}$	identity matrix
i	data index
IC	integrated circuit
ICE	internal combustion engine
IGBT	insulated gate bipolar transistor
$i(t)$	time dependent current
K_∞	empirical constant
k	thermal conductivity
L	length of duct
$\dot{m}$	mass flow rate
Nu	Nusselt number = hD/k
NREL	National Renewable Energy Laboratory
n	neutral
OEM	original equipment manufacturer
P	perimeter
P	power
PHEV	plug-in hybrid electric vehicle
PWM	pulse width modulation
Pr	Prandtl number = $\mu c_p/k$
p	pressure
p_0	initial pressure
p_x	pressure at duct length x
Q	volumetric flow rate
Q'''	volumetric heat generation
q	heat transfer rate
q'	heat transfer per unit length
q''	heat transfer per unit area
R	correlation coefficient
R_{conv}	convective thermal resistance
RMR	rotameter scale reading

r	radius
Re_D	Reynolds number based on diameter = $\rho uD/\mu$
Re_{pm}	Reynolds number for porous media = $\rho u C_f \sqrt{\kappa}\,/\mu$
s1	normalized length scale
s2	normalized length scale
S	conduction shape factor
SiC	silicon carbide
T	temperature
T_1	temperature of duct
T_2	temperature of ground
T_s	surface temperature
T_∞	bulk fluid temperature
T	period
t	time
TIM	thermal interface material
u	nominal velocity
$\vec{u}$	velocity field
$\bar{u}$	average velocity
V	voltage
v(t)	time dependent voltage
V_{an}	voltage between phase a and neutral
V_{ab}	voltage between phase a and phase b
V_{bn}	voltage between phase b and neutral
V_{dc}	DC bus voltage
WEG	water – ethylene glycol
X	sensitivity of pressure transducer
x	channel length
x_L	entry length
z	depth of circular duct

Units

°C	degree Celsius
cm	centimeter
GPM	gallons per minute
J	joule
K	Kelvin
kg	kilogram
kW	kilowatt
m	meter
mL	milliliter
mm	millimeter
Pa	Pascal
PPI	pores per inch
psi	pounds per square inch
psig	pounds per square inch - gage
s	seconds
V	volts
W	watt

Greek

α	dimensioned length
Δ	change
δ	substrate construction offset
ε	porosity
ζ	nondimensional length = $(x/D)/Re_D$
κ	permeability
μ	dynamic viscosity
ρ	density
ω	uncertainty

Chapter 1 - Introduction

Motivation

Cooling of electronic devices is crucial to their performance and reliability. Historically, the heat removal for power electronics has been provided through passive finned heat sinks, which reject the heat to air. Advances in semiconductor technology have led to increases in heat flux, which many existing heat sinks are not designed to meet. Proposed solutions for managing the increased heat flux typically move away from air cooling and include heat pipes, cold plates, spray cooling, refrigeration, enhanced surfaces, and direct pool boiling. In many cases, these technologies are developed as add-on solutions. The electronics are developed with the application in mind, and the thermal management is designed based on the package geometry and available ambient conditions.

Less often the two technologies, power electronic and heat management, are developed in parallel to optimize the thermal and electrical performance for the given application. Even though parallel development can produce optimal products, the process may by too costly for all applications. Yet when ultimate consumer cost and reliable performance is most critical, the process of designing the two technologies in parallel is warranted. More importantly some heat removal designs may improve upon typical packages by reducing their size and weight.

One such application that calls for this type of synergistic design is the inverter typical in hybrid electric vehicles (HEV) and plug-in hybrid electric vehicles (PHEV). The complexity of designing a power electronic system in a vehicle requires a large breadth of knowledge, including under-the-hood layout, package construction, power electronic device operation and physics, thermal management, and more [1, 2]. By designing the thermal control system in tandem with the electrical operation, the best use of resources and space can be achieved.

HEV manufacturers traditionally use two cooling loops under the hood to provide thermal control to the internal combustion engine (ICE) and the electric traction drive system. The two loops operate at two different nominal temperatures. The ICE loop provides 105°C coolant, and the traction drive radiator provides 70°C coolant. The cost benefit that can be realized from combining the loops into one is $150-200 per vehicle [1]. As automotive manufacturers desire to move away from two separate cooling loops, many design parameters for cooling the inverter and electric motor become more restricted. The major change is in the coolant temperature available to the inverter, which is now 35°C higher (i.e. 105°C). This increase in coolant temperature requires that the inverter operate at a higher temperature, which implies that special care must be taken to make sure that the power electronics can operate reliably.

Objective

This work seeks a new inverter package that is capable of operating with 105°C coolant. The focus of this research details the packaging design and thermal analysis of a direct cooled ceramic substrate that manages the heat load imposed by the power electronics.

Background

Two important aspects of inverter design are necessary to understand before beginning a new design. First is the operation of a basic inverter. Knowledge of electrical architecture or topology that is required dictates how the devices are physically arranged. This arrangement will control certain geometric parameters of the inverter and heat removal system. Knowledge of inverter operation is also crucial to understanding the heat source and the parameters that control the heat production.

The second aspect of designing a new inverter is to understand what is currently done on a device packaging level. Without understanding the basic package, attempts to improve the heat transfer may be unproductive. For example, the conduction resistance of the basic package is about the same as the convective resistance (0.1-0.5°C-cm^2/W) of advanced heat sinks [3]. Improving the heat sink performance may produce less benefit as compared to reducing the thermal resistance of the basic power electronic package.

Inverter Operation

An inverter is a specific example of a more general class of electric circuits classified as converters. The inverter converts a DC voltage source to AC current source [4]. In an HEV, the inverter typically takes DC battery voltage and changes it to an AC waveform for use in a 3-phase permanent magnet motor. A bi-directional converter can also take an AC generator signal and change it to a DC signal to recharge the battery. One of the most common architectures is a full bridge voltage source inverter as shown in Figure 1 [4].

DC current enters from the left and passes through a series of switches and diodes. The switches are controlled by an external signal, which typically uses a pulsed width modulation (PWM) control scheme to achieve the conversion to AC. The resulting AC signal is supplied to the load through phases *a*, *b*, and *c* on the right of the schematic. The capacitor on the left side filters any voltage ripple that may be present in the DC signal. Each electrical path that connects the positive DC bus to the negative DC bus is referred to as a leg. This inverter architecture has three legs. The switch-diode combination above the phase connection is generally called the upper leg, and the switch diode combination below the phase connection is called the lower leg.

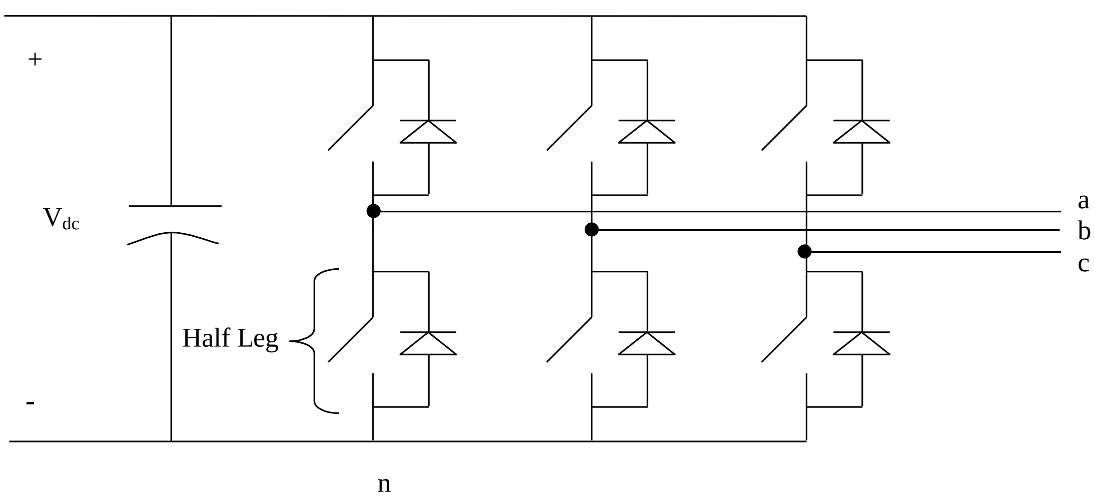

Figure 1. Electrical schematic of voltage source inverter

PWM is a control scheme that compares a reference waveform and a carrier waveform to determine when switches should be turned on and turned off. For an inverter, the carrier waveform is a triangle wave and the reference waveforms are sine waves. Each phase has its own reference waveform; the reference waveforms are 120° out of phase. Figure 2 shows a normalized example of these reference waveforms.

When the reference waveform is greater than the carrier wave, the switch on the upper leg for the respective phase is closed, and the switch on the lower leg is open. The resulting voltage from phase to DC negative (i.e. $V_{an,}$ $V_{bn,}$ or V_{cn}) is V_{dc}. When the reference waveform is less than the carrier wave, the lower switch is closed, and the upper switch is open. The resulting voltage from phase to DC negative is zero. Figure 3 shows the resulting waveforms for V_{an} and V_{bn}. To obtain the line-to-line output, V_{ab}, V_{bn} is subtracted from V_{an}, which is also shown in Figure 3.

The final line-to-line voltage alternates between positive DC and negative DC producing an AC signal. Depending on the motor or end of use application, the signal can be used directly. For applications that require a cleaner sine wave output, the output of the inverter is passed through a low pass filter so that the fundamental sine wave can be extracted.

It is during the switching process that the power electronic switches produce waste heat. In an ideal switching cycle shown in Figure 4, the switch would block all current when it is off. It would instantaneously switch from off to on. It would provide no resistance to current when it is on, and it would switch instantaneously back from on to off. This ideal switching process would result in no power loss where the average power loss is the product of the current, *i(t)*, and voltage, *v(t)*, integrated over the electrical period, *T*.

$$P = \frac{1}{T}\int_{t=0}^{T} i(t)v(t)dt \tag{1}$$

In a real switch, the switch cannot turn on and off instantaneously. Also during electrical conduction, the switch provides some finite resistance that results in a small on-state voltage. Real switches typically do a good job of blocking current. At voltage near

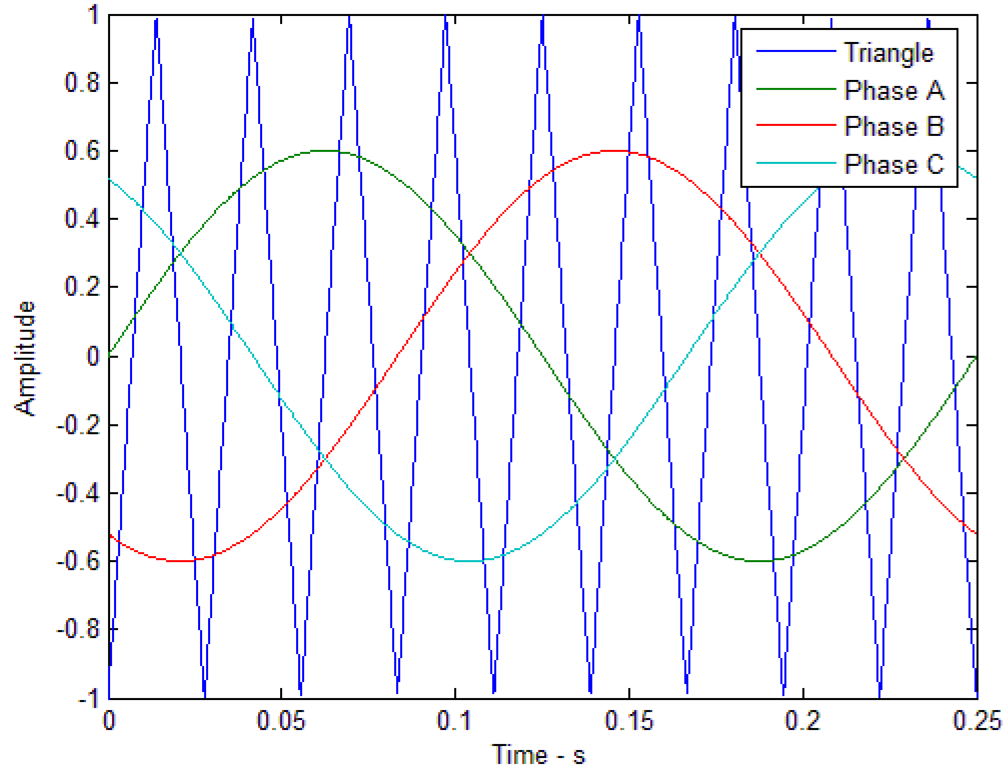

Figure 2. Reference waveforms for PWM operation

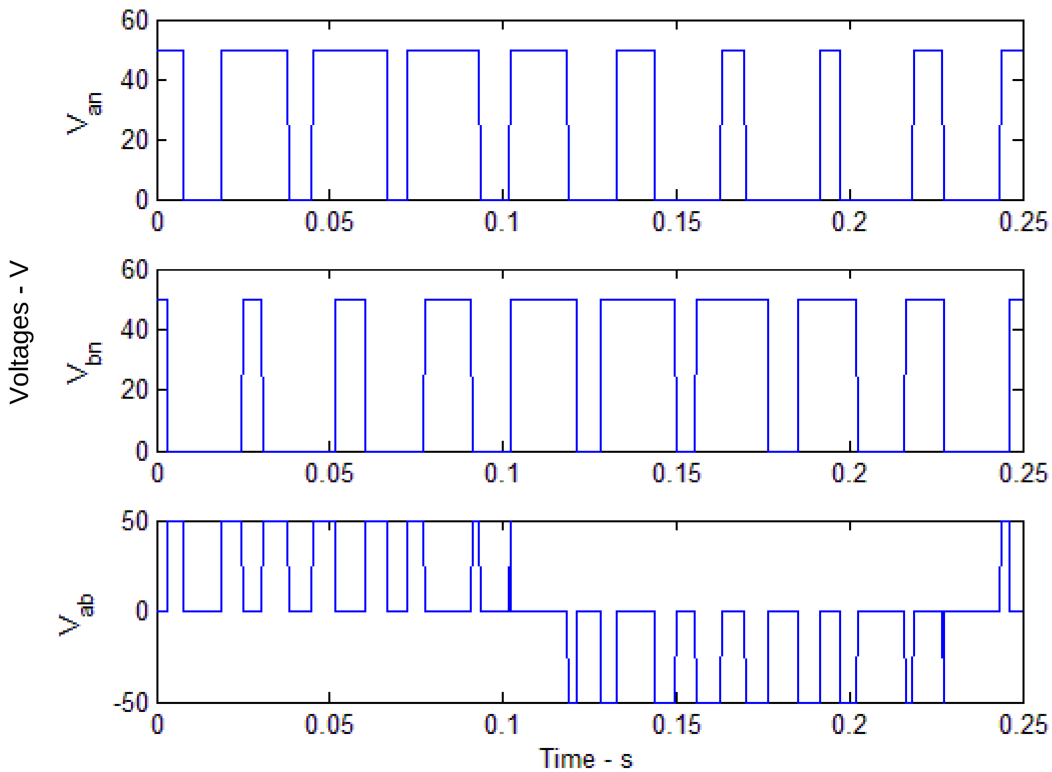

Figure 3. Resulting voltage waveforms for PWM operation for a DC link voltage of 50 V

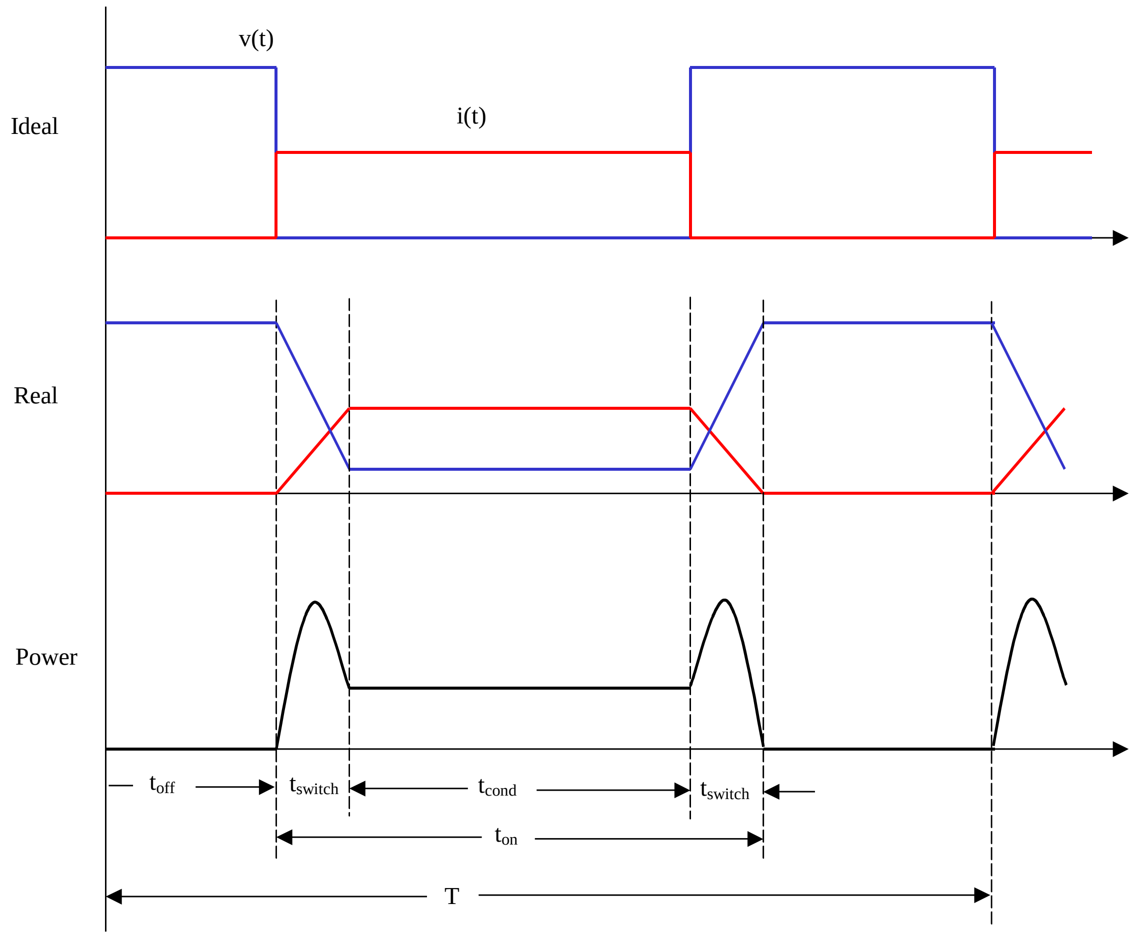

Figure 4. Ideal and real switching characteristics

the devices rated voltage, small leakage currents can occur. A combination of these effects produces a power loss that manifests itself as heat. Figure 4 also shows a simplified real switching cycle and the resulting power loss. In this figure, the leakage current is not shown.

It can be deduced that the heat load produced by an inverter is dependent on many variables: switch characteristics, diode characteristics, switching frequency, operating voltage, and operating current. It is hard to determine all of these parameters *a priori* a design. Analytically, the heat load can be estimated using device data sheets [1]. However, these estimates yield high efficiencies. More realistic numbers may come from previous literature and experimental testing results [5].

Inverter Packaging

In traditional packaging of power electronic devices, many layers exist to address the electrical requirements of the device. However, incorporating these packages into new applications can prove to be challenging, where the size and operation of the heat sink must be optimized. This task becomes even more important in applications where the ultimate coolant temperature is close to the temperature limit of the power electronic device.

Figure 5 is a schematic of a typical power electronic module attached to a generic heat sink. The power electronic module is outlined in the dotted line, which is attached to a heat sink. A thermal interface material (TIM) is placed between the power electronic module and heat sink to fill voids and promote better heat conduction to the heat sink. In this case, the heat sink could be a liquid flow channel, parallel fins with air cooling, or any other desired configuration.

In Figure 5, the power electronic chip is soldered to a direct bonded copper (DBC) substrate. This substrate provides electrical insulation from the rest of the package. It also provides a structure that reduces the coefficient of thermal expansion mismatch between copper and silicon devices. The DBC has three layers. The center is a thin layer of ceramic for electrical insulation. On either side of the ceramic, a layer of

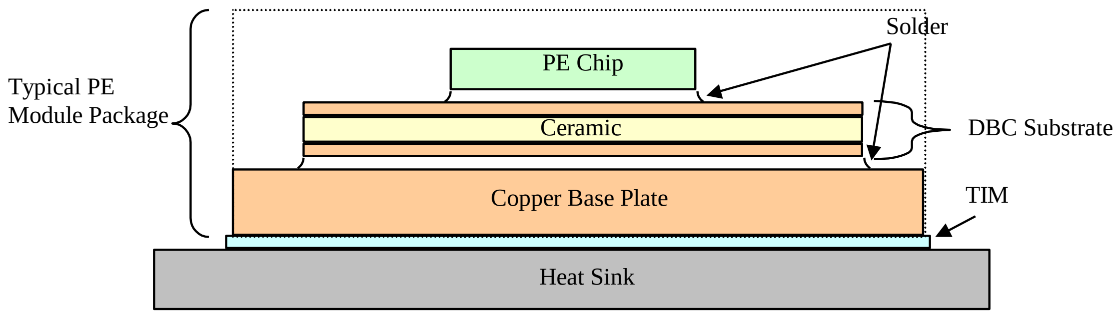

Figure 5. Schematic of power electronic package and heat sink (not to scale)

copper is molecularly bonded to the ceramic to provide solder surfaces for the chips and to connect the DBC to the package base. The DBC is soldered to a base plate to spread the heat out over a larger area and provide a more rigid structure to mechanically attach the module to traditional heat sinks.

The module is typically encapsulated in a plastic housing, and the chip is covered with a silicone gel to protect the wire bonds (not shown) from vibration and arcing. By eliminating some of these layers, particularly the TIM, heat transfer can be greatly increased by reducing the overall thermal resistance. Any improvement that will decrease the thermal resistance of the layers or eliminate them all together is an improvement that can decrease junction temperature, increase performance, and increase the overall chip reliability and lifetime.

Current Research

The purpose of this research is to design an inverter module for an HEV or PHEV that enables the use of 105°C 50/50 water-ethylene glycol (WEG) coolant. The module consists of an inverter half leg detailed in Figure 1. To enable the higher coolant temperature, the heat sink will be integrated into the ceramic structure as shown in Figure 6, which will eliminate the TIM and a solder layer which are traditionally found in power electronic packages [6].

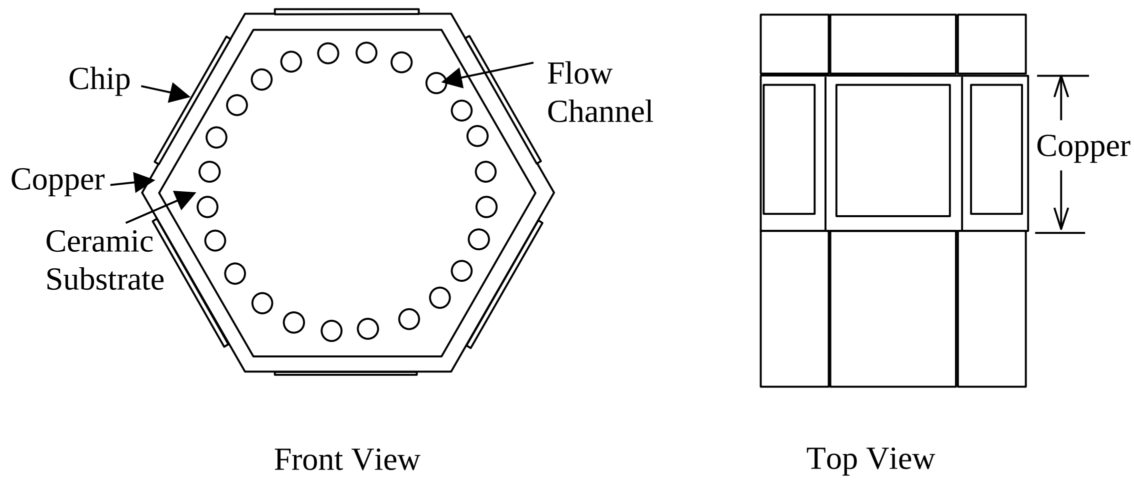

Figure 6. Schematic of proposed direct cooled substrate

The inner hexagon in the front view of Figure 6 is the ceramic substrate. A copper layer surrounds the substrate but does not cover the full length of the regular hexagon prism and is not symmetrically placed in the axial direction as shown in the top view. The chips are then attached onto the copper layer. Coolant would flow through the circular ducts that lie beneath the bonded copper surface. The hole pattern depicted is one of the several designs that are explored in this project. Here they are shown for demonstrating the overall concept and do not necessarily reflect any type of optimized coolant path. In other designs, a metal foam matrix was inserted into the duct(s) to increase the effective thermal conductivity of the WEG. These inserts were needed to achieve a balance between maximum device temperature, fluid temperature, heat load, and volume.

The hexagonal substrate shape was decided upon after several preliminary design iterations.   A general inverter package was first created to verify that this concept could result in a voltage source inverter topology that meets the necessary design targets. The proposed module would have cylindrical ends (not shown) that simplify the seals that keep the working fluid separate from the electronics. Furthermore, six faces provide enough space for the minimum amount of silicon required for a half leg of a three-phase DC to AC inverter. For a full bridge voltage source inverter, six of these substrates would have to be placed between inlet and outlet headers. The header package with six half-leg modules could be placed inside of a hollow cylindrical capacitor or along side a rectangular capacitor to complete the general inverter package. More discussion of the overall inverter package will be presented in this work. The primary focus of this work, however, is to design and analyze the ceramic substrate to manage the thermal load imposed by the power electronics.

Review of Related Work

Even thirty years ago when air cooling was meeting the demand of most electronics' heat dissipation, researchers realized the importance of new cooling strategies for the growing electronics market. Tuckerman and Pease developed the idea of incorporating microchannels into integrated circuit (IC) chips themselves [7]. Their approach eliminated all the extra conduction resistances from the junction to the ambient.

The heat exchanger, comprised of parallel microchannels, was etched in a typical silicon integrated circuit substrate. Thin film resistors were sputtered on the surface as an experimental heat source. The microchannels were sealed with a bonded plate, and deionized water was used as the cooling fluid. Deionized water is necessary to maintain electrical isolation between the cooling system and the potential device. The channels were supplied at an inlet manifold, which had also been etched into the silicon substrate. The theoretical power dissipation level was 1300 W/cm^2. Experimentally, the configuration was shown to dissipate 790 W/cm^2 with a junction to ambient thermal resistance of 0.09°C/W.

Other researchers have continued to develop the idea of on-chip cooling and tackle implementation problems like inlet and outlet seals and optimized flow channel geometries. Most commonly this method has been explored for printed circuit boards where isolating the electrical paths from the flow channel is more practical.

On chip cooling does not make sense for power electronic devices. Most devices have a vertical electrical structure, and electrical isolation would be completely dependent on the working fluid. Furthermore, silicon devices are fragile. High pressures typically needed for microchannel cooling would introduce new challenges to packaging the devices.

The next closest cooling option to the junction was to etch microchannels into a silicon substrate and directly attach the IC chip to it [8]. The chip served as the fluid seal. This unit was glued together and could be assembled prior to the circuit fabrication. The unit maintained the same footprint as IC chips of the day (~0.25”x 0.25”) and increased the total thickness from 0.008” to .040”. This strategy may work well for a single chip, but power devices are often paralleled to handle more current. Many devices would require manifolds to distribute the flow.

Instead of using the chip as a seal, Nayak et al. [9] explored the possibility of attaching a chip directly to a copper microchannel heat sink. Their motivation was to create a heat sink that had a lower pressure drop than the design of Tuckerman and Pease [7] that could be used for larger chipset footprints found in computers. They also wanted to be able to machine the heat sink rather than relying on silicon etching manufacturing methods. Additionally, they explored silicon as a microchannel heat sink material, but the design structurally failed from the required fluid pressure. With copper microchannels, they were able to remove 42 W/chip and maintain the junction temperature within 20°C of the fluid. Direct attach for power devices is often avoided because of the coefficient of thermal expansion mismatch between copper and silicon. At high temperatures, the mismatch can cause large residual stress that will compromise the structure of the die.

Up to this point, most efforts of cooling integration have involved lower powered IC level devices. Jankowski et al. [3, 10] detail the development of silicon and aluminum nitride (AlN) based microchannel heat sinks with direct die attach, i.e. no DBC. They used a power diode for the heat source. To alleviate pressure drop concerns typically experienced with microchannels, the design uses a manifold to deliver fluid perpendicular to the microchannels instead of parallel. While the material selection resolves the coefficient of thermal expansion mismatch, the silicon design presents concerns including isolation and the potential for voltage breakdown.

A second generation design uses AlN sputtered with a thin metallization layer to facilitate die attachment. In essence, the AlN design is most similar to the proposed work except that they use microchannels to achieve the enhanced heat transfer. More importantly the research explores the overall thermal resistance of placing the heat sink directly next to the chip. Thermal resistances of 0.1 to 0.175 K-cm^2/W are reported for the total thermal stack. This work demonstrates that by incorporating the heat sink closer to the die attach, that total thermal resistance can be almost halved from junction to ambient as compared to traditional packaging and cooling.

The next closest layer in a typical power electronic package to incorporate heat removal is on the other side of the DBC from the die attach. Exel and Schulz-Harder [11] have developed microchannel copper layers between two traditional DBC ceramic substrates. The power electronics are attached to the outer layers. The inner layer on the DBC is made up of bonded copper meshes to form the microchannels. The copper microchannels drastically reduce the thermal resistance of the cooling system by eliminating typical thermal greases, aluminum heat sinks, and solder layers. They also are able to apply chips to the top and bottom of the module to take advantage of the three-dimensional structure. The junction to ambient thermal resistances for this design range from 0.025-0.06°C/W depending on the mesh geometry and thickness. The authors acknowledge the future challenges of developing leak proof seals, copper compatibility with the working fluid, and copper compatibility with potential aluminum cooling system.

More recent designs start to transition to the use of base plates or head spreading plates attached to the DBC. In this design the base plate for an IGBT on a DBC is a copper microchannel heat sink [12]. To provide even more cooling, the wirebonds were replaced by solder bumps to turn the package into a flip chip package. This structure enabled a second DBC to be used on top of the chip and a second copper microchannel heat sink is used on the upper DBC as well. By providing double sided cooling, the waste heat dissipation increased by 76% as compared to the single sided microchannel.

While the use of microchannels is an effective means of enhancing heat transfer, they require a clean fluid. In the automotive environment, debris can enter the coolant over time. In the absence of a filter, which requires additional maintenance and larger pumps, the debris would clog these advanced cooling options.

A more suitable solution for automotive application is an actively cooled base plate. This is one of the more common proposals for reducing the overall resistance. The active base plate eliminates the TIM and combines the function of the heat spreading base plate and the heat sink. Research focused on this level of cooling is geared toward optimized heat sink design. Baumann et al. [13] propose substituting the solid base plate of a typical Insulated Gate Bipolar Transistor (IGBT) module with a plate that has a diamond shaped pinned fin arrangement. The integral pinned fin base would then be bolted to a liquid flow channel housing and sealed. They detail different pin shapes and patterns to achieve the best cooling performance.

Another variation of an active base plate includes a design that has flow channels stacked normal to the chip or die. This orientation promotes normal fluid flow toward the DBC as opposed to the traditional parallel channel flow in most common liquid cold plates [14, 15, 16]. In testing, the impinging flow design almost eliminates the temperature gradient across the base plate, which is typical of parallel flow over a heated plate. Another similar idea is discussed by Valenzuela [17].

These active base plates move further away from the device junction as compared to the microchannel research. The current research seeks a solution that is not affected by debris like the active base plate but is closer to the device junction like the microchannel solutions.

The National Renewable Energy Lab (NREL) conducted more general research to examine the basic heat transfer parameters required to achieve reasonable device operating temperature with the use of higher temperature coolants found in vehicles [18]. They compare a baseline package, like in Figure 5, to an integrated heat sink/base plate and a double-sided cooling design. With the maximum operating chip temperature at 125°C, cooling the heat load of 200 W/cm^2 was almost impossible for high temperature coolants. With a higher maximum allowable operating temp of 200°C, convection coefficients from 5,000 to 15,000 W/m^2/K were required to meet the heat flux goal.

NREL also explored air cooling [19]. The heat sink, though, must take on the form of microchannels to achieve the area/volume ratio required for automotive application. The air is taken at outside ambient condition of 30°C. No specific pressure drop is quoted but agreement is shown between their analytic model and CFD results. Their comparison between 30°C air cooling and 105°C liquid cooling shows that air requires 2.5 to 3 times more parasitic power and almost twice the physical volume. A liquid loop though is heavier and is more costly by 60%. NREL researchers advocate air especially for electronics with an allowable junction temperature higher than 125°C.

Air cooling may make more sense with wide band gap materials like silicon carbide or gallium nitride. These devices can operate at higher temperatures (>200°C) because of higher band gap energy of the material. These next generation devices are just starting to become viable for high power applications. Cheaper air cooled thermal management will most likely be the preference for them. However, to enable silicon devices to reach the limits of their operation and maintain reasonable volume sizes in automotive applications, liquid cooling is required.

Chapter 2 – Boundary Conditions and Design Parameters

Before constructing analytical and computation models, the boundary conditions and specific design parameters must be established. Models were used in this research to evaluate the thermal performance of the direct cooled substrate with respect to the operational limits. These parameters define a successful design but may also restrict design options.

Boundary Conditions

Thermal Load

In the past, two inverter ratings have typically been used in thermal models: 55 kW peak and 30 kW continuous. Previously constant efficiency in the inverter over the entire operational range of the inverter had been assumed [20, 21]. Thus, the thermal load for continuous and peak loading was determined from these parameters. However, this load derivation is not as valid as it first appears. The data from ORNL's SemiKron testing shown in Figure 7 indicates that waste heat magnitudes can approach maximum values while the output is below the peak power rating [5]. This is due to decreases in efficiencies based on operation frequency, modulation index, DC bus voltage, and other factors.

Using the maximum waste heat of 1746 W from Figure 7, an approximate waste heat distribution for power devices can be calculated. Assuming that the upper and lower leg of each phase will dissipate equal amounts of energy over an operational period, the heat loss per switch set is 291 W. Each switch set will have two diodes and three or four IGBTs. It is assumed that the diode losses are about a third of the switch losses. This approximation is based on an application note that SemiKron published for an inverter to control electric forklifts [22]. The power range was smaller than full-sized vehicles but the loss ratio is a good estimate of the loss distribution.

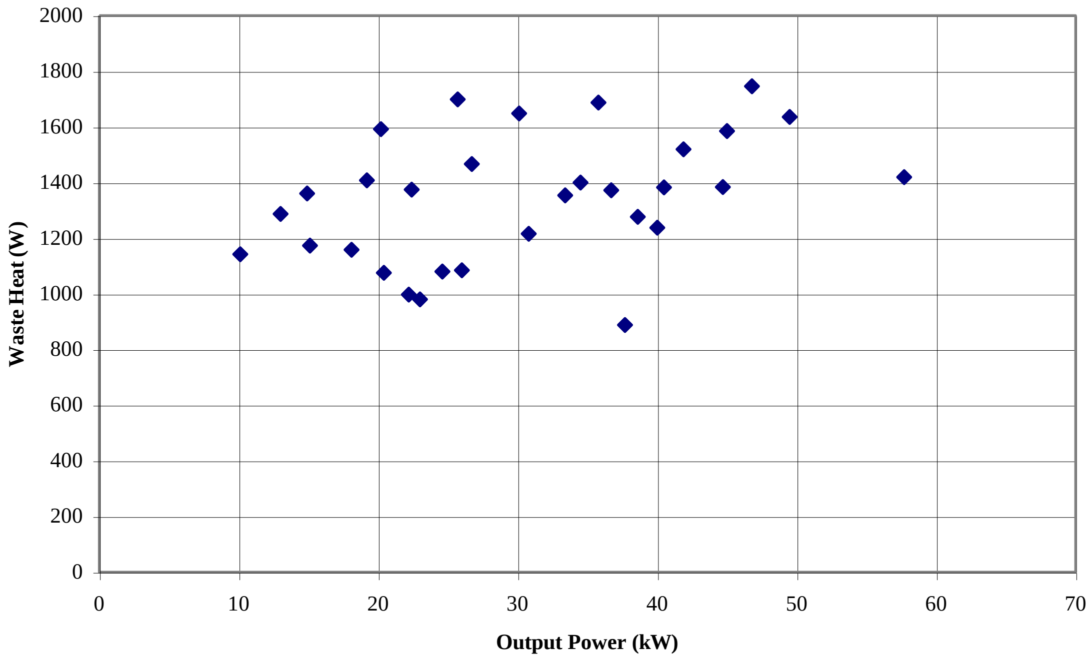

Figure 7. Waste heat produced by SemiKron inverter for different output powers [5]

A minimum of three switches is required to achieve the current rating for the inverter. If three switches were used, the losses would be 72.75 W per switch and 36.4 W per diode. Using four IGBTs per section implies 54.6 W loss per switch and 36.4 W loss per diode. Four switches would be helpful to spread the losses of the inverter out over a wider area and to provide additional margin of safety as the devices are being run on the upper end of their operational temperature range. The computer simulations will predict the maximum temperatures that will determine the appropriate chip set population.

A heat load for continuous power rating is not defined for this research. If designs are not thermally feasible at the steady state peak load, then a continuous load could be defined with a short transient peak. The transient modeling adds significant complexity to the computational models and is avoided if possible.

The thermal loads will be applied as an inward boundary flux to a silicon switch with a footprint of 10.23mm x 9.73mm [23]. In some models where the diode is modeled, the footprint is a 7.8 mm square. All other thermal boundaries are specified as thermally insulated. These insulated boundary conditions represent a conservative evaluation of thermal performance.

In reality, some heat will be removed from exposed surfaces by natural convection, radiation, impinging flow, and conduction to a manifold connection. If the predicted temperatures in the thermally insulated case meet the design specifications, then the actual performance should be better (i.e., lower chip and fluid temperatures).

Inlet Conditions

As alluded to earlier, the inlet temperature of the flow channels is specified as 105°C. This is the typical output temperature of an automotive ICE radiator. In general, the inlet flow was specified as a uniform velocity, which is derived from the maximum flow rate. Some models used slightly different conditions in the flow domain. These differences will be discussed in more detail as needed. The automotive manufacturers limit the maximum inverter flow rate to 2.5 GPM [24]. This boundary condition implies that the flow rate will have to be at a maximum in order to achieve the thermal performance indicated at a specified thermal load. Once preferred designs are chosen, some optimization in velocity/overall flow rate may be possible if more than sufficient cooling is present.

Design Parameters

Silicon Device Maximum Temperature

The maximum temperature rating of the newest silicon devices available on today's market is 175°C [23]. However, most device data sheets predict no power conduction at the maximum temperature. A silicon device's primary rating is its current (I) – voltage (V) characteristics which dictate how much current the device can conduct at the expense of a forward voltage drop. For IGBTs, theses curves depend on the applied gate voltage and junction temperature. For diodes, the I-V characteristic curves are temperature dependent. Moreover, both of these characteristic curves are based on the packaging that encapsulates the semiconductor, which limits the heat removal.

In this design concept, discrete semiconductors are being used, i.e. no prepackaged chips. Thus, a device can conduct rated current up to its maximum rated junction temperature as long as the waste heat being produced is removed. Even though devices are available whose maximum junction temperature is 175°C, the design parameter is limited to 150°C to increase the reliability of the inverter.

Most models do not explicitly model the semiconductor. The heat load is applied as a boundary condition. In this application, the solder layer is not represented either. The actual chip junction temperature would be slightly higher than what the models predict as the maximum temperature in the chip area.

Fluid Maximum Temperature

The fluid temperatures must be maintained below the boiling point of 50/50 WEG mixture so that automotive manufacturers do not have to alter radiator pressure ratings. Table 1 shows the boiling point for 50/50 mixes of WEG for various system pressures [25]. Typical automotive radiator caps are rated between 12 and 18 psig, but 15 to 16

Table 1. Boiling points for 50/50 mixture of water-ethylene glycol [25]

Pressure	Boiling Point
psig	*ºC*
0.0	107.1
12.0	125.4
13.0	126.6
14.7	128.6
16.0	130.0
20.0	134.1

psig is more common. Pressure ratings above 18 psig typically are indicative of high-performance parts.

The design limit is defined such that the fluid-wall interface must be maintained below 128°C. The boiling point of the working fluid at 16 psig is 130°C, but the fluid should remain in a saturated single-phase state. The computational simulation does not account for the latent heat transfer from liquid to vapor at the boiling point. Any simulation result that predicts temperatures above the design criteria would not be physically relevant.

Manufacturer Requirements

The automotive manufacturers also establish a maximum pressure drop of 13,800 Pa (2 psi) for the inverter cooling structure [24]. The original equipment manufacturers (OEM) also requires that the heat sink be able to pass a 1 mm particle. It is for this reason that many vehicle OEMs do not embrace microchannel technology that has been previously researched. Microchannels offer enhanced heat transfer but would easily clog with debris that is generated in the ICE coolant channels.

Material Properties

Several ceramic materials were explored for use in this inverter substrate. All of these materials are common to the ceramic insulator market. Table 2 shows the relevant thermo-physical properties of these materials. The properties were evaluated at 150°C to provide conservative estimates [26]. The silicon carbide ceramic is a sintered polycrystalline material that is different than the semiconductor material, which has a higher thermal conductivity than the material considered in this study [26]. In general, the thermal conductivity of all ceramics increases with decreasing temperature. In several designs, metal foams were incorporated to act as a thermal conductivity enhancer for the WEG.

Table 3 contains the bulk thermo-physical properties of the 50/50 WEG and WEG/metal foam composite. For the metal foams, the thermal conductivity is an effective thermal conductivity based on correlations by Calmidi and Mahajan [27]. The density and specific heat are that of the working fluid because the bulk of the heat energy is transferred to the fluid [28]. The properties of individual components were determined from WEG manufacturer's literature and base metal properties [25, 29]. The metal foams selected for examination were specified as 10 pores per inch (PPI). This open cell structure has holes large enough to meet the OEM particulate requirement without readily clogging.

Other material properties in the models included the thermo-physical properties of the copper, aluminum, and silicon, which are in Table 4 [29].

Table 2. Ceramic thermo-physical properties

Material		Thermal Conductivity *W/m-K*	Density kg/m^3	Specific Heat *J/kg-K*
Alumina	Al_2O_3	25	3700	800
Aluminum Nitride	AlN	160	3260	740
Beryllium Oxide	BeO	146	2850	1046
Silicon Carbide	SiC	130	3100	720

Table 3. Bulk thermo-physical properties of WEG/metal foam composite

	Thermal Conductivity *W/m-K*	Density kg/m^3	Specific Heat *J/kg-K*	Viscosity Pa-s
50/50 WEG	0.4	1006	3750	0.0006
50/50 mixture with copper foam	14	1006	3750	0.0006
50/50 mixture with aluminum foam	7.2	1006	3750	0.0006

Table 4. Thermo-physical properties of other DBC materials

Material	Thermal Conductivity *W/m-K*	Density kg/m^3	Specific Heat *J/kg-K*
Copper	400	8700	385
Aluminum	160	2700	900
Silicon	163	2330	703

Chapter 3 – Free Flow Duct Designs

The initial approach to cooling the power electronic devices on the hexagonal module was to develop simple flow channel geometries in the ceramic substrate. During this process, the regular hexagon dimensions, duct dimensions, and duct locations varied. Later on, porous metal foams were included in the ducts to promote more heat transfer. This chapter chronicles the evolution of the duct designs with “free flow”, which represents flow that is unrestricted by thermal enhancement material.

In a goal to make the overall module’s cross-sectional area as small as possible, the side of the outer hexagon was set to 12 mm. The side length was determined by the size of the power electronic chip, which was 10.23 mm wide. The length of the substrate was determined by the electrical layout and connections. Its total length is 30 mm.

Circular Duct

The first duct configuration was a series of cylindrical holes, which were equally spaced around the hexagonal prism. Several different duct sizes and spacings were considered. An example of this layout is in Figure 8 where 24 holes with a diameter of 1.27 mm are drilled through the ceramic subsection. They are equally spaced on a bolt circle that maintains a minimum ceramic wall thickness of 1.27 mm (0.050”). The minimum distance is maintained to provide structural integrity and is based on manufacturing limitations. The dark triangle is a thermally symmetric section, which represents the unit cell that is modeled later.

To fully understand the thermal behavior of this substrate full three-dimensional computer simulations will be required. Because of the time and resources required to carry out this modeling, it is desirable to focus the computer modeling on selected duct dimensions. Analytical estimations can be made to select a circular duct design that performs the best.

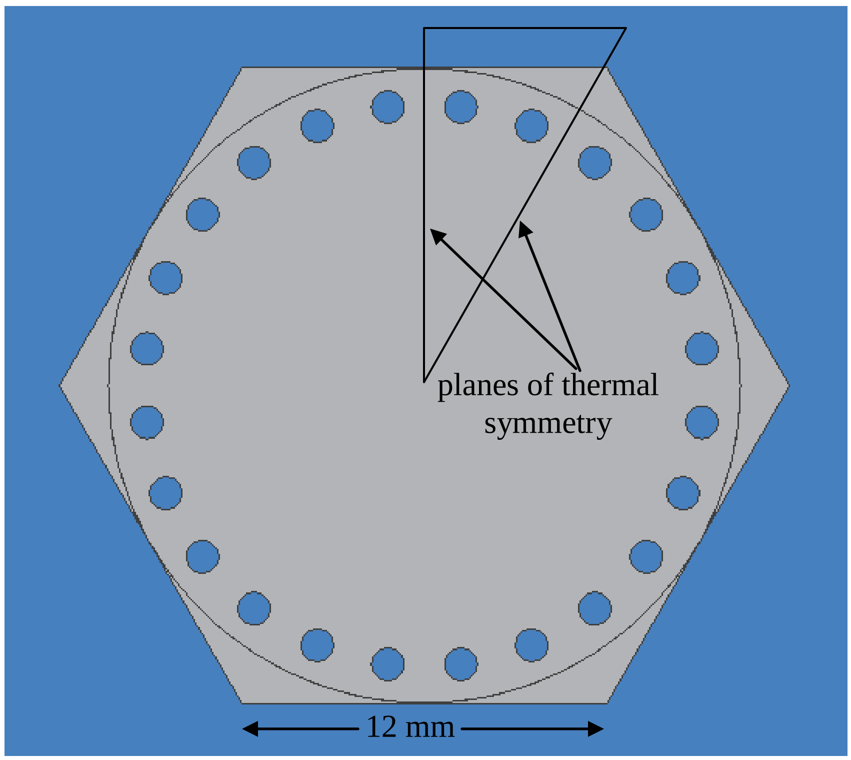

Figure 8. Sketch of hole geometry relative to hexagon substrate with symmetric geometry noted

Analytical Estimation of Duct Size and Number

In order to estimate the number and size of circular ducts to achieve the design criteria, an individual circular duct was analyzed with a constant heat flux wall. The heat load for the duct was determined by uniformly distributing 55 W/switch over one-sixth of the total number of ducts. The total number of ducts varied depending on diameter. Duct diameters of 1.27, 1.778, 2.54, and 3.175 mm were investigated. As the hole diameter increases, the total number of channels that can fit in the regular hexagonal prism with flats of 12 mm decreases. The number of ducts in the substrate for each diameter and the heat load for each case is listed in Table 5.

For the analytical estimation of thermal/fluid performance, correlations for the heat transfer were used. Because of the short duct length, developing flow correlations were used for pressure drop predictions and heat transfer [30, 31, 32, 33, 34]. To definitively show that the flow regime is developing, the criteria defined by Shah and London [35] is used. Eq. (2) shows this relation where the entry length, x_L, is dependent on channel diameter, D, and the Reynolds number, Re_D. Among all flow channel diameters, the minimum entry length for 2.5 GPM total flow rate is 131 mm, which is more than four times the length of the channel in consideration. The correlation in Eq. (2) differs from the typical definition of entrance length in Eq. (3) [31] because it does not allow the entrance length to go to zero as Re_D goes to zero. However for values of Re_D at 2.5 GPM total flow, the two methods only differ by 7% where Shah and London's correlation [35] results in shorter entry length predictions.

Table 5. Dimensional parameters for various circular ducts and associated heat load

	Hole Diameter (mm)			
	1.27	1.778	2.54	3.175
Number of ducts per Hexagon	24	18	12	12
Heat Load per Duct (W)	13.75	18.3	27.5	27.5

$$x_L \approx \left(\frac{0.6}{1+0.035\,\mathrm{Re}_D} + 0.056\,\mathrm{Re}_D \right) D \tag{2}$$

$$x_L \approx 0.06\,\mathrm{Re}_D\, D \tag{3}$$

The laminar pressure drop in the developing flow region is described by an apparent friction factor. Its relation to pressure drop is given in Eq. (4) where *p* is the pressure, $f_{F,app}$ is the apparent friction factor, *x* is the length of the channel, D is the duct diameter, ρ is the fluid density, and $\bar{u}$ is the mean velocity [30]

$$p_0 - p_x = f_{F,app} \frac{4x}{D} \left(\frac{1}{2} \rho \bar{u}^2 \right). \tag{4}$$

The apparent friction factor takes into account the added shear stresses associated with fluid core acceleration in the developing region. It is predicted by another correlation Shah and London [35] shown in Eq. (5). This correlation is valid for developing flow in circular, annular, and rectangular ducts. In this case, the empirical constants are only presented for the circular ducts: $f_{FP}\,\mathrm{Re} = 16$, $K_\infty = 1.25$, $c_1 = 0.000212$

$$f_{F,app}\,\mathrm{Re}_D \approx \frac{3.44}{\sqrt{\zeta}} + \frac{f_{FP}\,\mathrm{Re}_D + K_\infty / 4\zeta - 3.44/\sqrt{\zeta}}{1 + c_1/\zeta^2},\; \zeta = \frac{x/D}{\mathrm{Re}_D}. \tag{5}$$

At the maximum flow rate for the inverter, the flow for all hole diameters is laminar, i.e. $Re_D < 2300$. The pressure drop results at this condition are in Figure 9. The maximum pressure drop is 666 Pa (0.1 psi), which is well within the parameters of the design.

For later investigation, the total inverter flow rate is increased to the turbulent regime. For the turbulent pressure drop across the channel, Phillips [36] notes that the friction factor for fully developed turbulent flow is not valid until x/D~100 even though fully developed turbulent flow is usually reached by x/D~10. For circular and rectangular ducts, Phillips suggests Eqs. (6a-c), where $D_e = D_h$ for circular ducts

$$f_{F,app} = A\,\mathrm{Re}_{De}^{B}, \tag{6a}$$

$$A = 0.0929 + \frac{1.0161}{x/D_h}, \tag{6b}$$

$$B = -0.02680 - \frac{0.3193}{x/D_h}. \tag{6c}$$

To calculate heat transfer to the fluid and estimate the channel wall temperature in the laminar cases, Newton's law of cooling is used as shown in Eq. (7) [33]

$$q'' = h_x(T_s(x) - T_\infty). \tag{7}$$

In Eq. (7), q'' is the applied heat flux, h_x is the local heat transfer coefficient, $T_s(x)$ is the surface temperature at axial length x, and T_∞ is the bulk fluid temperature. The heat load is prescribed by dividing the total load in Table 5 by the surface area of the duct. The heat transfer coefficient is determined by flow parameters and is related by a nondimensional quantity, the Nusselt number where $Nu_x = {h_x D}/{k}$ [33]. In this expression, k is the thermal conductivity of the fluid, which is 0.4 W/m·K, D is the diameter of the duct, and h_x is the local heat transfer coefficient.

In a circular duct with constant heat flux, the correlation in Eq. (8) by Churchill and Ozoe [32] is used for Nusselt number. This correlation is valid for entrance and fully developed regions and was shown to agree within 5% of numerical data for Pr = 0.7 and Pr = 10.

$$\frac{Nu_x}{4.364\left[1+(\beta/29.6)^2\right]^{1/6}} = \left[1+\left(\frac{\beta/19.04}{\left[1+(\mathrm{Pr}/0.0207)^{2/3}\right]^{1/2}\left[1+(\beta/29.6)^2\right]^{1/3}}\right)^{3/2}\right]^{1/3},$$

$$\beta = \frac{\pi}{4}Gz\,,\ Gz = \frac{\mathrm{Re}_D\,\mathrm{Pr}}{x/D}. \tag{8}$$

Because the maximum wall or surface temperature of the channel occurs at the exit of the duct, the heat transfer coefficient and bulk fluid temperature in Eq. (7) should be evaluated at the exit. The bulk fluid temperature at the exit is found from Eq. (9) with an energy balance on the fluid where $T_{\infty,i}$, is the bulk fluid temperature at the inlet

$$T_{\infty,e} = T_{\infty,i} + \frac{q}{\dot{m}c_p}. \tag{9}$$

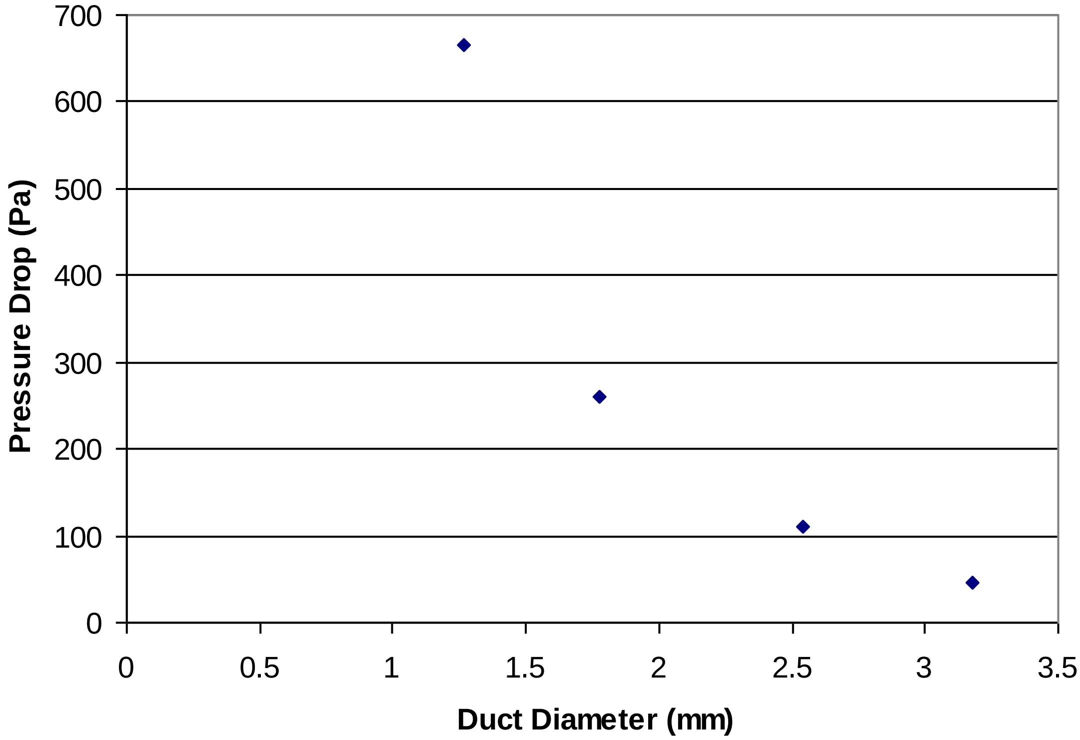

Figure 9. Calculated pressure drop for laminar flow across 30 mm long circular channels at 2.5 GPM

In most cases beyond the maximum inverter flow rate of 2.5 GPM, the flow transitions into the turbulent regime. The Nusselt number correlation in Eq. (10) is used to develop the heat transfer coefficient for turbulent flow in a circular duct [32]

$$Nu_D = 0.023\,\mathrm{Re}_D^{4/5}\,\mathrm{Pr}^{0.4}. \tag{10}$$

The four channels sizes were examined for inlet velocities from 0.05 m/s to 1 m/s. The results for the maximum channel surface temperature are in Figure 10. These results include both laminar and turbulent flow conditions as appropriate for each duct diameter and flow rate. At the maximum inverter flow rate of 2.5 GPM, the 1.27 mm diameter duct produced the lowest temperature at 132.4°C, which is above the boiling point of 50/50 WEG. The flow is laminar for all hole diameters at this flow rate limit. To achieve a fluid temperature at the wall of 130°C, the inverter flow rate must be increased to at least 2.9 GPM, which is still in the laminar flow regime.

Thermal performance of constant flux wall circular ducts was analyzed to focus the required computer simulation efforts on selected duct design. From the analytical estimation, the 1.27 mm diameter duct performs the best at the maximum inverter flow rate. In the hexagonal substrate, material properties, duct location, and heat source location will affect the fluid temperature results. To get a better idea of the impact of these factors on thermal performance, three-dimensional models must be generated.

Finite Element Analysis of 3D Unit Cell

The commercial finite element code, COMSOL, was used extensively in this research. This software package is a general partial differential equation solver that has specific modules built around general physics like heat transfer, structural mechanics, fluid flow, and more. It has the capability of modeling one, two, and three-dimensional geometries. Also included in this package are CAD tools and mesh generators. In addition to the graphical user interface, the models can be exported as MATLAB files to customize the geometries, boundary conditions, and solver parameters. This feature is particularly useful in running large batch problems where only one or two parameters are varied over wide ranges.

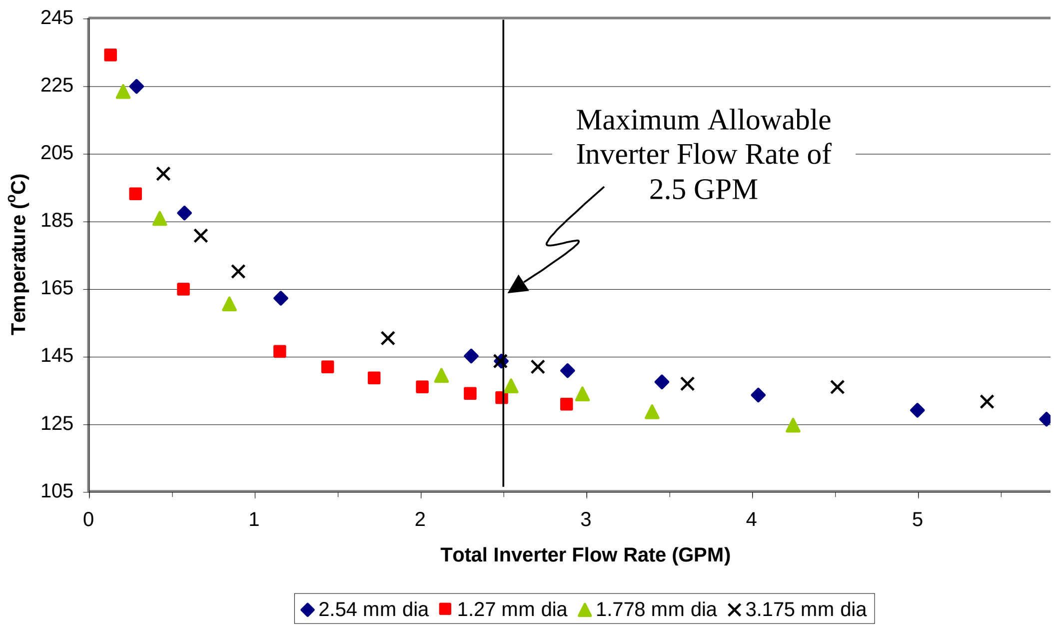

Figure 10. Maximum fluid temperature at the duct wall for 30 mm long channel

From the analytical analysis of the constant heat flux circular duct, the 1.27 mm diameter duct produced the lowest fluid wall temperatures for a fixed inverter flow rate of 2.5 GPM. The performance of this selected design will change based on the three-dimensional effects of conduction. Furthermore, no information is gleaned from the performance estimation on device temperature. For this reason, simulations are necessary to better understand the limits of the free flow duct design.

Model Setup

To model the geometry depicted in Figure 8, a one-twelfth symmetrical section was built. This section consists of two identical flow channels that are bounded by insulated walls. On top of the ceramic is a copper layer that is topped with a device footprint. Figure 11 shows this geometry. Certain physical details of the actual piece are omitted for simplicity. These details include rounded ends where the module would connect to a flow header, wirebonds, and solder layers.

Using a thermally symmetric unit cell aides in the accuracy of the model. The accuracy of the computed energy transfer is related to the mesh density. The mesh can be considered sufficient when increasing the mesh no longer produces significant change in the model output. Typically in three-dimensional models, a mesh independent solution can require 100,000 to 1,000,000 elements or more. The cost for increased mesh density is computer resources. For limited computer resources, cuts in the geometry domain can be made along symmetry planes without affecting the physics of interest. The smaller symmetric sections allow for increases in mesh density and thus accuracy while remaining in the operational limits of the computation resources available.

The modeling for this problem consists of a coupling of 3-D Incompressible Navier-Stokes and 3-D General Heat Transfer modules. It is possible to fully couple these models in COMSOL with temperature dependent physical properties and a buoyancy source term. In this case, the flow is forced convection so the buoyancy source can be neglected, and the physical properties are chosen to be constant. Therefore, full coupling of the flow and thermal models is not required. Instead, the velocity field was solved first, and the resulting solution was used to solve the steady state temperature

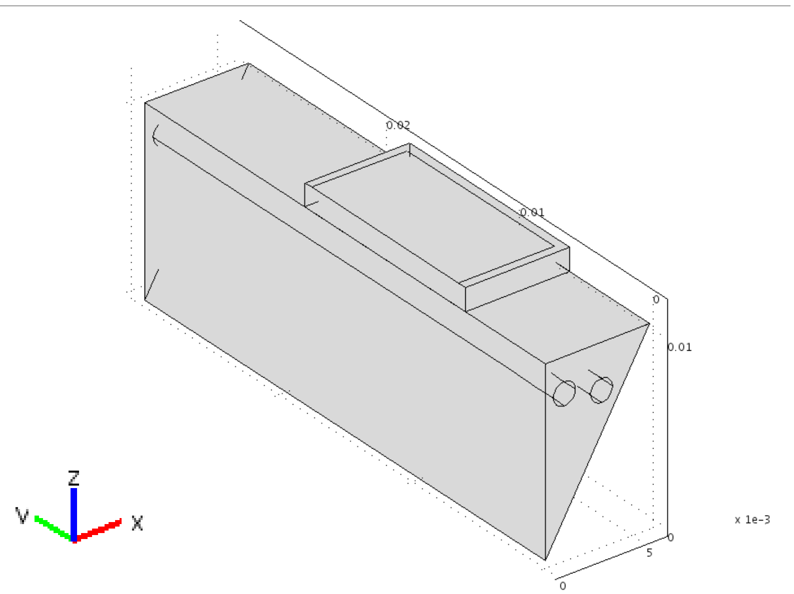

Figure 11. Drawing of a unit cell symmetric subsection of geometry shown in Figure 8

distribution. Even with this approach, the three-dimensional nature of the design requires either a large multiprocessor machine, long iterative solution schemes, or a novel alternative to solve for the velocity and temperature fields.

The velocity field in each flow channel of the design should be identical given a uniform pressure at the inlet and outlet. Furthermore, the flow field in the channel ought to be axisymmetric. Thus, a novel solution scheme is used to map a 2-D axisymmetric flow field solution onto the 3-D unit cell. The mapped flow field solution is used to solve the temperature distribution. This method reduced computational time significantly.

Several ceramic candidate materials are explored for the substrate. Thermal performance will not be the only variable to consider in the final design decision. Material availability, manufacturability, compatibility, and cost will also be important. The ceramic material properties were detailed in Chapter 2.

Governing Equations

For the 2-D axisymmetric flow field, the governing equations are the incompressible Navier-Stokes and the continuity equations in Eq. (11) and (12)

$$\rho\vec{u}\cdot\nabla\vec{u} = \nabla\cdot\left[-p\mathrm{I} + \mu\left(\nabla\vec{u} + (\nabla\vec{u})^{T}\right)\right], \tag{11}$$

$$\nabla\cdot\vec{u} = 0, \tag{12}$$

where ρ is the density, $\vec{u}$ is the velocity field, p is the pressure distribution, μ is the viscosity, and **I** is the identity matrix. The fluid properties are chosen as constant, which are specified at the mean temperature of the inlet and outlet bulk fluid temperatures. The outlet bulk fluid temperature is found from an energy balance on the flow channel. These properties were considered sufficient because the thermal properties of the working fluid vary less than two percent over the maximum operating temperature range.

After the velocity field is solved, it is mapped to a 3-D cylinder, and the temperature distribution can be found. The steady state temperature distribution in the solid domain of the ceramic and copper is given by the heat equation with constant properties in Eq. (13)

$$k\nabla^{2}T + Q''' = 0, \tag{13}$$

where k is the thermal conductivity, T is the temperature, and Q''' is volumetric heat generation. In this case, the heat load is applied as a boundary condition on the surface area that is the chip footprint, and Q''' = 0.

In the General Heat Transfer module, the coupling of the flow field and the temperature distribution is done through enabling convective heat transfer. The fluid in the duct experiences convection, which is governed by the energy equation:

$$\rho c_{p}\vec{u}\cdot\bar{\nabla}T = Q''' + k\nabla^{2}T, \tag{14}$$

where c_p is the specific heat of the working fluid and the velocity field, $\vec{u}$, is from the mapped flow field solution.

Extrusion Coupling/Solution Mapping

As alluded to earlier, the model requires the 3-D flow field to be resolved before solving the temperature distribution. Early models using iterative methods proved to be extremely time consuming and resource intensive. Models for the 3-D flow field alone required fine mesh refinement for adequate solution convergence. For just one of the flow channels, the model created near one million degrees of freedom, which was the upper limit of the computing resources available.

To speed up and in some cases enable, the flow field solution process, Extrusion Coupling Variables, a feature available in COMSOL, were used. A two-dimensional axisymmetric solution of the flow field was mapped onto three-dimensional circular ducts, which are a part of the unit cell model as shown in the triangle in Figure 8. The flow field in the duct was then resolved into Cartesian components and used in the General Heat Transfer convection model. This process allows for a coarser mesh to be used to find the temperature distribution in the solid region. The reduced number of degrees of freedom allows for more solver options, including direct solvers, to be used to find the temperature distribution. With the computing resources available, the above procedure reduced the entire computational time by more than two orders of magnitude as compared to just solving the entire 3-D velocity field. Detailed instructions for the mapping procedure are included in COMSOL - Help [37].

Boundary and Mesh Parameters

The boundary conditions for the 2-D axisymmetric flow at the inlet has a specified dimensionless velocity, Re_D, that was parametrically increased up to a nominal Reynolds number,

$$\mathrm{Re}_{D,in} = \frac{\rho v_{in} D}{\mu} = 1841, \tag{15}$$

where v_{in} is the nominal inlet velocity at 2.5 GPM. The outlet was set to “Outlet, Pressure, no viscous stress, $p_0 = 0$”. The wall was set to no slip and the centerline to axisymmetric. The mesh for the 2-D axisymmetric solution can be as fine as needed for an accurate solution because the mapped solution will only be as good as the initial solution that it is given as a source.

For the full 3-D model of the unit cell, the inlet temperature is specified at 105°C. The outlet of the flow channel is given a convective flux condition. The velocity field is specified as it relates to the extruded coupled variables as previously described. The chip footprint is given an input flux of 454,545 W/m^2. All other boundaries were left as thermally insulated, which is COMSOL’s default condition. These boundary conditions represent a conservative evaluation of thermal performance.

In reality, some heat will be removed from these adiabatic surfaces by natural convection, impinging flow, and conduction to a manifold connection. If the predicted temperatures in the thermally insulated case meet the design specifications, then the actual performance can be expected to improve with lower chip and fluid temperatures.

FEA Results for Circular Duct

For $Re_{D,in}$, the maximum chip interface and fluid temperatures are shown in Figure 12. The chip interface temperature is found on the footprint of the chip. The maximum fluid temperature is found on the channel wall closest to the heat source.

In Figure 12 the three ceramics with higher thermal conductivity, aluminum nitride (AlN), beryllium oxide (BeO), and silicon carbide (SiC), have interface temperatures that are below the operation limit of 150°C, but the fluid wall temperatures are above the boiling point of the working fluid, which is 130°C. The lower thermal conductivity ceramic, Alumina, drastically exceeds both design limits. Boiling is not desirable because it could eventually lead to localized hot spots that could damage the electronic component. Furthermore, the model was not created to simulate the phase transition at boiling, thus the temperature results are not accurate when the boiling point is exceeded. An increase in the flow rate and thus Reynolds number will eventually bring the fluid temperature below the boiling point where modeling results can be more reliable; however, the flow rate is already at its specified maximum.

Examining the temperature distribution at the outlet of the circular duct in Figure 13 shows that the thermal boundary layer thickness is small. Ideally less fluid would remain at the inlet temperature to better utilize the heat capacity of the working fluid. In this case, manufacturing and cost limitations prevent interior grooves or fins from being integrated into the ceramic core. The simplest change would be to examine other duct shapes that might spread the heat more uniformly.

During this research phase, a cost study was also completed on the different candidate materials [38]. It was found the alumina was the cheapest material. The other

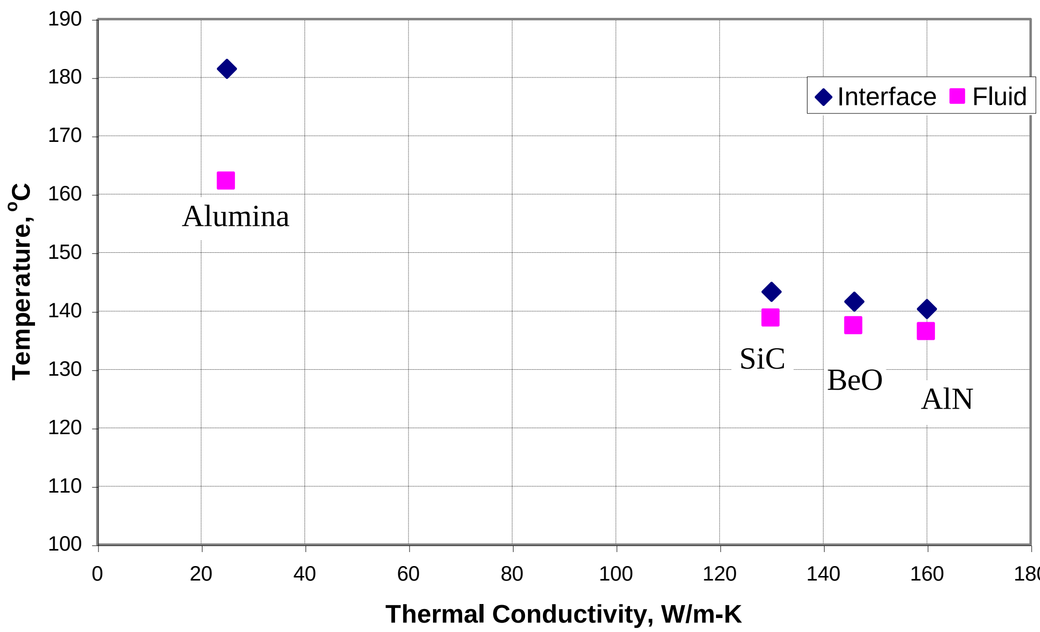

Figure 12. Maximum interface and fluid temperatures of 1.27 mm diameter duct for the four ceramic materials at $Re_D = 1841$

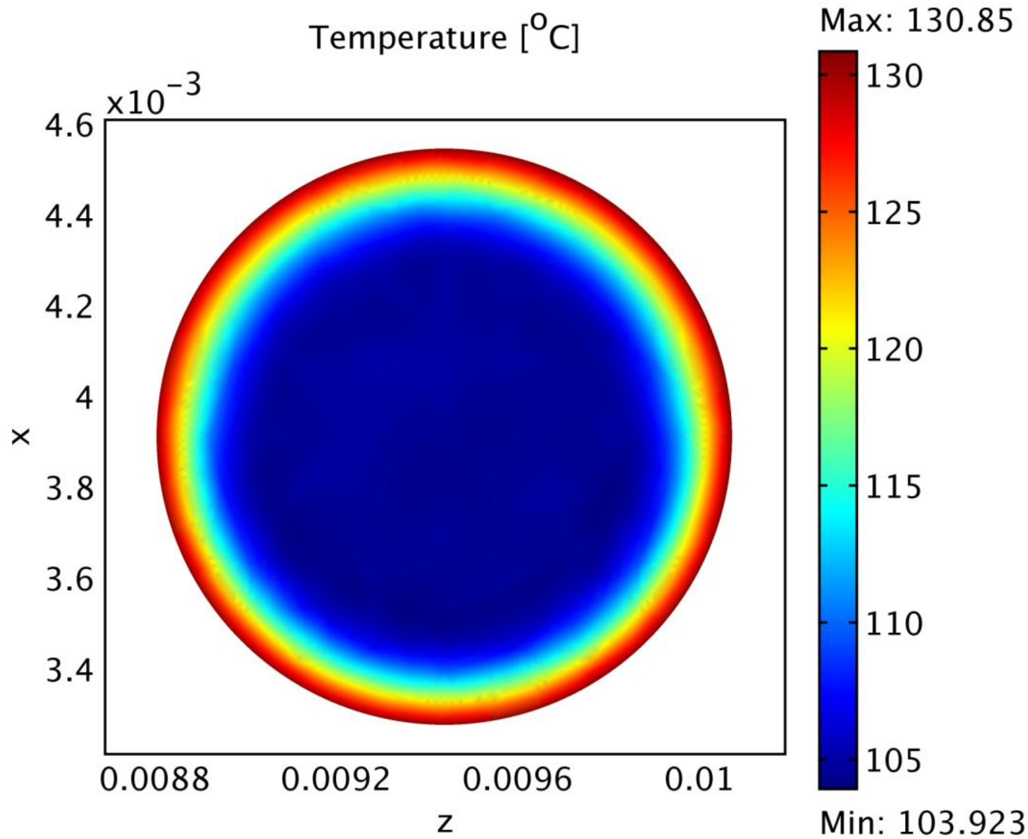

Figure 13. Temperature distribution for end of circular channel

materials ranged from 5 to 10 times more expensive. Because of the dramatic increase in cost, the research focus was directed to making an alumina substrate perform within the design criteria. Unfortunately, this ceramic material possesses the lowest thermal conductivity among the material candidates, which requires that the overall cross-sectional area of the hexagonal substrate be increased to aid heat spreading. Justification for the exact size increase will be explained in Chapter 4. For subsequent studies in this section, the hexagonal substrate has a flat dimension of 24 mm.

Rectangular Duct

The first analysis of possible flow channel configurations just looked at small through holes of a circular shape as shown in Figure 14. The analytical approximation focused the research effort on a selected duct diameter and population, but the COMSOL results indicated that the internal wall temperature exceeded the boiling point of the fluid. A change to the flow channel geometry is needed to produce a lower fluid wall temperature.

One systematic way to study flow channel shape is to look at conduction shape factors. The shape factors provide a scale of heat transfer. Shape factors exist for a long circular duct embedded in semi-infinite media [33]. They also exist for rectangular ducts embedded in semi-infinite media [39]. A rectangular duct would appear to provide some advantage for heat transfer because a rectangle would have less cross-sectional area for the same surface area or perimeter when compared to a single circular channel. The smaller area would allow for a higher average inlet velocity as compared to the circular channel given a constant volumetric flow rate. Also, the thickness or height of the duct could be designed to provide better heat spreading to the fluid that would result in a smaller outlet fluid core at the initial fluid temperature as compared to Figure 13.

Analytical Evaluation

The shape factor expression takes into account the distance from the outer surface to the surface of the embedded object. The theoretical shape factors for a cylinder and

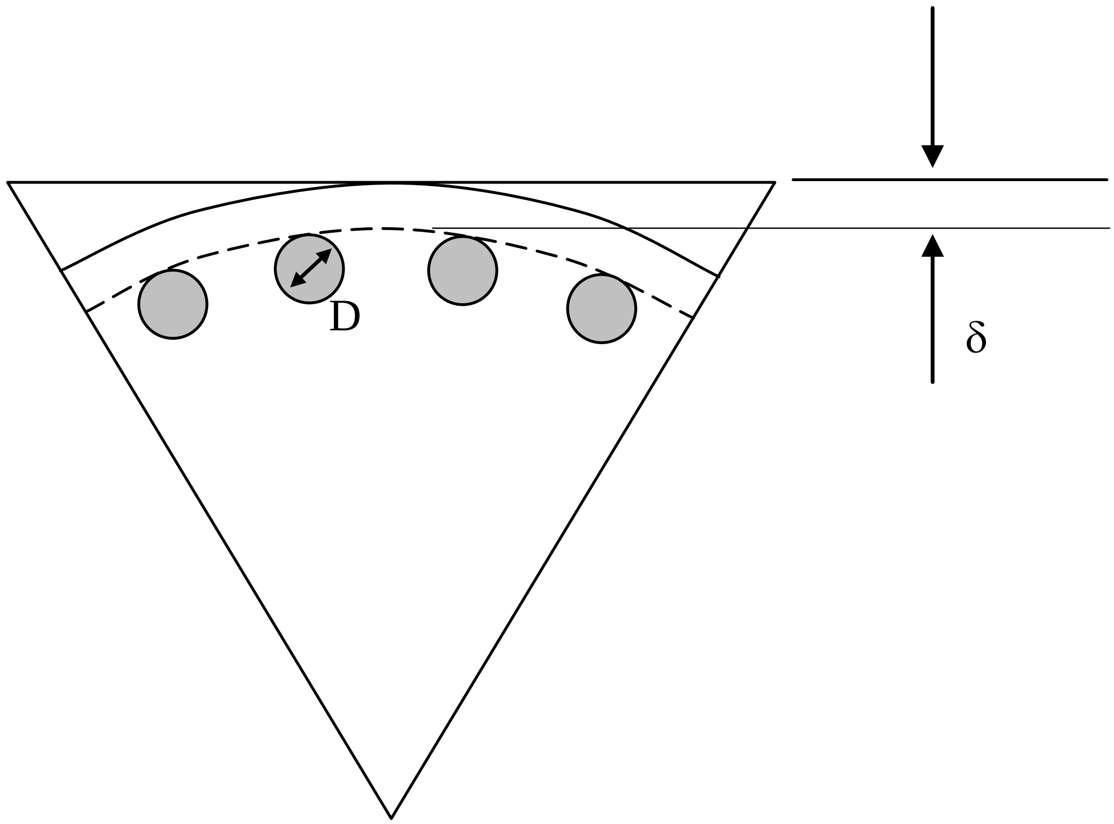

Figure 14. Schematic of duct configuration in ceramic substrate

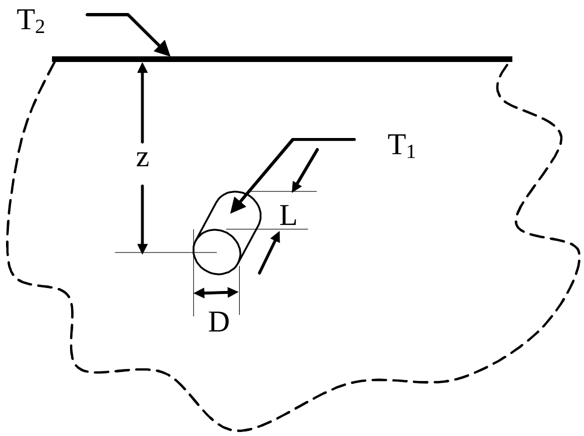

$$\frac{2\pi L}{\cosh^{-1}(2z/D)}, \quad L >> D$$

$$\frac{2\pi L}{\ln(4z/D)}, \quad L >> D \;\&\; z > 3D/2$$

Figure 15. Shape factor for embedded cylinder [33]

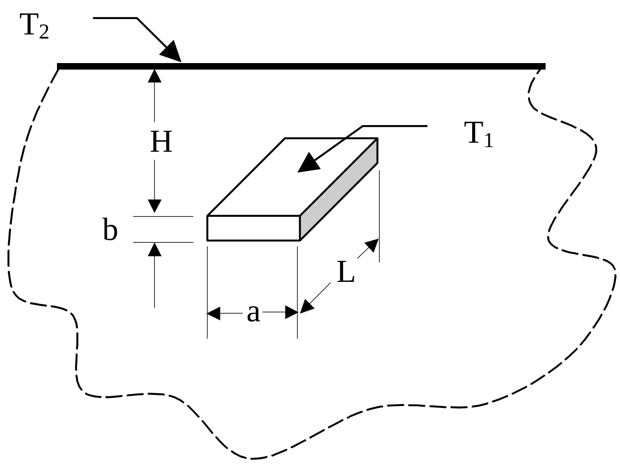

$$2.756L\left[\ln\left(1+\frac{H}{a}\right)\right]^{-0.59}\left(\frac{H}{b}\right)^{-0.078},$$

$$L >> H, a, b$$

Figure 16. Shape factor for embedded rectangular duct [39]

rectangular duct are in Figure 15 and Figure 16. Heat transfer using shape factors is defined by:

$$q = Sk(T_2 - T_1), \tag{16}$$

where S is the shape factor with units of length, k is the thermal conductivity, and the change of temperature is between the isothermal surface of the ground and the channel wall [33].

The natural analytical baseline case would be the twenty-four, 1.27 mm diameter circular duct design. However, the analytical solution does not provide for an array of channels. Thus the baseline case is a single hole with a diameter of 5.08 mm. This diameter preserves the total surface area for the four holes. Note in the hexagonal shape, a construction line exists 1.27 mm in from the outer diameter of the inscribed inlet and outlet boss that is dictated by manufacturing issues. Thus minimum depth of the baseline case is z = 6.35 mm. The shape factor per unit length for the baseline cylindrical channel is 6.5.

Next, a set of dimensions was generated for embedded rectangular channels. A schematic of the layout in a one-sixth unit cell is in Figure 17. The channel width, a, was varied from 10 mm to 16 mm. The depth of the channel, H, was dictated by the width of the channel and the radial construction offset. The dimension H is found by the following expression:

$$H = r - \sqrt{(r - 1.27)^2 - a^2/4}, \tag{17}$$

where all dimensions are in millimeters. The channel height, b, was varied from 2 mm to 8 mm depending on the clearance available in a symmetric section of the hexagon. The bottom corners cannot penetrate past the symmetry lines. Furthermore, the corners can be no closer than 0.635 mm from the symmetry line to maintain the 1.27 mm spacing for manufacturing. The analytical shape factors for the rectangle are normalized by those for the single circular channel. The results are in Table 6.

The first major observation in the shape factor comparison is that all rectangular duct geometries yield a larger conduction shape factor than the chosen baseline case. The width does not have much effect on the shape factor, but the shape factor does

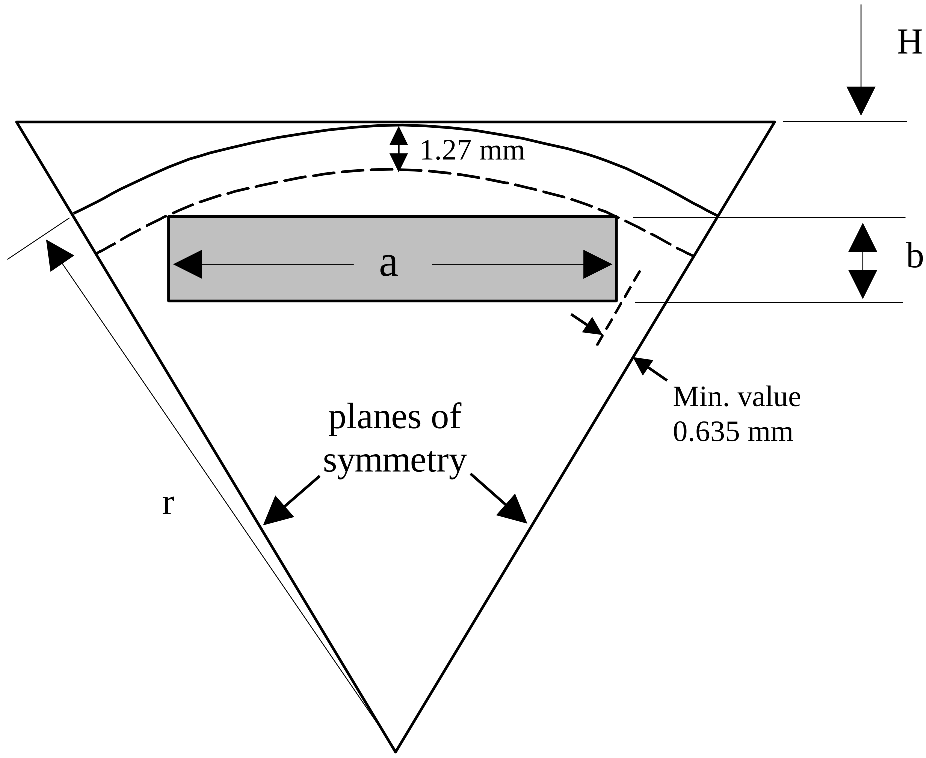

Figure 17. Schematic of a unit cell rectangular channel in hexagonal substrate

Table 6. Conduction shape factor ratio for rectangular duct/circular duct

Duct Width, *a* (mm)	10	11	12	13	14	15
Duct Depth, *H* (mm)	1.921	2.061	2.215	2.384	2.569	2.769
Duct Height, *b* (mm)						
1	1.12	1.13	1.13	1.13	1.12	1.11
2	1.18	1.19	1.19	1.19	1.18	1.17
3	1.22	1.23	1.23	1.23	1.22	1.21
4	1.25	1.26	1.26	1.26	1.25	
5	1.27	1.28	1.28	1.28		
6	1.29	1.30	1.30			
7	1.30	1.31				
8	1.32					

significantly increase with increasing height of the duct. This pattern is explained by the limitations on the geometry. The depth of the duct, H, increases as the width increases. The additional depth tends to maintain the H/a ratio nearly constant, which implies the H/b ratio will dominate any differences between dimensional combinations.

Determination of Actual Shape Factor Based on Simulation

To examine the benefit of the rectangular duct more closely, two-dimensional FEA models were developed to explore the effect of variations from the ideal analytical shape factor. The specific geometry in this study varies from the analytical case because it is not a semi-infinite medium. Also the heat source is a discrete length to simulate a chip as opposed to being applied over the whole boundary. In addition, the base line case is altered in the FEA comparison to reflect the four small circular holes in Figure 14. By defining constant temperature boundaries on the chip length of 10 mm and the flow channel walls of 1K and 0 K, respectively, and prescribing a thermal conductivity of 1 W/m/K, the shape factor per unit depth can be found by integrating the normal heat flux along the heat transfer surface.

The shape factor per unit depth for the baseline case as shown in Figure 14 is 5.27. The shape factors for the rectangular ducts were also calculated and normalized similar to the baseline duct layout. These runs were set up by looping the various dimensions in the MATLAB file of the model and running in a MATLAB with COMSOL link. The MATLAB code is in the Appendix. The results are shown in Table 7.

The results for the shape factor comparison in the simulations are not as beneficial as the analytical case. The largest improvement is 17%, and some rectangular ducts perform worse than the four holes. Unlike in the analytical comparison, the rectangular duct width does have an effect on the conduction shape factor; a maximum at a width of 11 mm is evident. In the more realistic comparison, the height of the duct has no significant effect on the improvement over the baseline design. These trends are most likely due to the discrete heat source. The only increase in "visible" heat transfer surface

Table 7. Comparison of rectangular shape factors to four circular channels via COMSOL

Duct Width, *a* (mm)	10	11	12	13	14	15
Duct Depth, *H* (mm)	1.921	2.061	2.215	2.384	2.569	2.769
Duct Height, *b* (mm)						
1	1.09	1.16	1.11	1.06	1.01	0.95
2	1.09	1.16	1.11	1.06	1.01	0.96
3	1.09	1.17	1.11	1.05	1.01	0.97
4	1.09	1.17	1.11	1.05	1.01	
5	1.09	1.17	1.11	1.05		
6	1.09	1.17	1.11			
7	1.09	1.17				
8	1.09					

comes with increasing the width. The height of the flow channel is essentially hidden from the heat source on the top of the hexagon.

Heat Transfer Enhancement

The total heat transfer enhancement is not limited to comparing conduction shape factors. The shape of the channel also affects the convective heat transfer. In the initial analytical estimation of the twenty-four ducts, the flow domain was established to be developing laminar flow. In the developing region, the heat transfer is enhanced over fully developed flow and is Reynolds number dependent. But for ease of comparison, fully developed flow is considered in this analysis.

Analytical

For a circular duct, the Nusselt number for fully developed laminar flow is 3.66 for a constant temperature wall [33]. No examination of the Nusselt number for a flux boundary is needed because the conduction shape factor analysis dictates a constant temperature duct wall. The Nusselt number is related to convective heat transfer by:

$$Nu = \frac{hD_h}{k}, \tag{18}$$

where h is the heat transfer coefficient, D_h is the hydraulic diameter, and k is the thermal conductivity. The convective thermal resistance is derived from Newton's law:

$$q' = hP\Delta T = \frac{\Delta T}{R_{conv}} \Rightarrow R_{conv} = \frac{1}{hP}, \tag{19}$$

where q' is the heat flux per unit depth, h is the heat transfer coefficient, P is the perimeter of the duct, ΔT is the temperature change from the transfer surface to the bulk temperature of the fluid, and R_{conv} is defined as the convective thermal resistance. The convective resistance for a single 1.27 mm diameter circular duct is 0.217 m·K/W. In a thermal resistance network, the convective resistances can be combined in parallel for an effective total convection resistance. For the four ducts in a symmetric unit cell, the combined convective resistance was 0.0544 m·K/W. The conduction resistance is derived in a similar manner from Eq. (16). For shape factor conduction, the resistance is $1/Sk$. The values for comparison were taken from the COMSOL derived shape factors. The total thermal resistance is the sum of the conduction and convection contributions, which is 0.244 m·K/W for the baseline case.

The convective resistance for the rectangular ducts is found in a similar manner. The only variation is that the Nusselt number varies with the rectangle's aspect ratio, a/b [33]. Several rectangular dimensions were explored from widths of 10 mm to 12 mm and heights of 2 to 4 mm. The resulting total resistances for each of these combinations are in Table 8, where they are normalized against the baseline thermal resistance of 0.244 m·K/W .

Improvement upon the twenty-four circular channels is only seen in two cases, 11x2 and 12x2. In this comparison, a smaller thermal resistance is desired. Only ratios less than one demonstrate a total heat transfer improvement. This improvement is on the order of 5%. Channels with a height of 1 mm were not considered because of the particulate requirement.

Table 8. Total thermal resistance for rectangular ducts normalized to the circular duct baseline design

Height, b (mm)	Width, *a* (mm) 10	11	12
2	1.012	0.943	0.951
3	1.156	1.070	1.070
4	1.283	1.189	1.189

Computational

Because the heat transfer improvement was small, FEA models were built to examine the effect of the discrete flux source in three dimensions. The model setup was similar to that explained in the circular duct FEA analysis. However, these models were prescribed simple plug flow to determine the lower bound, which would result in the best thermal performance. The models were of an 11 x 2 mm rectangular duct and a baseline circular duct array. The circular duct model is reexecuted under plug flow to have a better comparison as compared to the previously presented material. Alumina was used as the ceramic material. The maximum temperature results from these models are in Table 9.

In these models, the circular duct design resulted in much lower temperatures as compared to the rectangular duct. This conclusion is in contrast to the thermal resistance comparison with fully developed laminar flow. This result is due to the difference in flow area. The rectangular duct provides more than four times the cross-sectional flow than the circular array. The increase in area results in a decrease in velocity and a decrease in heat transfer.

Figure 18 shows the outlet temperature distribution for the rectangular duct. Like the circular duct, a large percentage of the flow remains at the initial inlet temperature. The heat does not penetrate well into the fluid. Overall, the rectangular duct design did not meet the design parameters and ultimately provides no improvement upon the circular duct design.

Table 9. Plug flow model temperature (°C) results for free flow in rectangular and circular ducts

	Rectangle	Circles
Wall	147.7	129.9
Chip	162.6	143.4

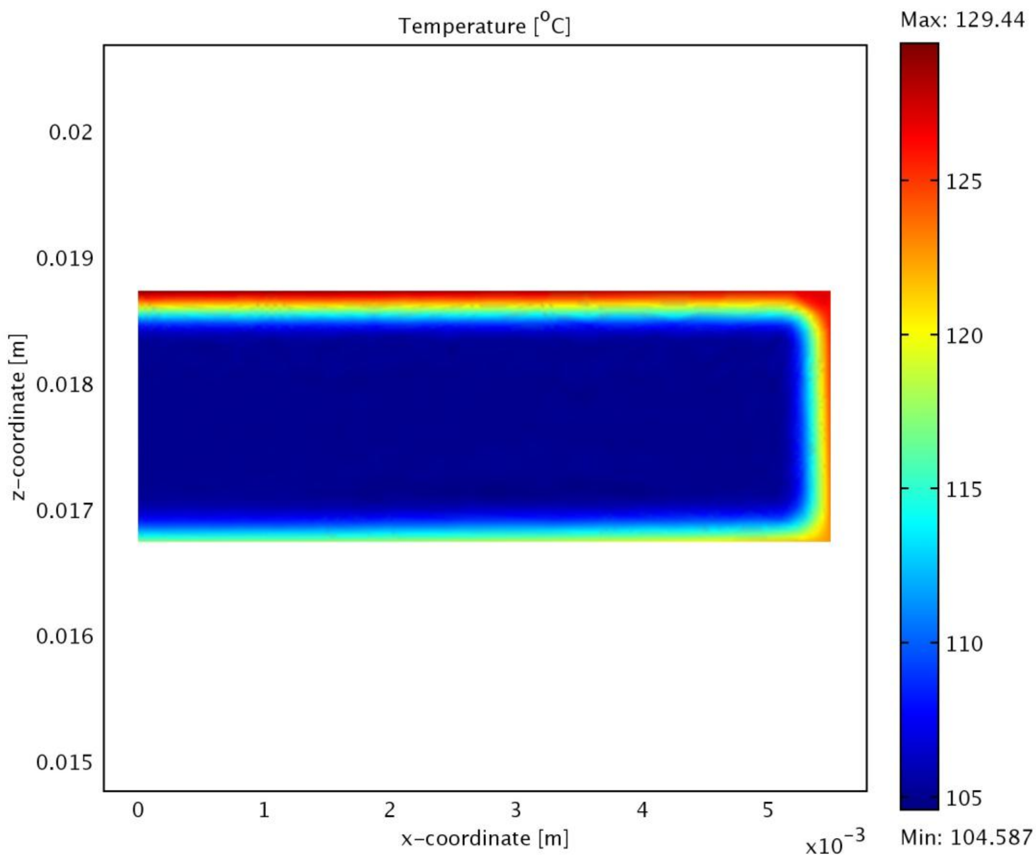

Figure 18. Outlet temperature distribution for plug flow in rectangular duct

The circular duct also had lower temperatures as compared to the fully modeled flow field in Figure 12. The better performance is explained by the application of plug flow and the larger hexagonal geometry. The current model setup provides the absolute lower bound for temperature. Since wall temperatures in Table 9 are above the design criteria of 128°C, further iterations are necessary to find a successful duct layout.

Triangular Duct

To seek a slight improvement, a triangular duct was considered. No analytical conduction shape factor was found in literature, but a two-dimensional model was built. The trends were similar to the rectangular duct in that no variation was evident with increasing triangle height. The conduction shape factor improvement was only 6%. A plug flow model for a triangle with a base length of 10 mm and height of 3 mm resulted in wall temperature of 144.2°C. This duct shape is also not feasible. Other design alternatives must be sought besides simple changes in free flow duct geometry design.

The plug flow models' maximum fluid wall temperatures exceeded the design specification. In real developing flows, the addition of viscous effects will only make the wall and chip temperature worse. Furthermore, the temperature distributions shown in Figure 13 and Figure 18 show that large potential cores exist in the flow channels. A design with thermal conductivity enhancers could be implemented to utilize more of the coolant. Even small increases in the effective thermal conductivity of the working fluid would provide dramatic improvements because the thermal conductivity of the working fluid is two orders of magnitude less than the lowest value of thermal conductivity for a ceramic.

Chapter 4 - Porous Media Designs

In the free flow configurations, the thermal penetration into the fluid was small, and a large fluid core remained at the inlet temperature. Heat transfer enhancements were explored to better utilize the available coolant. General methods of enhancing the heat transfer include extended surfaces, micro surface structures, microchannels, and metal foams. Mass-market ceramic manufacturing techniques do not yield to fine extended surfaces. Furthermore, many microstructures or microchannels could not meet the OEM requirement of being able to pass a 1 mm particle. Therefore, the design alternative to increase the effective thermal conductivity of the coolant was to introduce a coarse structure metal foam. The foams of interest are specified from manufacturers as 10 PPI. This size cell structure would still allow for the design to meet the particulate requirement established by the OEMs.

All models presented in this chapter are evaluated using COMSOL under steady three-dimensional constant-power assumptions.

Theory

Porous media is analyzed using three basic models. The Darcy model assumes a plug flow or uniform velocity profile. This type of flow describes slow creeping flows typically found in packed beds, soil, or other porous media. For Darcy flow, the pressure gradient (∇p) is proportional to the velocity field ($\vec{u}$) and it is representative of the viscous drag (skin friction effects) in porous media:

$$\nabla p = -\frac{\mu}{\kappa}\vec{u}, \tag{20}$$

where the dynamic viscosity (μ) and the permeability (κ) are proportionality constants. In this model, this flow field does not have to be explicitly solved because of the uniform profile. The average velocity is directly prescribed in the convection mode of COMSOL. The velocity is based on a reduced area that is described by the porosity of the foam. The porosity is the ratio of the void volume to the total volume of the porous media. From literature, the porosity (ε) was chosen to be 0.89 [40].

The next porous media model is the Brinkman model. It takes into account the viscous shear effects at the inner wall of the flow channel, which results in a parabolic velocity profile. From a boundary condition point of view, it allows for a no-slip condition to be applied on the foam/wall boundary instead of the slip condition inherent in the Darcy model. Brinkman originally added the Darcy (viscous drag) contribution to the pressure gradient to the fully developed incompressible Navier-Stokes equation (viscous shear) to describe flow in a packed bed of spheres [41, 42, 43]. In the COMSOL implementation of the Brinkman equation, the viscous shear viscosity is scaled by porosity:

$$\nabla p = -\frac{\mu}{\kappa}\vec{u} + \frac{\mu}{\varepsilon}\nabla^2\vec{u} \tag{21}$$

The Brinkman model is still limited to slow creeping flows that would typically be described by Darcy's model. The advantage of the Brinkman model is that it can be coupled with free flows, i.e. flow without porous media, to solve free/porous flow systems.

However, the Darcy model and Brinkman extension do not account for the form drag contribution as the flow rate increases above the laminar, creeping flow regime. Forchheimer accounted for the form drag. The Darcy-Forchheimer model adds a quadratic relation to velocity field in the pressure gradient [42, 43]. The Darcy-Forchheimer model is:

$$\nabla p = -\left(\frac{\mu}{\kappa} + \frac{\rho C_f |\vec{u}|}{\sqrt{\kappa}}\right)\vec{u}\ , \tag{22}$$

where C_f is the Forchheimer form drag coefficient and ρ is the density. The Forchheimer term can be added to the Brinkman formulation in COMSOL as a source term as shown in Eq. (23) [44]. This application allows for the no-slip condition to be maintained at the fluid-wall interface and account for turbulent mixing in the foam/fluid matrix [44, 45].

$$\left(\frac{\mu}{\kappa}\right)\vec{u} = \nabla \cdot \left[-p\,\mathrm{I} + \frac{\mu}{\varepsilon}\left(\vec{\nabla}\vec{u} + (\vec{\nabla}\vec{u})^{T}\right)\right] - \frac{\rho C_f \left|\vec{u}\right|}{\sqrt{\kappa}}\vec{u} \tag{23}$$

One important assumption made in using these formulations with a single energy equation to solve for the heat transfer is the application of local thermodynamic equilibrium. In short, this assumption allows for the fluid/foam matrix to be modeled with average bulk properties instead of describing the minutia of the porous foam. More background information on the history of these formulations and on local thermodynamic equilibrium can be found in Norton's work [44].

For the early computer models in this research, Darcy's model (plug flow) was used to evaluate the thermal performance of varying flow channel geometries and hexagonal prism sizes. Despite efforts by several authors to generalize flow behavior by permeability based Reynolds numbers [41, 42], no generalized theory for open celled foams has proven to be conclusive about discerning appropriate flow regimes (Darcy or Darcy-Forchheimer) outside of specific experimental data sets. In this case, Darcy flow was justified based on the hydraulic Reynolds number for the flow channel, which was well within the laminar flow regime. Furthermore, Darcy flow is easy to implement in COMSOL to focus the selection of specific duct sizes, shapes, and placement. Once suitable geometries are found, more rigorous attention will be given to the different flow models to examine their effect on thermal performance.

Darcy Porous Media Models for Designs of Hexagon Substrate with 12 mm Sides

As mentioned previously, a cost analysis was performed on hexagonal designs with a flat width of 12 mm. This analysis was conducted on the circular duct design and on two other hole configurations with metal foams inserts. These designs are briefly discussed here to show progression of thought toward the final designs. More details of these designs and results were included in the annual ORNL report [38].

Four-hole Design

Figure 19 shows a hexagon cross-section with four holes; each would be filled with a metal foam insert. The section in the rectangle is the unit cell that is modeled. Four holes were investigated instead of six because the design uses fewer pieces, i.e. lowers cost and simplifies the assembly. Also the diodes generate less average heat load, which may not require a dedicated flow channel. The flow channel is offset some from the center of the side as a consequence of maintaining the minimum construction offsets (0.050”) in the ceramic. The offset benefited the design by balancing the different heat loads from the near and far side.

For this design, the size of the holes was determined by maintaining at least two pores across the diameter (~5 mm) and adjusted for the best thermal results from Darcy (plug flow) models. As the diameter grows, the inlet velocity decreases for a fixed flow rate, but some benefit is gained in increased surface area. The maximum size was limited by the ceramic manufacturing limitations.

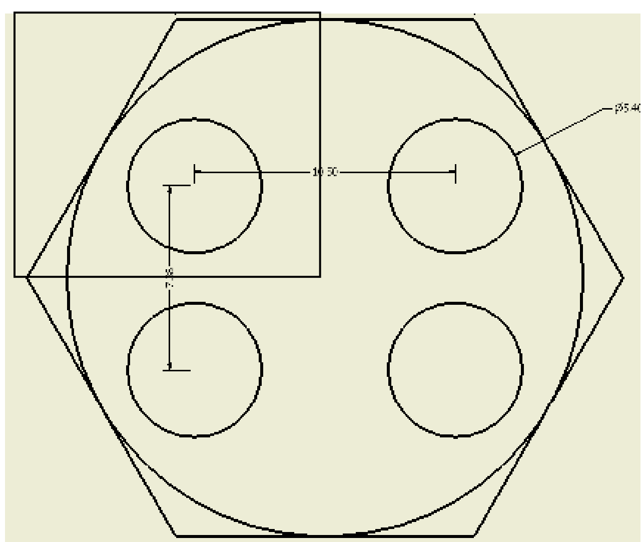

Figure 19. Sketch of four-hole design for 12 mm hexagon

Single-hole Design

Figure 20 shows the general shape of the single-hole design for the 12 mm hexagon. The hole in the center is 9mm in diameter and is filled with a copper or aluminum foam insert. The triangular section represents the symmetric unit cell that was modeled. Decreasing the number of flow channels to one allows for much simpler construction and manufacturing. This design would also be easier to evenly distribute flow through a header for final inverter construction.

Simulation Results and Conclusions

The commercial software package COMSOL, developed for modeling multi-physics problems, was used for the analysis in this project. The thermal load for four switches and two diodes was used for the computational results shown in Table 10. Plug flow was prescribed to the flow channels based on the assumption of Darcy flow.

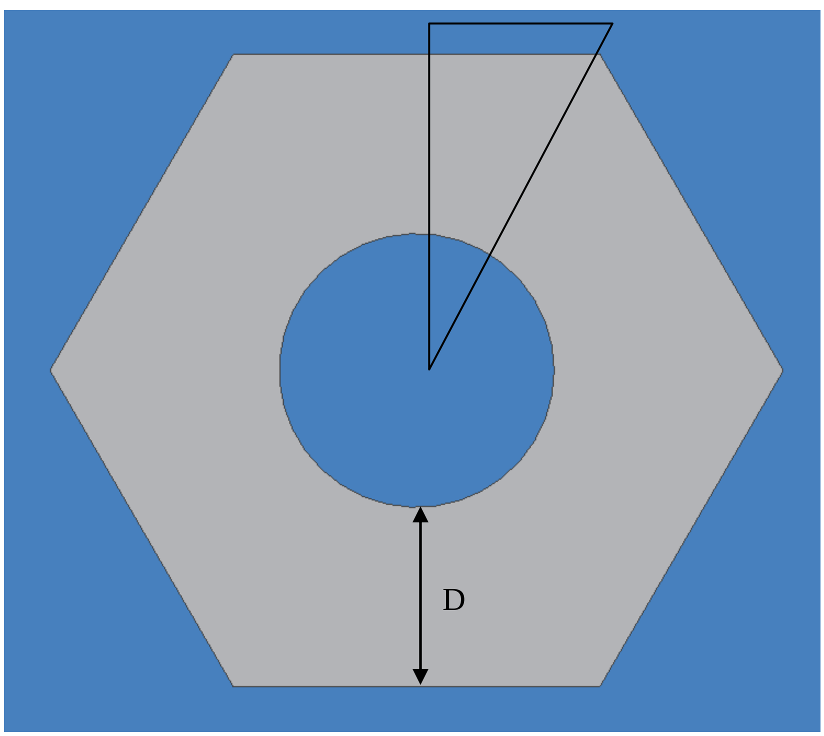

Figure 20. Sketch of single-hole design

Table 10. Thermal performance of 12 mm hexagonal designs from COMSOL models

Design	Free-flow Circular Duct				Four-hole							
Description	24-holes 1.27 mm diameter				***copper foam***				***aluminum foam***			
Ceramic Insulator	AlN	BeO	SiC	Alumina	AlN	BeO	SiC	Alumina	AlN	BeO	SiC	Alumina
Performance at 2.5 GPM for the whole inverter												
Max Projected Junction Temperature (°C)	141.7	143.0	144.7	**182.9**	126.5	127.6	128.8	**167.5**	129.3	130.6	131.9	**171.5**
Max. Fluid Temperature (°C)	**136.5**	**137.5**	**138.8**	**163.0**	119.0	119.4	119.8	126.6	122.7	123.1	123.7	**133.4**
Required Flow Rate to Meet Thermal Limits (GPM)	>7.25	>7.95	>8.67	LARGE	2.5	2.5	2.5	2.5	2.5	2.5	2.5	>3.88

Design	Single-hole							
Description	***copper foam***				***aluminum foam***			
Ceramic Insulator	AlN	BeO	SiC	Alumina	AlN	BeO	SiC	Alumina
Performance at 2.5 GPM for the whole inverter								
Max Projected Junction	137.3	138.8	140.9	**219.5**	142.3	143.8	145.9	**224.4**
Max. Fluid Temp	120.5	120.6	120.7	121.4	126.1	126.3	126.4	127.9
Required Flow Rate to Meet Thermal Limits (GPM)	2.5	2.5	2.5	LARGE	2.5	2.5	2.5	LARGE

These results include aluminum and copper foam for the four-hole and single-hole designs. For comparison, the results for the circular duct are also shown. The projected junction temperature is based on the chip/substrate interface temperature and an approximated thermal resistance of the solder joint and chip. These temperatures are typically less than 2°C greater than the interface temperature. The maximum fluid temperature is found on the wall of the flow channel nearest the heat source(s). Temperatures that exceeded the design criteria are highlighted in red. The green highlights are to denote switch temperatures above the design criteria of 150°C but below the maximum junction limit of 175°C. If the predicted temperatures at 2.5 GPM did not fall within the design criteria, the flow rate was increased. The flow rates where thermal limits were met are also reported.

Furthermore, this study showed the effect of different ceramic substrate materials. From a thermal point of view, the thermal conductivity should be as large as possible to create a compact substrate. The results in Table 10 show that all foam designs with the higher thermal conductivity materials, i.e. AlN, BeO, and SiC, met the thermal design criteria at a flow rate of 2.5 GPM. The circular duct design kept the switch temperature below the design criteria but exceeded the boiling point of WEG. The simulations do not account for phase change in boiling; thus, any model results, which predict temperatures greater than the boiling point, are invalid. However, one can deduce that if the maximum fluid temperature was decreased, then the chip temperatures would also decrease from their present value and be maintained within the design limits. The alumina, which has the lowest thermal conductivity, performed poorly.

For the successful models where both switch and fluid temperature were below their design criteria, the thermal load was increased by using three switches and two diodes. The change in chip population increased the dissipation of the switch to 73 W/switch. The temperatures remained within the design limits for the copper foam models and the four-hole aluminum foam model. However, the margin of safety with respect to the maximum performance criteria was drastically reduced. While some cost advantage could be realized by a reduction in silicon, the reliability of the inverter would decrease. Thus, the four switch and two diode population was used for the rest of the research.

At this point in the research, the cost study was initiated. Alumina has long been a standard material in power electronics; hence, it is the cheapest. The other materials have been used in high performance parts but are generally newer to the widespread market. This specialty use greatly increases the cost of the higher thermal conductivity materials to a point of being prohibitively expensive. Therefore, alumina would have to be the ceramic used for further design considerations. For applications, such as defense, where performance may be more crucial, these designs and material choices are still viable options.

Also aluminum foam was decided upon as the foam of choice to move forward. Despite the better thermal performance of the copper foam, no domestic supplier could be found. Furthermore, the manufacturing process for the copper foam presents many environmental hazards. Also WEG compatibility with aluminum is well known, and the two materials are widely used in the automotive industry. Introducing copper into a system that contains aluminum could potentially cause unwanted corrosion.

Design Optimization for Alumina

Exploring a viable alternative geometry that uses an alumina substrate is desirable because of its low cost, availability, and mature manufacturing techniques. To tame the high projected junction temperature of the alumina substrate, some geometry changes must be made instead of a simple velocity increase.

Single-hole

The single-hole design was chosen to explore rough sizing of the alumina substrate because the dimensional variations were simpler to manage for parametric studies. The overall dimensional conclusions could then be used as a basis for exploring improvements to the four-hole design, which had better thermal performance in the earlier simulations. The first modification was to increase the center hole radius in

Figure 20. Again, all the flow models were based on an assumed Darcy flow. The radial increase resulted in lower interface temperatures but increased the fluid temperature beyond the operational limit. From these results, a distance of 6 mm from the hexagon side to the outer radius was found to maintain the fluid temperature around 128°C. This dimension is shown in Figure 20 as D. To decrease the interface temperature and thus the projected junction temperature, the overall size of the hexagon was increased. The radius of the hole grew as the hexagon side width increased. D was held constant at 6 mm. The inlet velocity was recalculated in each case to maintain a total inverter flow rate of 2.5 GPM. Figure 21 shows the trends for a range of hexagon side widths.

At first glance, these changes seemed to have produced a semi-viable geometry. With a hexagon side width of 24 mm, both temperatures of interest are below their absolute maximums of 175°C and 130°C but above the design criteria of 150°C and 128°C.

In an attempt to improve on these modifications and reduce the fluid wall temperature, D was increased to 7 mm, and the results are shown in Figure 22. As expected, the fluid temperature decreased, but the interface temperature increased as compared to Figure 21. Therefore, the hexagon side width had to increase more to decrease the interface temperature. At a side width of 32 mm, the interface temperature is 166°C while maintaining a maximum fluid temperature near 128°C. While these improvements offer a low cost alumina solution, the geometry must significantly increase in size and volume.

Annulus

Another way to decrease the fluid wall temperature and interface temperature is to increase flow rate by decreasing the cross-sectional area of the flow channel. Since the core of the single-hole design remains at the inlet temperature, an annular design was considered. Figure 23 is a sketch of this geometry.

In this geometry, the minimum distance from the hexagon side to the flow channel D can be smaller than in the previous models. This smaller distance is a result of an increase in local velocities created by the annular shape.

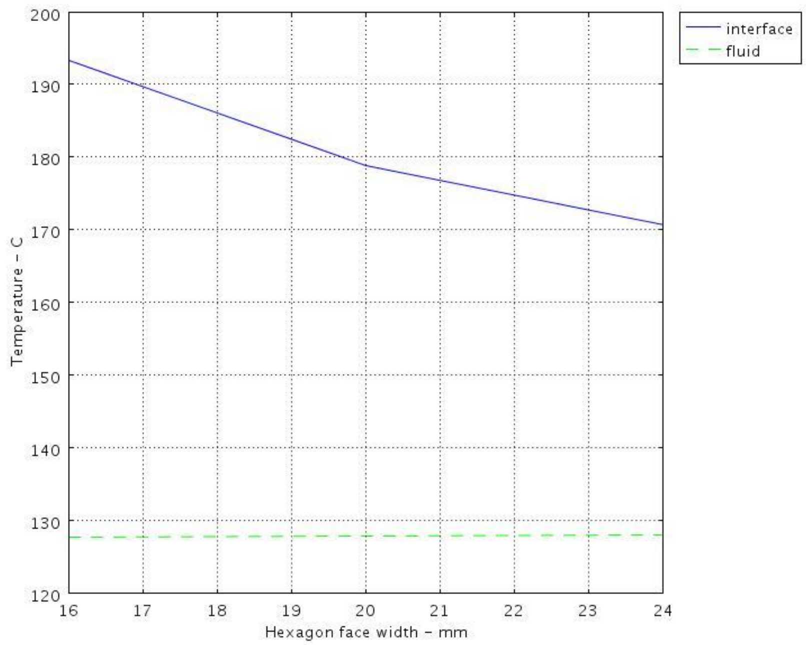

Figure 21. Maximum interface and fluid temperature for single-hole geometry with aluminum foam, D = 0.006 m

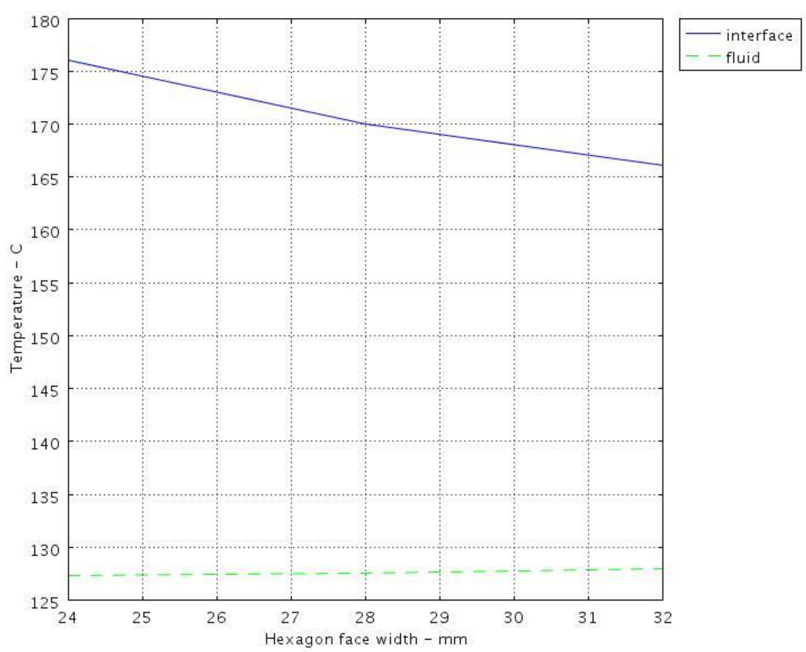

Figure 22. Maximum interface and fluid temperature for single-hole geometry with aluminum foam, D = 0.007m

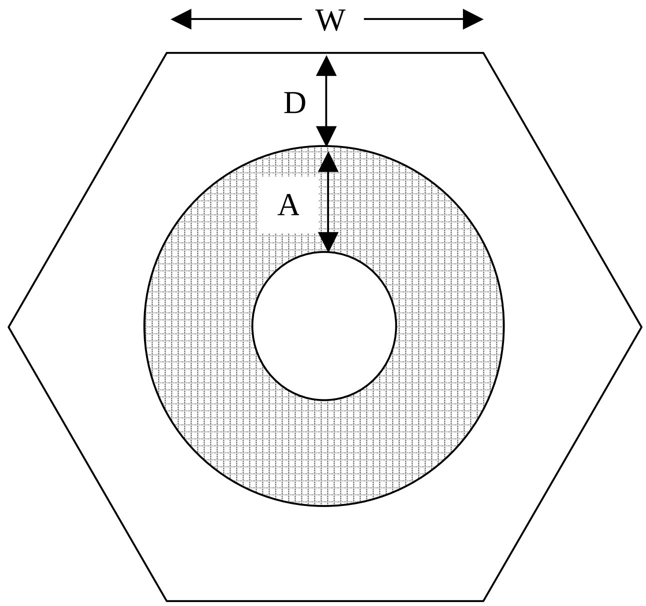

Figure 23. Schematic of annular geometry

For the model, D = 3.4 mm was used to maintain the fluid wall temperature below the design criteria. The annulus thickness, A, was 5 mm. Five millimeters was chosen based on the general dimensions of the aluminum foam matrix. For smaller annulus thickness, the foam would not have enough structural integrity. The radii were determined based on these parameters and the hexagon side width. The inlet velocity was determined based on a constant inverter flow rate of 2.5 GPM. Figure 24 shows the maximum temperatures for this design as a function of W, the width of the hexagonal face. The interface temperature is lower for a given side width than in the single-hole design.

Also the maximum fluid temperature decreases with increasing side width. This trend is the opposite of the single-hole design trend. At a side width of 18 mm, the temperatures are within the maximum limits of the design and below the maximum temperatures of the single-hole design with a larger substrate. To increase reliability of the power electronics and strive to meet the design criteria instead of the maximum allowable temperatures, the hexagon side should be increased more.

At a side width of 24 mm, which is twice the original width of 12 mm, the maximum interface temperature is 152°C, and the maximum fluid temperature is below

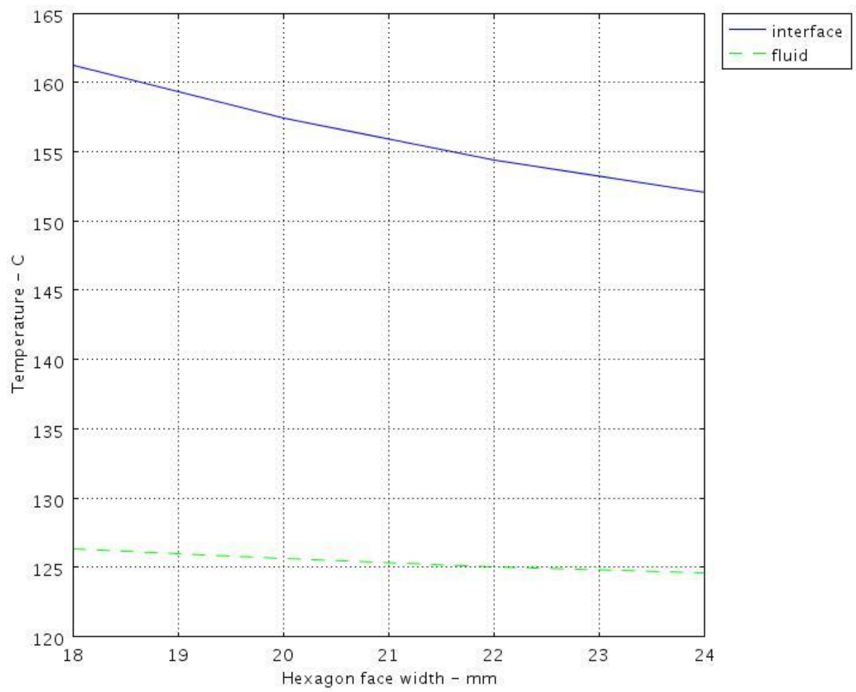

Figure 24. Maximum interface and fluid temperature for annular hole geometry with aluminum foam, D = 0.0034 m and A = 0.005 m

125°C. These temperatures demonstrate great improvement over the single-hole performance. Further optimization of the distance D could be explored to obtain temperatures below the design criteria because the maximum fluid temperature could increase slightly and still be below the design limit of 128°C.

Four-hole

A hexagon side width of 24 mm was shown to be a viable substrate size for the annular flow channel. Because its initial thermal results were promising, this same size substrate was reexamined here with a four-hole channel design. With the overall size established as a regular hexagon with 24 mm sides, the geometry of interest turned to the flow channel size and placement. Successive design iterations led to the final design, which a quarter section is shown in Figure 25.

For this design, the operational load was altered from 55 W in both chips to 55 W in the side chip and 37 W in the top chip. This waste heat distribution better represents

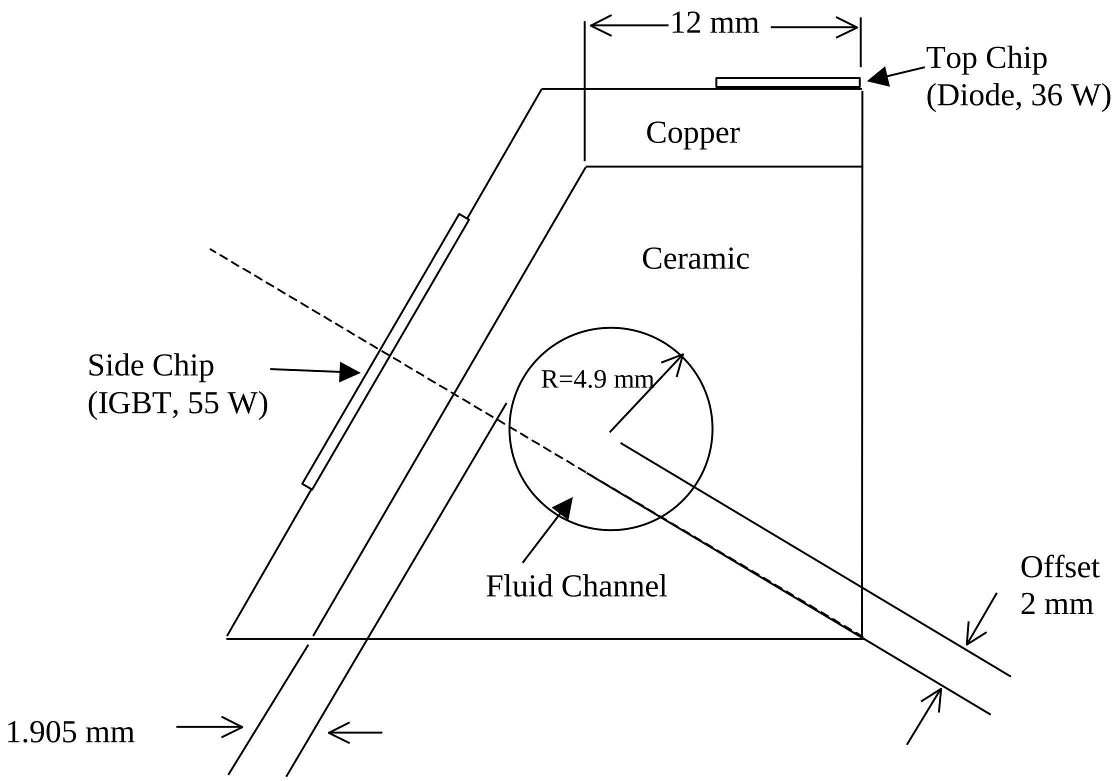

Figure 25. Schematic of four-hole alumina design

the load of an IGBT on the side and a diode on the top of the DBC structure. Furthermore, the optimum placement of the coolant channel is dependent on the heat load. By using a more realistic heat load, the geometry could be determined to provide the lowest maximum temperatures. The results shown in Figure 26 are for the four-hole alumina substrate design as the position of the hole was offset from the center of the side chip. The reported temperatures are the maximum temperatures on the respective surface, as labeled in Figure 25. The center of the flow channel was started at the center of the chip and offset in 1 mm intervals in a parallel direction to the side of the hexagonal substrate. The preferred offset dimension in Figure 25 is the one that has the maximum temperature in both devices to be about the same. The preferred offset was 2 mm. More discussion of this parametric study is in the Appendix.

For the geometry shown in Figure 25, the maximum temperature in the IGBT was 150.3°C and in the diode was 149.3°C. The maximum fluid temperature was maintained at 128.5°C. All of these temperatures are within 1°C of the design criteria.

Compared to the annular design, this design would involve four aluminum foam inserts. The overall size of the two designs is the same, and the thermal performance is nearly identical. The annular design initially seems to be a simpler design to manufacture. Commercially available tubes can be purchased with aluminum foam brazed on the exterior surface. By closing up the ends of a tube, the annular structure could easily be made. The four aluminum foam cylinders can be purchased to the exact size. However, four pieces are needed for each substrate. On a prototype level, the cost for the single brazed tube is about 50% more than the four aluminum foam cylinders.

Both the annular and four-hole designs provide structures that warrant further examination. Their thermal performance is comparable. For future investigation, both designs will be considered to evaluate their advantages and disadvantages.

Brinkman and Brinkman-Forchheimer Porous Media Models

To this point, the design decisions primarily relied on the thermal models of simplified symmetric unit cells of the direct cooled substrate. These models were

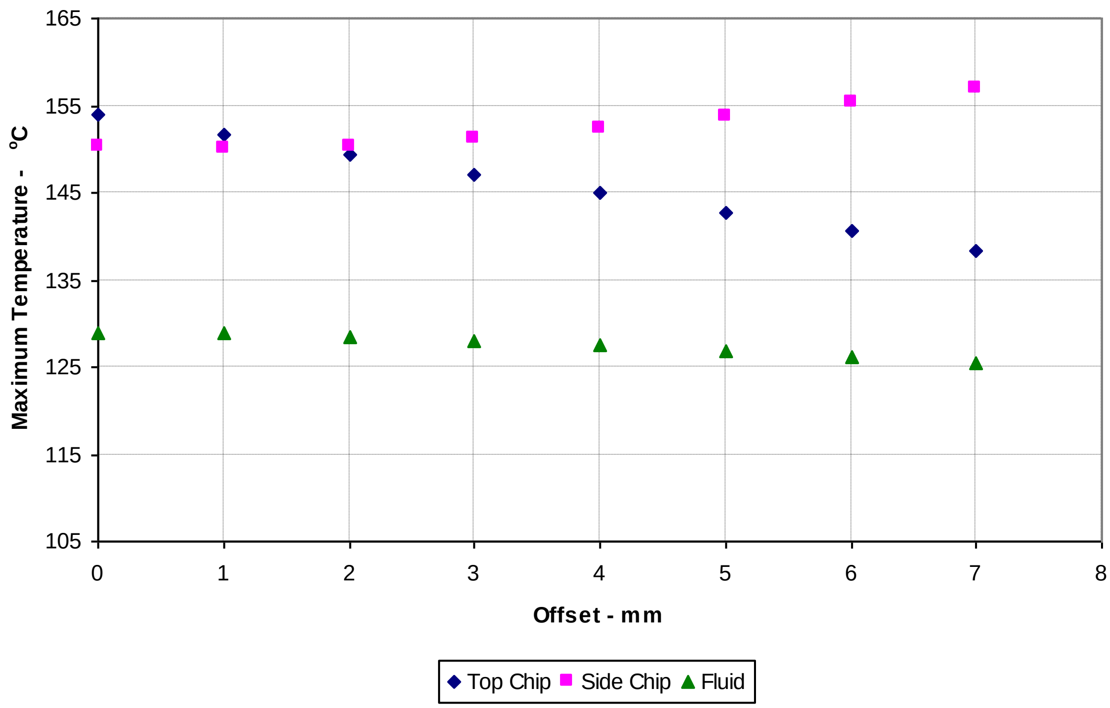

Figure 26. Maximum temperatures in four-hole design with heat load of 36 W for the top chip and 55 W for the side chip

designed to present conservative thermal boundary conditions to result in more robust designs and to arrive a feasible geometric configurations. The overall simulated chip load was higher than the actual case because some diodes will replace the switches. The geometry was also simplified as compared to final net shapes, i.e. no wire bonds and few other fine details.

One simulation that was not conservative was the modeling of the flow through the metal foam. The flow through the metal foam was modeled as plug flow under the assumption of Darcy flow. Before fabricating the selected geometries, it is important to better understand the intricacies of the thermal behavior. Therefore, further models were created to incorporate more geometry detail and the other porous media flow models.

These models include more geometry detail such as rounded ends, wire bonds, actual chip sizes, and thermal loading based on the specific device load. Because of the more detailed thermal load, the symmetric section is a quarter wedge for both designs. In the previous work the annular design was modeled as a one-twelfth section, and the four-hole was modeled as a quarter wedge. The models evaluated to this point had a copper cladding thickness of 0.050” (1.27 mm), which was required for heat spreading. The first quote from a vendor was to clad the substrate with 0.020” (0.5 mm) thick copper. This thickness was the limit of their manufacturing capability. A few models were run to determine the effect of copper thickness on the junction temperature. The thinner cladding increased the junction temperature of the chip by 5ºC. Thus the copper cladding should be as thick as possible. Another vendor was able to provide a quote for 0.050” thick cladding; therefore this thickness was used for these detailed thermal models.

Because the flow properties of the thermal enhancing metal matrix were unknown at this time, the three porous media flow models were run for each design case to establish an operational range. The Darcy flow model will result in the lowest temperature predictions because of the lack of boundary layer effects. The Darcy model forms the lower bound of the operational range.

The parameters used for the porous media models were taken from literature [40]. The porosity was 0.89, which was consistent with the earlier Darcy models. The permeability for aluminum foams with similar specifications is on the order of $1\text{x}10^{-8}$ m^2. This low permeability provides a high flow restriction that increases the difficulty of obtaining a converged solution for all three porous media models. For a basic comparison and simpler computational scheme, the permeability was set to $1\text{x}10^{-4}$ m^2. The larger permeability will raise the upper bound of the operational range, but will allow the general relation between the three porous media model to be established. If the operation range is within the design criteria with the larger permeability, decreasing this value will only help the thermal performance.

Because the Brinkman model allows a no-slip condition at the wall, a finite velocity gradient will exist at the fluid/wall interface. The decrease in velocity gradient at the channel wall results in less heat transfer to the fluid. Of the three porous media models, the Brinkman model produces the highest junction and fluid temperatures. It forms the upper bound of the operational range.

A Brinkman model with a Forchheimer correction flattens the velocity profile. The more uniform profile increases the velocity gradient near the wall, which causes more local heat transfer. This effect lowers the maximum temperatures as compared to the Brinkman model but not to the point of equaling those from the Darcy model. The Brinkman model with the Forchheimer correction is believed to yield more realistic results because it accounts for the added flow resistance resulting from the form drag in turbulent flow. The initial Forchheimer friction coefficient (C_f) was calculated from a correlation by Amiri [46] where ε is the porosity

$$C_f = \frac{1.75}{\sqrt{150\varepsilon^3}}. \tag{24}$$

Annular Design

To correctly model both IGBT and diode placement, a quarter symmetry section is used as shown in Figure 27.

Darcy Results

Figure 28 shows a temperature distribution along the fluid channel wall for the Darcy model. The coordinates are face parameters that describe the location as a fraction

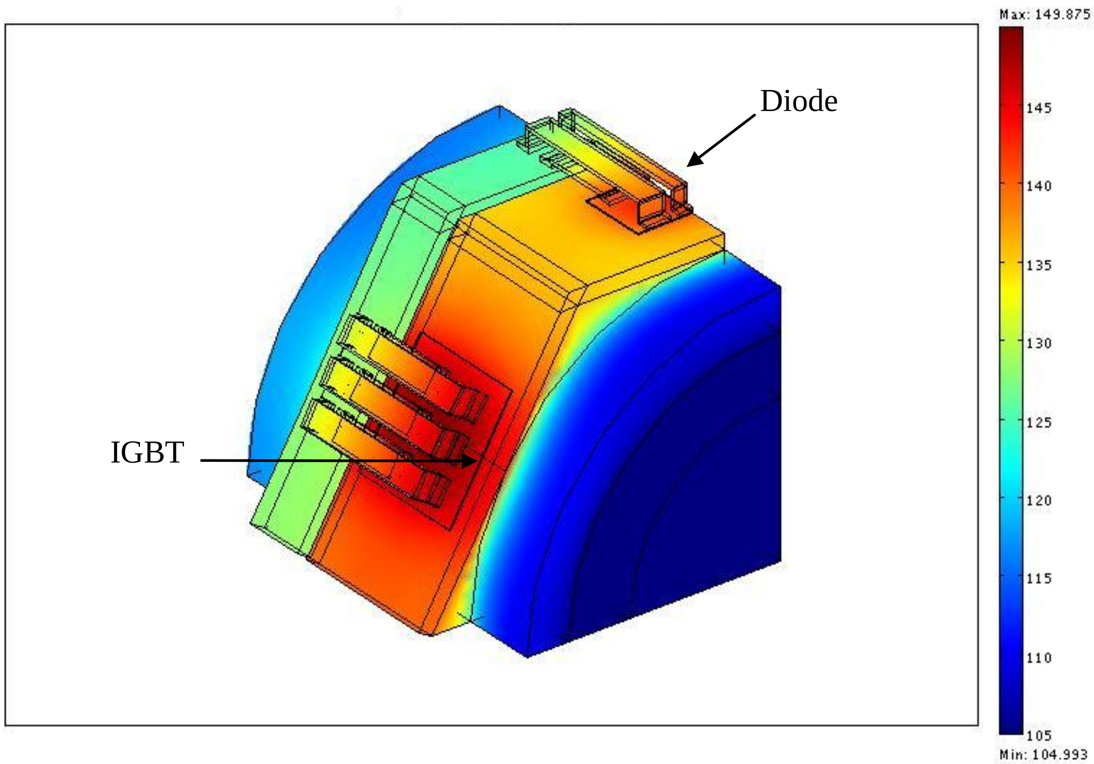

Figure 27. Quarter symmetry geometry with IGBT and diode

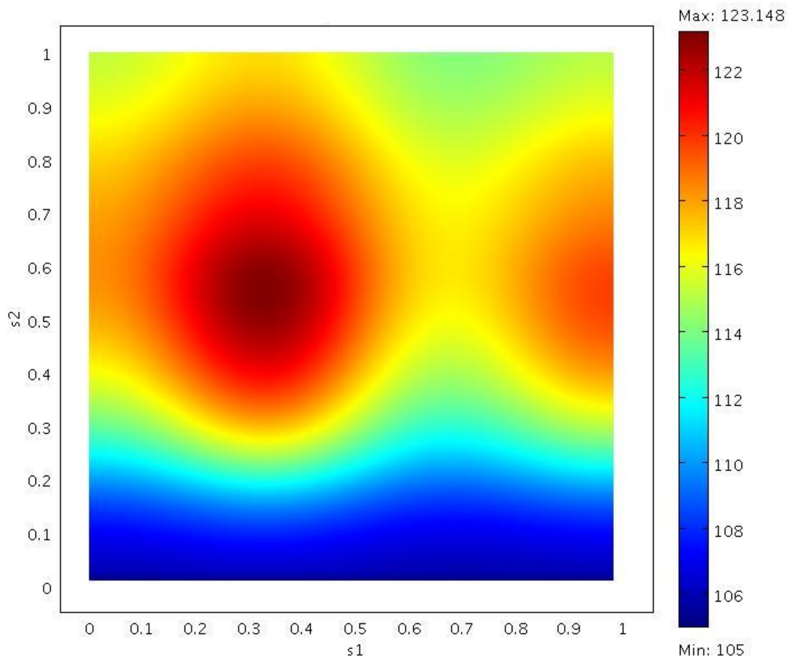

Figure 28. Flow channel wall temperature (°C) in Darcy flow model

of the total length of the quarter circumference (s1) and axial length (s2). The larger high temperature zone represents the thermal footprint resulting from the IGBTs and the smaller one at the right is that of the diodes. The maximum fluid temperature is well within the design specifications, and heat is spread well towards the exit plane, which would be at the top of the figure. Because of the additional conduction paths and reduced load on the diodes, the simulated maximum temperatures are less than predictions from the original models. The maximum IGBT and diode temperature were 149.9°C and 143.5°C, respectively. The maximum fluid temperature was 123.1°C.

Brinkman Model

The Brinkman porous media quarter symmetry model setup was identical to the quarter symmetry Darcy model except for the velocity field. The heat does not spread as much in the axial direction as shown in Figure 29. The hot zone does not extend as far toward the outlet as it does in the Darcy model. This indicates less heat transfer to the fluid, which raises the chip and fluid temperatures. The maximum IGBT temperature is

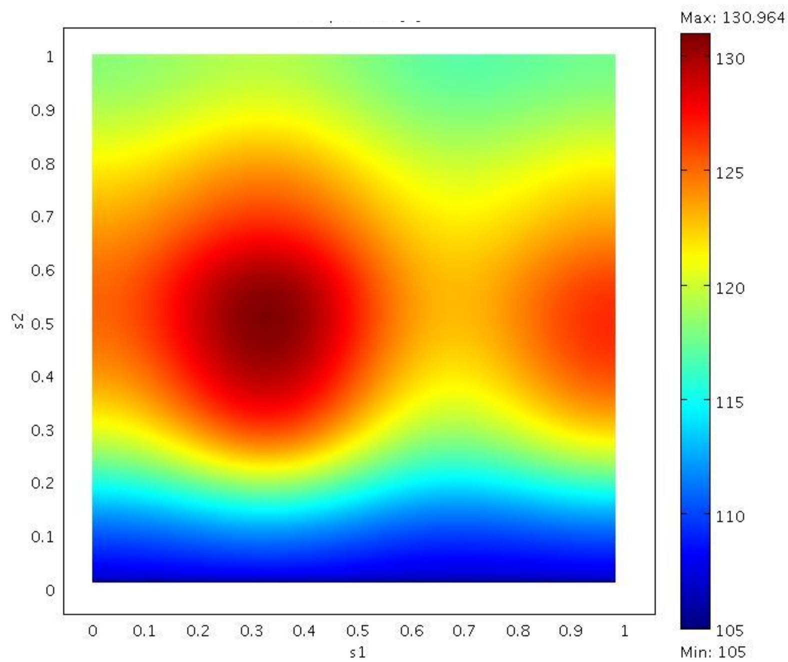

Figure 29. Flow channel wall temperature (°C) in Brinkman flow model

6.7°C hotter than in the Darcy flow model. This temperature is above the desired 150°C but still below the absolute maximum of 175°C. The diode temperature is still below the desired 150°C, and the maximum fluid temperature exceeds the boiling point of 50/50 water-ethylene glycol.

The Brinkman model, however, tends to be less accurate for very porous material like the foam in consideration because it assumes laminar flow. The foam structure creates mixing and turbulence which should be taken into account.

Brinkman-Forchheimer

The Forchheimer correction adds the effect of turbulence to the fluid/foam matrix and flattens the velocity profile. Figure 30 shows the fluid channel wall temperature distribution. The relative distribution is mostly unchanged as compared to the results from the Brinkman model in Figure 29. The primary difference is that the temperature magnitude decreased by 2°C to a point below the boiling point of 50/50 WEG.

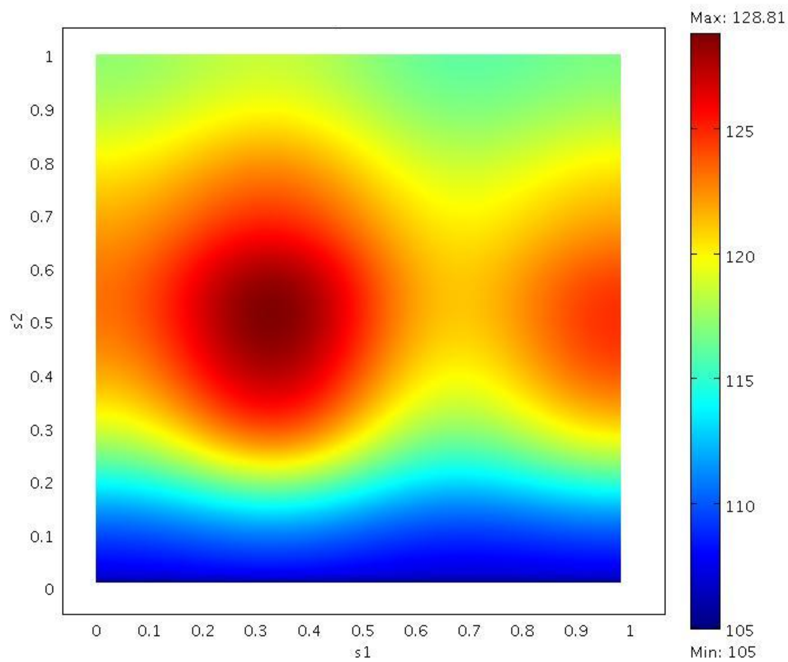

Figure 30. Flow channel wall temperature(°C) in Brinkman flow model with Forchheimer correction

A comparison of the three velocity profiles is shown in Figure 31. The flatter profile increases the velocity near the wall, which causes more local heat transfer. This effect lowers the maximum temperatures as compared to the Brinkman model but not to the point of equaling the Darcy model. Table 11 summarizes the results for the three flow models.

Four-hole Design

Recall that the alumina four-hole design was based on the specific device heat load for the switch and diode; however, both devices had the same footprint. This necessity for the specific loading in the original design arose from the placement of the hole as detailed in Figure 25. The hole position relative to the center of the switch resulted in an effect on both the switch and diode temperature, which was also dependent on the device's thermal load. Thus, not much change is expected in the results with the addition of these geometry details for this final design. Moving the flow channel closer

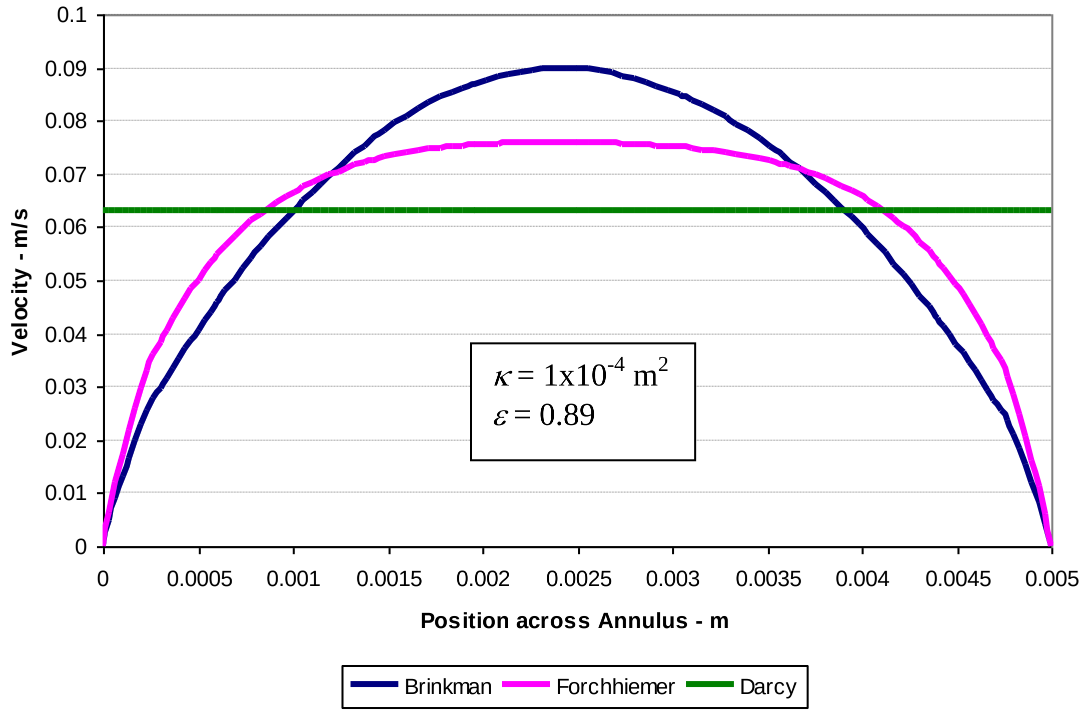

Figure 31. Comparison of velocity profiles for annular design

Table 11. Summary of results for the annular design

Maximum Temperatures	**Darcy**	**Brinkman**	**Brinkman with Forchheimer Correction**
T_{IGBT} ºC	149.9	156.6	154.8
T_{diode} ºC	143.5	149.7	148.1
T_{fluid} ºC	123.1	131	128.8

to the diode would decrease the temperature but increase the IGBT temperature. If this geometry is chosen as a preferred design for the final inverter and the experimentation verifies the modeling procedure, a parametric study would be necessary to find the optimal placement based on the actual chip and diode dimensions.

The Darcy model resulted in a maximum fluid wall temperature close to the maximum allowable temperature. Based on the fluid wall temperature increase from the annular results, the expectation is that the other flow models will result in fluid temperatures which exceed the boiling point. Modeling the Brinkman and Forchheimer correction confirm this hypothesis. A summary of the results is in Table 12.

The other flow models resulted in large increases in the predicted junction temperatures. The chips can theoretically survive at these temperatures, but their reliability may be compromised. Because the models predict temperatures above boiling, the actual junction temperatures may be lower because of phase change effects. On the other hand, they may be higher because of local hot spots and bubble formation. The model does not account for the latent energy exchange associated with boiling and cannot prescribe junction temperatures if the boiling point is exceeded. Experimentation will have to validate the modeling results, which will give more information about the type of flow model that best describes the physical setup.

A comparison of the velocity profiles for the three different porous media models is in Figure 32. The profiles are plotted over the radius of the hole. The same trends are shown as compared to the annular flow channel. The Forchheimer correction profile is flatter than the parabolic Brinkman profile. In this case, the Forchheimer correction

Table 12. Maximum temperature results for the four-hole design

Maximum Temperatures	**Darcy**	**Brinkman**	**Brinkman with Forchheimer Correction**
T_{IGBT} °C	150.8	160	156
T_{diode} °C	152.9	160.4	156.9
T_{fluid} °C	127.7	139.7	134.3

flattens the profile by a greater percentage than in the annular design, which leads to a greater reduction in the maximum temperatures.

Porous Media Benefit

The porous media was added to spread the heat deeper into the working fluid. The plots of the outlet temperature distribution for the small circular duct and rectangular duct in Figure 13 and Figure 18 showed that a large core of fluid still existed at the inlet temperature. For comparison, Figure 33 and Figure 34 show the temperature distribution of the annular duct and four-hole duct pattern. These plots show that more of the fluid is heated. For the annular design, ~50% of the height of the annulus is warmer than the initial inlet temperature. For the four-hole design, the fluid is heated over half the radius on the hot side of the duct. In comparison, only 25% of the rectangular duct height and circular duct radius were heated in the free flow designs. Adding metal foam does aid the heat transfer from the ceramic substrate to the fluid.

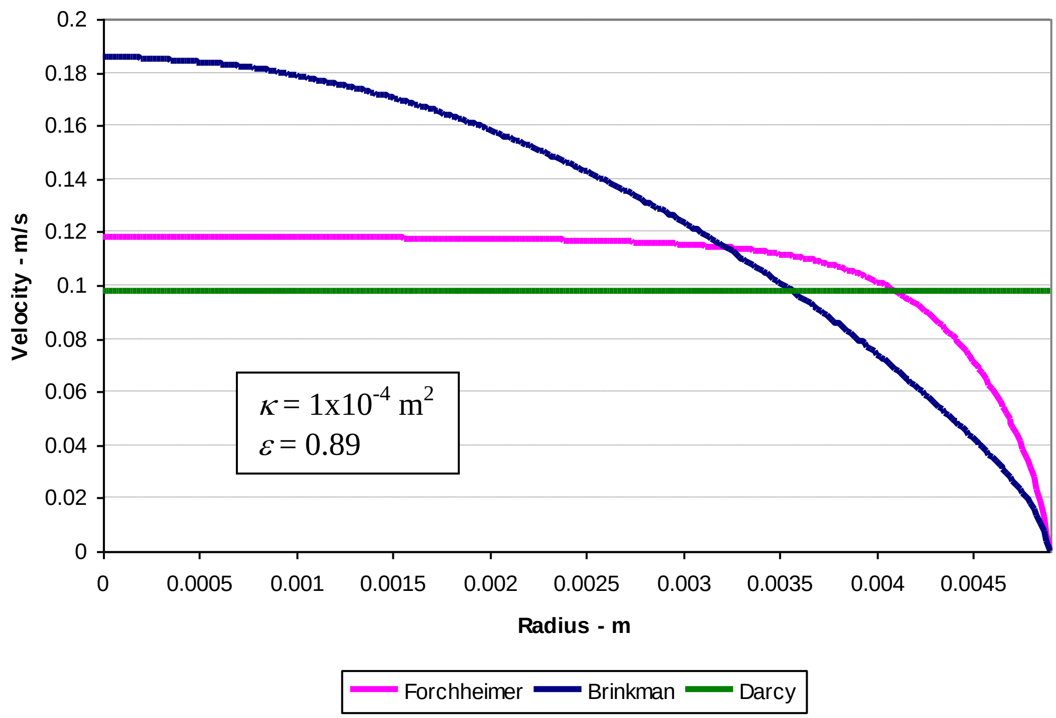

Figure 32. Comparison of velocity profiles for the four-hole design

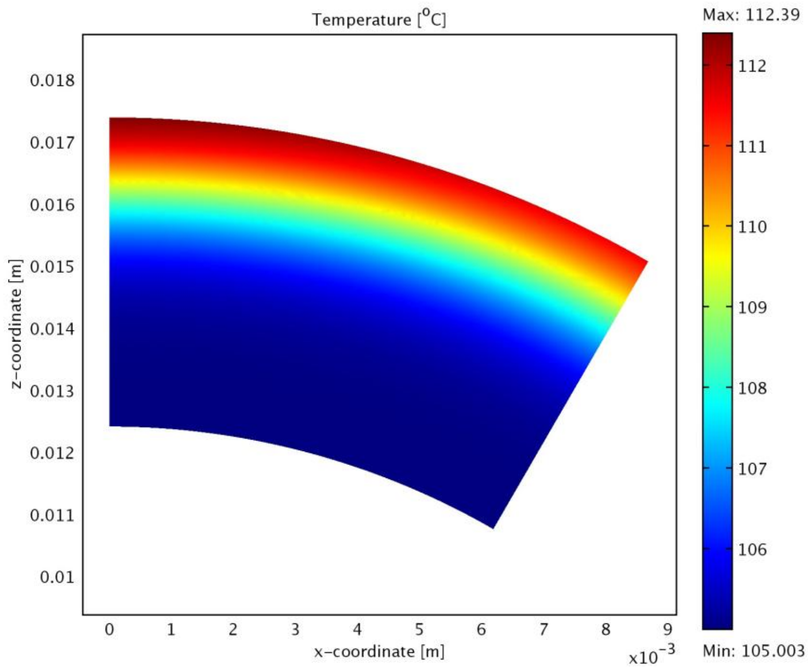

Figure 33. Outlet temperature distribution for the annular duct design with Brinkman-Forchheimer flow

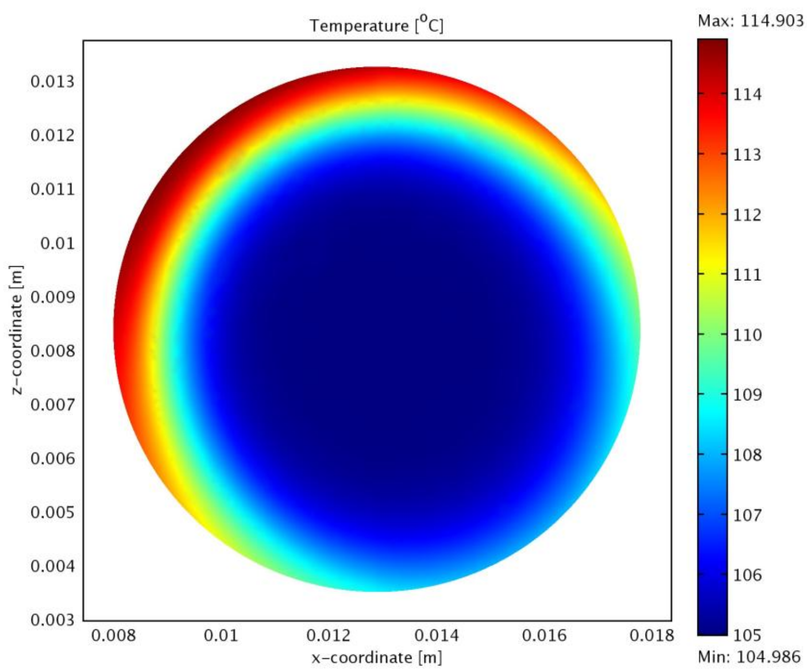

Figure 34. Outlet temperature distribution for four-hole duct pattern with Brinkman-Forchheimer flow

Chapter 5 – Experimental Verification of Model Parameters

All of the porous media models to date have been based on values of permeability and porosity found in literature. To validate the model setup, experimentation is required to determine effective foam properties, flow behavior, and temperature distribution. Two primary experiments were conducted. The first was to determine the trend of the pressure drop across the foam with varying inlet velocity. This data was used to extract effective foam properties and flow parameters. The second experimental setup recorded temperatures at the wirebond flat and chip case to determine the accuracy of the predicted temperature distribution and solid material properties.

Permeability Measurement – Pressure Drop Experiment

To characterize the pressure drop and thus flow regime, Darcy or Darcy-Forchheimer, across foam pieces, the permeability of the metal foam must be determined. Typically to measure permeability, a long section of metal foam is sandwiched between two plates or is inserted in a long tube, and pressure taps are placed within the boundaries of the foam piece. The pressure drop is recorded for various flow rates and analyzed to determine the flow behavior [40, 47, 48].

Apparatus

In the present application, a long test section was not feasible, and a modified experimental method had to be devised. The ceramic substrate contains a relatively short section of foam, and pressure taps are only available up and down stream of the whole substrate. A schematic of the test set up is in Figure 35. A Bay Voltex unit, a custom commercial heater/chiller, circulates the 50/50 water ethylene glycol (WEG). This unit is capable of regulating the temperature of the working fluid from 0ºC to 110ºC and providing flow from 0.25 to 2.5 GPM at various discharge pressures [49]. An auxiliary heater was installed on the outside of the Bay Voltex unit to assist the internal heating element when running at elevated temperatures.

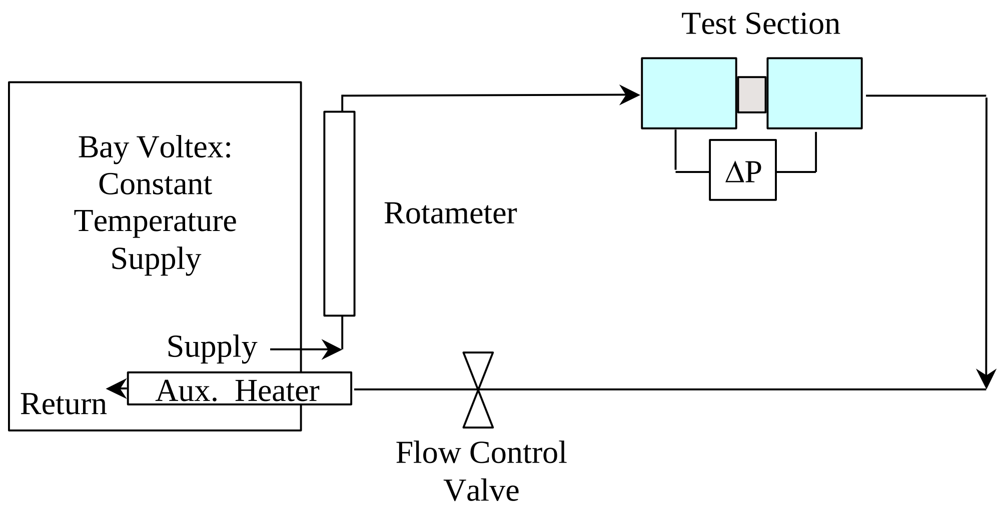

Figure 35. Schematic of component test experiment

The auxiliary heater allows for the temperature to regulate faster than if left to only the internal heat source.

The volumetric flow was measured by a rotameter, which had been calibrated for 50/50 WEG. The calibration procedure and results are in the Appendix. The pressure drop was measured by both a differential pressure gage and two pressure gages (relative to ambient) to evaluate the accuracy of the data reduction. The temperature was monitored with a thermistor in the test section header. Device specifications are in the Appendix.

A schematic of the test section is in Figure 36. A pressure gage was placed on each header in a side port. These gages can operate up to 125ºC, but the output has to be compensated for operating temperatures above 85ºC for accurate results [50]. The differential pressure gage was fed from taps on the bottom of the header. The differential meter had bleed valves built into it to make sure no vapor was in the lines leading to the differential transducer. The transducer housing had to be kept below 65ºC to operate within the compensated temperature range [51]. The transducer temperature was monitored and never exceeded 35ºC with 100ºC WEG at the test section.

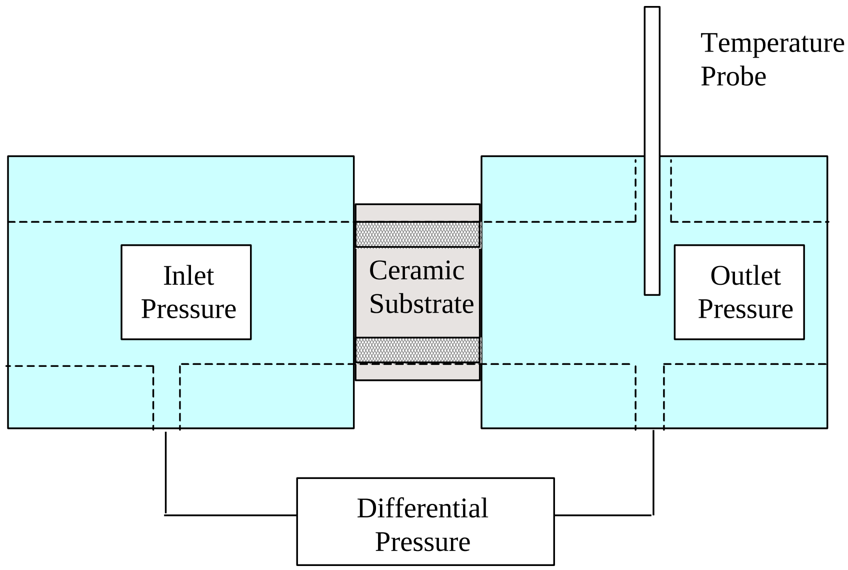

Figure 36. Schematic of test fixture for pressure drop measurements

The temperature of the working fluid was monitored downstream of the ceramic substrate so that the thermistor probe did not create a flow disturbance at the header inlet. For flow characterization testing, the placement of the temperature probe is not crucial because all that needs to be maintained is an isothermal working fluid. For the thermal validation experiment, more temperature-measurement probes were added to account for energy transfer.

Test Procedure

The pressure drop across the ceramic substrate was measured at WEG temperatures of 25ºC and 100ºC. A baseline measurement at 25ºC allows for the data reduction method to be evaluated without the added difficulty of operating outside the compensated temperature range of the transducers. During the test runs, the flow was controlled by a needle valve on the return side of the experiment as shown in Figure 35. This allows for the working fluid to be pressurized at the test section. Gage pressure between 16 and 20 psig (110.3 and 137.9 kPa) were needed for the heat transfer testing to insure that the boiling point of WEG was not exceeded.

A pressure regulator on the Bay Voltex unit was also used to regulate flow and maintain a constant pressure inlet on the experimental test section. The inlet pressure was maintained constant for comparable data collection runs. A constant inlet pressure was critical to collecting good data. The flow through the foam is pressure driven, and the pressure drop varies with the inlet pressure at comparable rotameter readings. If the pressure regulator was not adjusted, the inlet pressure could vary 50% over the range of the measured flow rates.

Data was collected for at least 100 seconds at rotameter readings from 95% to 10% in steps of 5% or until the limits of the pump output were reached. After the last reading, the pump was shutdown, and a bias measurement was recorded at no flow. The temperature set point had to be adjusted slightly, s.p.+0.5 to 1.5ºC, at lower velocities to maintain 100ºC at the test section.

The decrease in WEG temperature is expected because of the heat loss to the environment between the supply and the experimental test section. The heat loss from the experimental system would consist of radiation and convection from an isothermal source to the ambient, which would be constant assuming no major changes in the ambient conditions over the entire duration of the test. The energy balance requires that the heat gain by the environment be balanced by the heat loss from the WEG, which is given by:

$$q = \dot{m} c_p \Delta T \tag{25}$$

where q is the total heat loss (W), $\dot{m}$ is the mass flow (kg/s), c_p is the specific heat (J/kg/K), and ΔT is the temperature change (K) of the WEG between the set point and the experiment. As mass flow decreased, the change in temperature must increase to maintain a constant heat loss to the surroundings.

The pressure drop that can be measured is a total pressure drop across the ceramic substrate, which consists of viscous components and two sources of form drag. The form drag results from the ceramic substrate shape and the porous media at higher inlet velocities. In order to account for the form drag of the ceramic substrate, the pressure drop was recorded for a test section with foam and without foam. For the annular shape, a dummy core was held in place by a thin structure that was pinched between the ceramic and the flow header. For the four-hole design, a substrate with no foam inserts was used. The orientation of the four-holes was held consistent between runs with foam and no foam.

This procedure was followed for eight data collection runs: the annular ceramic substrate with aluminum foam at 25ºC and 100ºC, the annular ceramic substrate with a dummy core at 25ºC and 100ºC, the four-hole design with aluminum foam at 25ºC and 100ºC, and the four-hole design with no foam at 25ºC and 100ºC.

Results and Discussion

For all cases, the pressure drop was first corrected by a measured offset at no flow. For comparable runs, the offset was fairly constant. Next, the pressure drop measured for no foam was fit to a regression due to the scatter in the data set. The data from the differential transducer had much less scatter than that derived from the two relative gages. This result is expected based on the range of the respective devices. Also the regression allows for the data to be subtracted from other data sets where exact matches in flow rate may not exist. Finally, the pressure drop regression for the no foam run was subtracted from the data with aluminum foam to yield the pressure drop across the foam section alone. The reduced data for both duct designs is in the Appendix. This data can be used to calculate the applicable permeability and the Forchheimer form drag coefficient for each case. The permeability calculated from the in-situ measurement in this manner represents the effective permeability. It includes the effect of increased porosity near the walls and the finite length of the porous section.

Annulus

Figure 37 shows the reduced data for the differential pressure gage. The data follows a logical trend which is representative of flow through porous media that is governed by Darcy-Forchheimer flow:

$$p_{in} - p_{out} = \left(\frac{\mu}{\kappa} + \frac{\rho C_f |u|}{\sqrt{\kappa}} \right) u \Delta x . \tag{26}$$

A second order polynomial was fit to the data points from the differential pressure gage with the y-intercept specified at 0 Pa; the correlation coefficient was R=0.995.

Using the linear coefficient from the best fit quadratic polynomial and known fluid properties evaluated at test section temperature, permeability, κ (m^2), was calculated by comparison to the linear term in Eq. (26). The linear term represents the Darcy contribution to the pressure gradient. Likewise, the quadratic coefficient is used to find the Forchheimer form drag coefficient, C_f. The calculated foam properties for WEG at 25°C are $\kappa = 9.64 \times 10^{-8}$ m^2 and $C_f = 0.072$. Using these values, the pressure drop for the Darcy-Forchheimer model is calculated using Eq. (26). Figure 37 shows the Darcy-Forchheimer model in red, which overlays the second order least-squares regression.

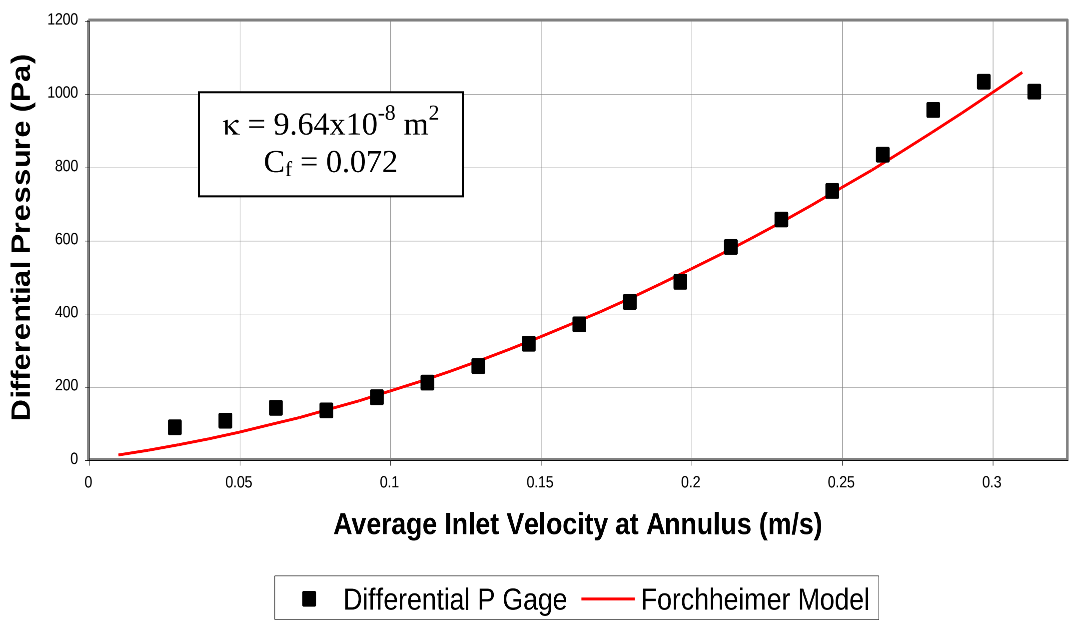

Figure 37. Pressure drop across aluminum foam annulus at 25ºC

Table 13. Properties of 10 PPI foam from previous literature

ε	Foam Material	κ (m^2)	C_f	Reference
0.914	Al	$1.01\text{x}10^{-7}$	0.054	[40]
0.794	Al	$2.20\text{x}10^{-8}$	0.098	[40]
0.918	Al	$6.23\text{x}10^{-7}$	0.182	[40]
0.878	Ceramic	$1.93\text{x}10^{-7}$	0.048	[40]
0.9486	Al	$1.2\text{x}10^{-7}$	0.097	[47]
0.9138	Al	$1.1\text{x}10^{-7}$	0.07	[47]
0.8991	Al	$9.4\text{x}10^{-8}$	0.068	[47]
0.949	Al	$1.49\text{x}10^{-7}$	0.099	[47]
0.909	Al	$1.11\text{x}10^{-7}$	0.082	[47]
0.91	Al	$4.21\text{x}10^{-8}$	0.0076	[52]

Table 13 contains other values of permeability and Forchheimer drag coefficients found in other studies. The selected values are all from foams designated as 10 PPI. Also they have porosity values (ε) within a reasonable range of those measured for the aluminum foam samples in the present study. The values from the current experiment lay well within the results of other studies.

For the 100°C case, the permeability and Forchheimer drag coefficient obtained at 25°C and the WEG properties at 100°C were used to calculate the predicted pressure drop from Eq. (26). The resulting Forchheimer pressure drop prediction is the red line shown in Figure 38 for the annular channel. The same data collection and reduction procedures were followed at 100ºC for the annular foam channel. The reduced data for the differential pressure gage is shown in Figure 38 with error bars defining a 95% confidence band in the reduced data. The uncertainty analysis procedure is detailed in the Appendix.

The Darcy-Forchheimer model based on the foam properties obtained at 25°C lies within the error bars on the lower and upper end of the measured flow region. Only small deviation from the confidence band is noted in the center area. In the actual operating region, to the left of the blue vertical line, the model well describes the pressure drop expected for the aluminum foam annulus.

Also noted in Figure 38 is the maximum allowable operational point for the channel. Figure 38 shows why more data had to be collected above the operational point to determine flow behavior. At higher average inlet velocities, the Forchheimer model is more sensitive to the drag coefficient than at lower flow velocities. If data had only been collected up to the maximum operation point, the quadratic component of the pressure gradient would have been hard to determine.

Another means of qualifying the reasonableness of the flow parameters is to examine them on a nondimensional scale in terms of a porous media Reynolds number and friction factor. The respective nondimensional groups are given by Eq. (27) and Eq. (28), where ρ is the density (kg/m^3), u is the local average velocity (m/s), κ is the permeability (m^2), μ is the dynamic viscosity (Pa·s), and ∇p is the pressure gradient

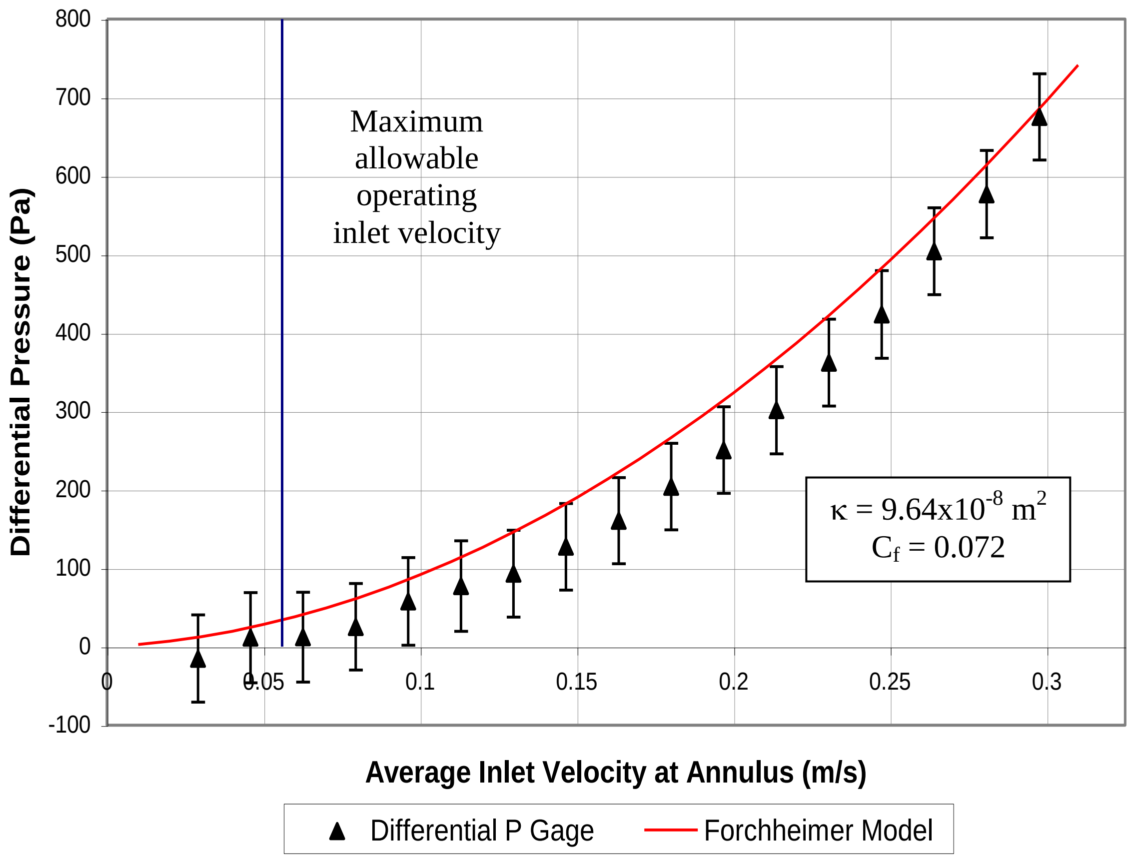

Figure 38. Pressure drop across aluminum foam annulus at 100ºC where $\kappa = 9.64 \times 10^{-8}$ m^2 and $C_f = 0.072$

(Pa/m). The porous media Reynolds number is defined here as the ratio of the form drag from the Forchheimer correction to the viscous drag from the Darcy contribution

$$\mathrm{Re}_{pm} = \frac{Form\,Drag}{Viscous\,Drag} = \frac{\rho u C_f \sqrt{\kappa}}{\mu}, \tag{27}$$

$$f_\kappa = \frac{-\nabla p \sqrt{\kappa}}{\rho u^2}. \tag{28}$$

If the Darcy-Forchheimer model is used to express the pressure gradient, the friction factor reduces to:

$$f_{\kappa_{D-F}} = -\frac{\sqrt{\kappa}}{\rho u^2}\left(-\frac{\mu}{\kappa} - \frac{\rho C_f |u|}{\sqrt{\kappa}}\right)u = \frac{\mu C_f}{\rho u \sqrt{\kappa}} + C_f = \frac{C_f}{\mathrm{Re}_{pm}} + C_f. \tag{29}$$

If the Darcy model is used to express the pressure gradient, then the friction factor reduces to:

$$f_{\kappa_D} = -\frac{\sqrt{\kappa}}{\rho u^2}\left(-\frac{\mu}{\kappa}\right)u = \frac{\mu}{\rho u \sqrt{\kappa}} = \frac{C_f}{\mathrm{Re}_{pm}}. \tag{30}$$

These two expressions for friction factor, Eqs. (29) and (30), are shown in Figure 39 as solid lines. Ideally the experimental data evaluated in Eqs. (27) and (28) would fall within these two bounds.

For the most part, the data does fall within these ranges. At low Re_{pm}, the data stray from the model. This variation is attributed to forcing the least squares regression through y = 0 Pa. From the ideal models (solid lines) in Figure 39, it is evident that the Forchheimer term begins to significantly contribute to the friction factor between Re_{pm} = 0.1 to 1. After Re_{pm} = 1, the Forchheimer term dominates the Darcy contribution to friction factor as it becomes asymptotic to C_f. For the data at 25 ºC, the higher velocities, i.e. $\mathrm{Re}_{pm} > 1$, are adhering to the Forchheimer model. The result is not surprising because this data was the source for the least squares fit which determined κ and C_f. Flow in the region of Re_{pm} = 0.1 to 0.5 is behaving more like Darcy flow with the deviation from the ideal case attributed to error in data reduction and instrumentation.

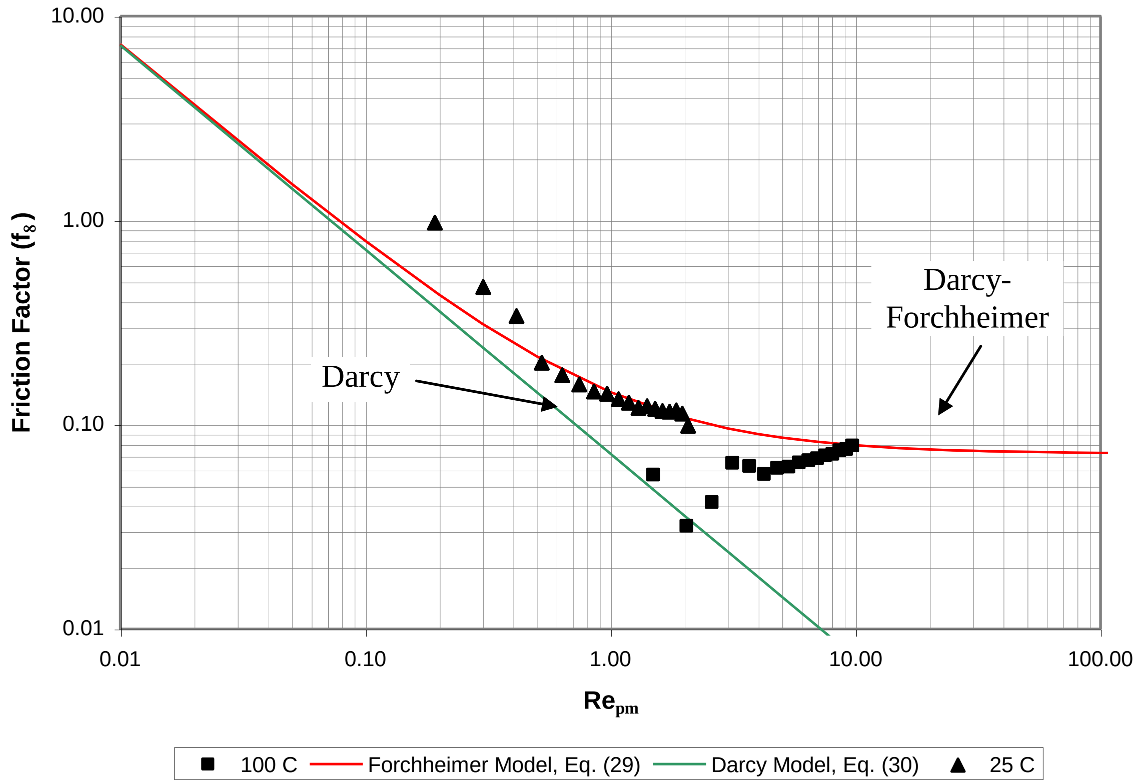

Figure 39. Friction factor for aluminum foam annulus where $\kappa = 9.64\text{x}10^{-8}$ m^2 and $C_f = 0.072$

The data at 100ºC displays similar effects but is not as clear in the interpretation. The data almost appears to undergo a transition from Darcy-like flow to Darcy-Forchheimer flow between Re_{pm} = 1 to 5. Considering the actual operation range of the system is between Re_{pm} = 2 to 3, the dominant flow mechanism should be Darcy-Forchheimer flow based on the theoretical models. However, the data lie closer to the Darcy flow regime. Determining the correct flow model for this flow condition is not obvious from the pressure drop data. The thermal validation data should give more information to determine which flow regime and model yields better results.

Four-hole

The same data reduction process was followed for the four-hole design at 25ºC. The results are shown in Figure 40. Using the data from the differential pressure gage for the four-hole design in Figure 40, the quadratic least-squares regression had a correlation coefficient of R = 0.9996. The calculated flow properties were $\kappa = 6.54 \times 10^{-8}$ m^2 and C_f = 0.056. Again, these values fall within a reasonable range when compared to the values in Table 13.

Again, the foam properties obtained at 25°C were used in conjunction with the coolant properties at 100°C in Eq. (26) to form the Darcy-Forchheimer model at 100ºC. The red line in Figure 41 is the Darcy-Forchheimer model evaluated with fluid properties at 100ºC and flow parameters found from the 25ºC data. The black triangles are the data from the differential pressure gage measured at 100ºC and a 95% confidence band is shown for the data.

Overall, the Darcy-Forchheimer model lies within or near the 95% confidence band of the data. More deviation is noted in the mid-range of velocities, but the model is well within the confidence band at the operating inlet velocity that is noted by the vertical blue line. Using these flow parameters should give more realistic results in the thermal performance models.

The friction factor results for the four-hole design in Figure 42 are similar to the annulus friction factor results. The 25°C data falls close the Forchheimer model because they form the basis for the measured foam properties. It appears that the flow transitions

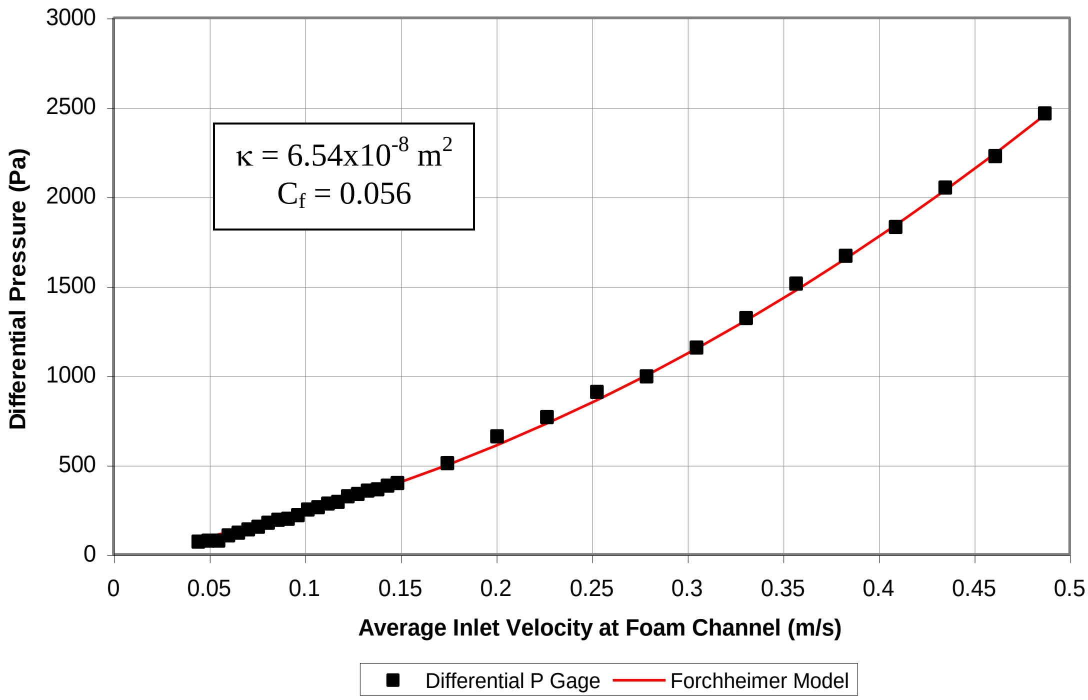

Figure 40. Pressure drop across aluminum foam in four-hole design at 25ºC

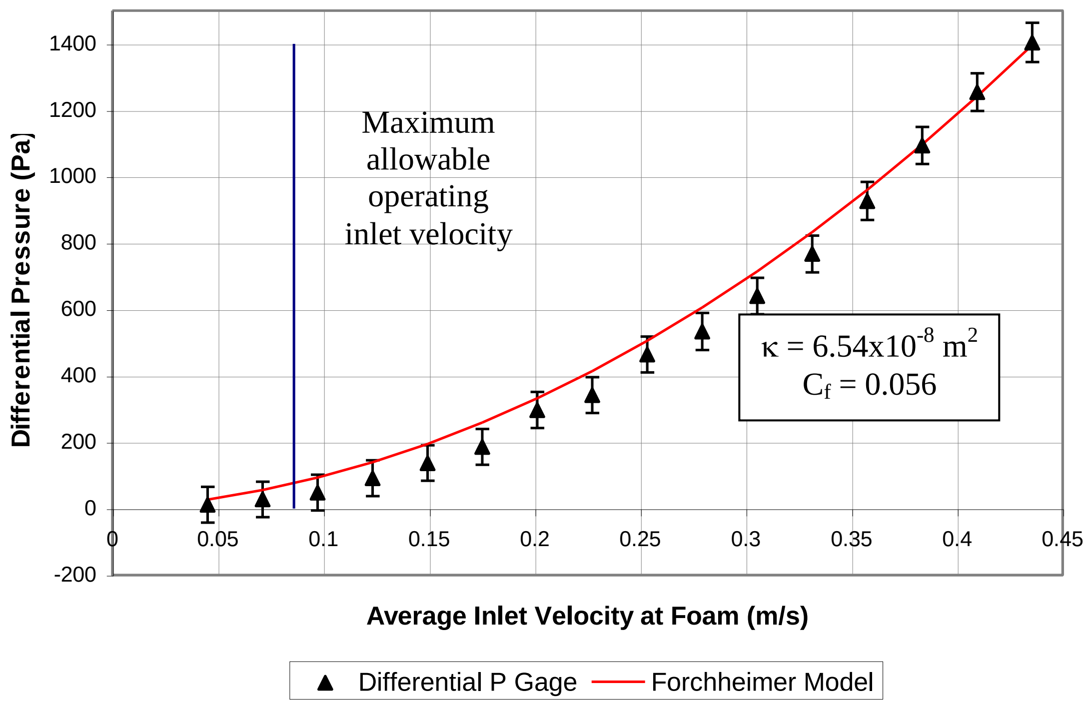

Figure 41. Pressure drop across aluminum foam in four-hole design at 100ºC where $\kappa = 6.54\text{x}10^{-8}$ m^2 and $C_f = 0.056$

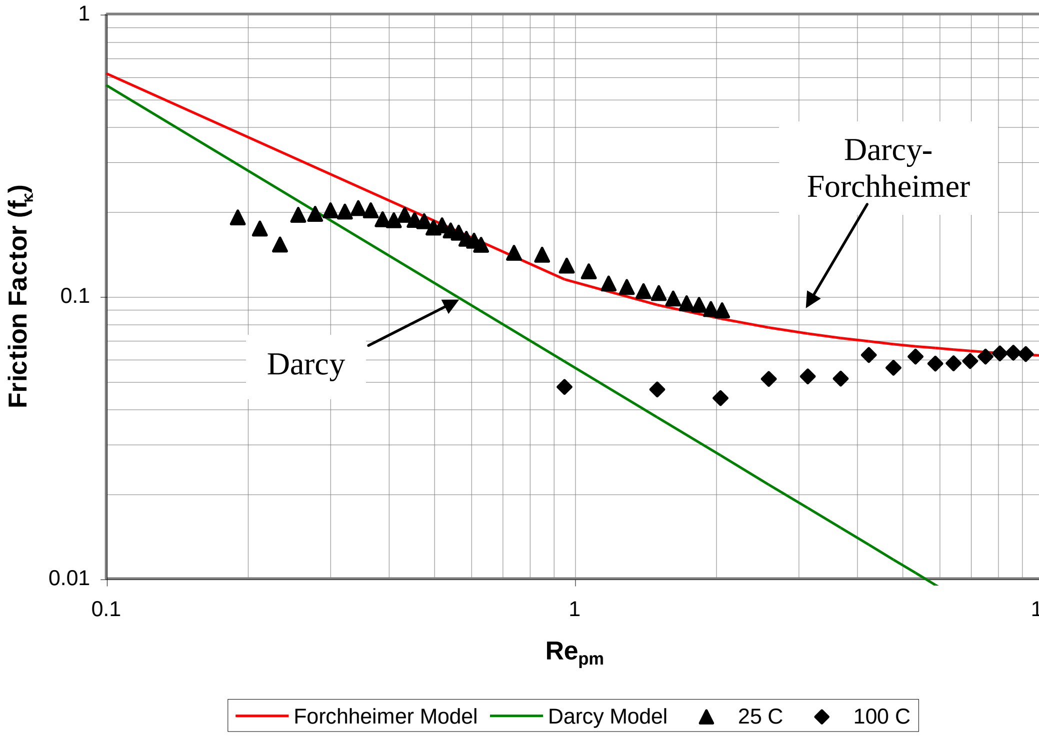

Figure 42. Friction factor for aluminum foam in four-hole design where $\kappa = 6.54 \times 10^{-8}$ m^2 and $C_f = 0.056$

from Darcy flow between $Re_{pm} = 0.2$ and 0.5. The 100°C data looks as if it is undergoing a transition from Darcy to Forchheimer flow from $Re_{pm} = 1$ to 5. This trend is hard to interpret because nondimensionalizing the data should account for temperature effects.

The actual operating condition at 105°C would lie near $Re_{pm} = 2$. From the theoretical models, this point should be well within the Forchheimer flow domain. According to the 100°C data, this operational point may just be starting to transition from a Darcy dominated flow. The thermal experimentation should be helpful in identifying which flow model produces temperature predictions that are more agreeable to the actual results.

From the pressure drop experimental data, the models derived for the aluminum foam annulus and the aluminum foam cylinders are in general agreement with general Darcy-Forchheimer behavior at higher velocities. Deviation from the predicted behavior at low flow rates may be explained by data reduction error; however, the thermal validation experiment should help show which model, Darcy or Darcy Forchheimer, results in closer thermal predictions at a low flow rate.

Addendum

In light of the inconclusive evidence in the friction factor plots, another data reduction method was used to determine permeability and Forchheimer drag coefficients. One assumption used in the initial data reduction process was that the flow parameters κ and C_f were constant with temperature. The permeability is a geometric property of the foam and does not vary with fluid temperature [28]. This fact can be observed from Darcy's Law. Dividing the temperature dependent viscosity out of Darcy's Law shows that the adjusted pressure gradient is directly proportional to velocity by a factor of $1/\kappa$

$$-\frac{\nabla p}{\mu} = \frac{u}{\kappa}. \tag{31}$$

However, when the Darcy-Forchheimer model is used to model the entire pressure drop over the flow range, the drag coefficient is temperature dependent. Dividing viscosity out of the expression shows that the Forchheimer term still has temperature dependent variables of density and viscosity

$$-\frac{\nabla p}{\mu} = \frac{u}{\kappa} + \frac{\rho C_f u^2}{\mu\sqrt{\kappa}}. \qquad (32)$$

Thus it cannot be expected that using constant flow parameters would yield a good fit for the data obtained at different fluid temperatures.

The new data reduction method identifies a linear operating region of the data at low flow where the pressure drop at both temperatures is similar. This data is used to extract permeability for the respective duct geometry. Then, the Forchheimer drag coefficient is determined by manually adjusting the model to the data set. In this process, the data was also shifted to account for linear offsets between y-intercepts. The results lead to new flow parameters, which are shown in Table 14. More discussion of the new data reduction procedure and results are detailed in the Appendix A.6.

For future work, these parameters should be used in the thermal models. The thermal models in the following validation section, however, use the flow parameters originally established in the first data reduction method as in Figure 39 - Figure 42.

Thermal Performance Verification

To verify the model subdomain and boundary conditions, thermal tests were conducted. The original plan was to use diodes as heat sources to test the thermal performance. Due to manufacturing delays in the modules, this setup was not feasible. Therefore, an alternative experimental setup was developed.

Table 14. Flow parameters from new data reduction technique

	Permeability, κ (m^2)	Forchheimer Drag Coefficient, C_f
Annulus, 25ºC	7.97×10^{-8}	0.060
Annulus, 100ºC	7.97×10^{-8}	0.062
Four-Hole, 25ºC	3.22×10^{-8}	0.021
Four-Hole, 100ºC	3.22×10^{-8}	0.036

The ceramic hexagons that were available for testing had 200 to 400 microns (0.008-0.015") of copper directly bonded to the outer flats. The original request for the copper thickness was for over 1 mm of copper. The adverse impact of the much thinner copper would primarily be on the heat spreading. Nevertheless, modeling verification tests could be conducted with these hexagons. However, the models were adjusted for the reduced copper thickness.

Apparatus

Because the copper-clad substrates were not available in time to attach diodes for this study, it was decided to use surface mounted resistors instead. A fixture was built to clamp resistors to the chip mounting surface to act as heaters as shown in Figure 43 and Figure 44. The 60 W, 1 ohm resistors were packaged in clip style TO-220 cases [53]. A thin layer of thermal grease was applied under the resistors to fill voids. The resistors then were wired in series to produce a heat load to the module. Garolite blocks (k=0.288 W/m·K [54]) were used between the resistor case and the clamping screw to add some insulation and spread the force over the entire resistor case.

Thermocouples and voltage leads were also attached to the unit to monitor resistor case temperature, wirebond flat temperature, and the voltage drop across each resistor. The case temperature thermocouple was inserted between the Garolite block and the top side of the resistor case. This temperature was monitored to prevent over heating the resistors while conducting the experiment. The wirebond flat temperature was monitored as the primary validation temperature for comparison with the models. This location provided the least temperature gradient in the computer simulations and hence is less sensitive to the attachment location. Also this location accounts for dimensional effects of heat travel through the alumina substrate and to the fluid/foam matrix. The voltage drop was monitored to ensure equal power distribution/heat loss from each resistor. An unbalanced heat load would make comparisons to a model more difficult because of the assumed symmetry planes in the computer simulations.

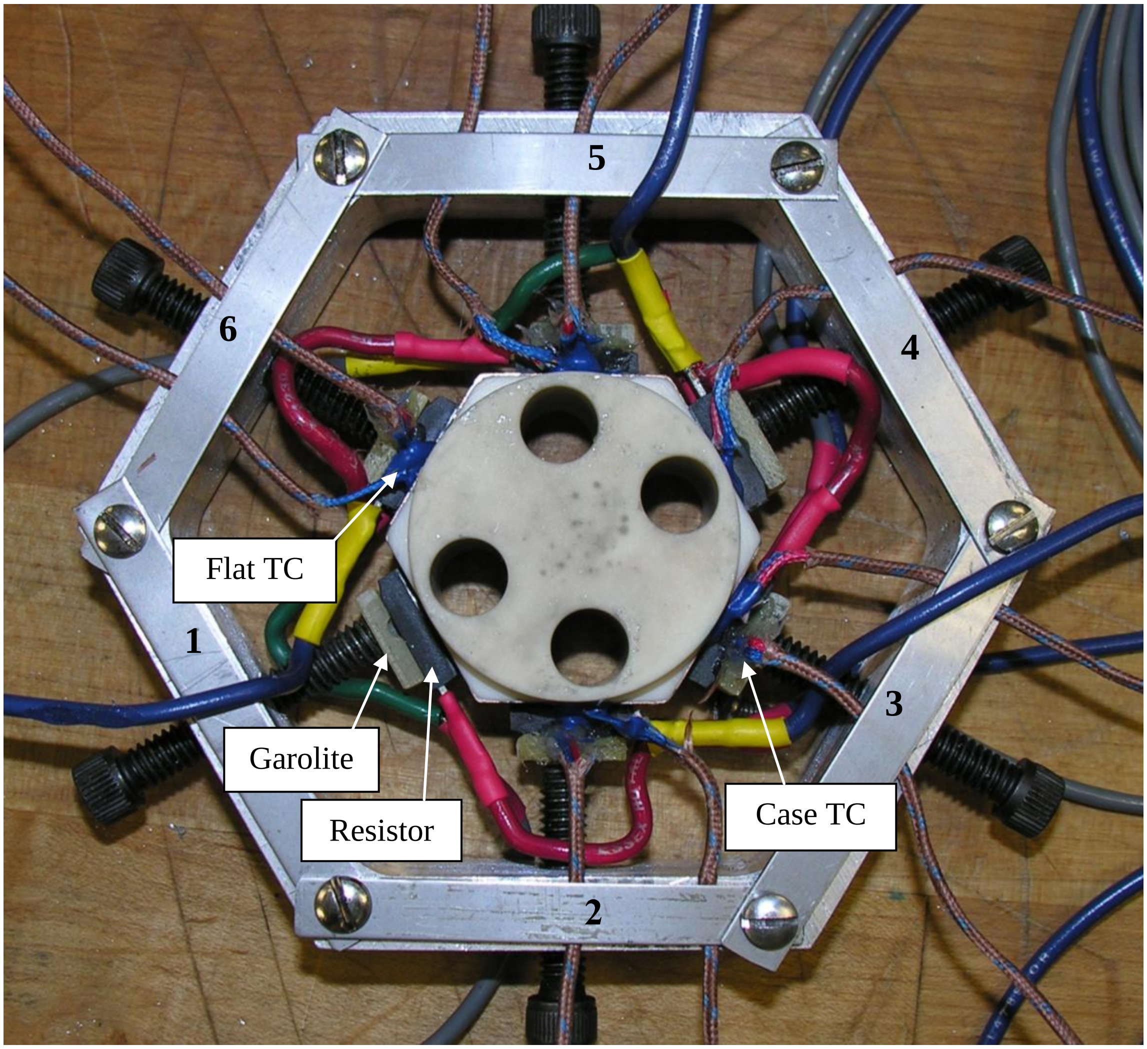

Figure 43. Four-hole substrate in the experimental clamp fixture

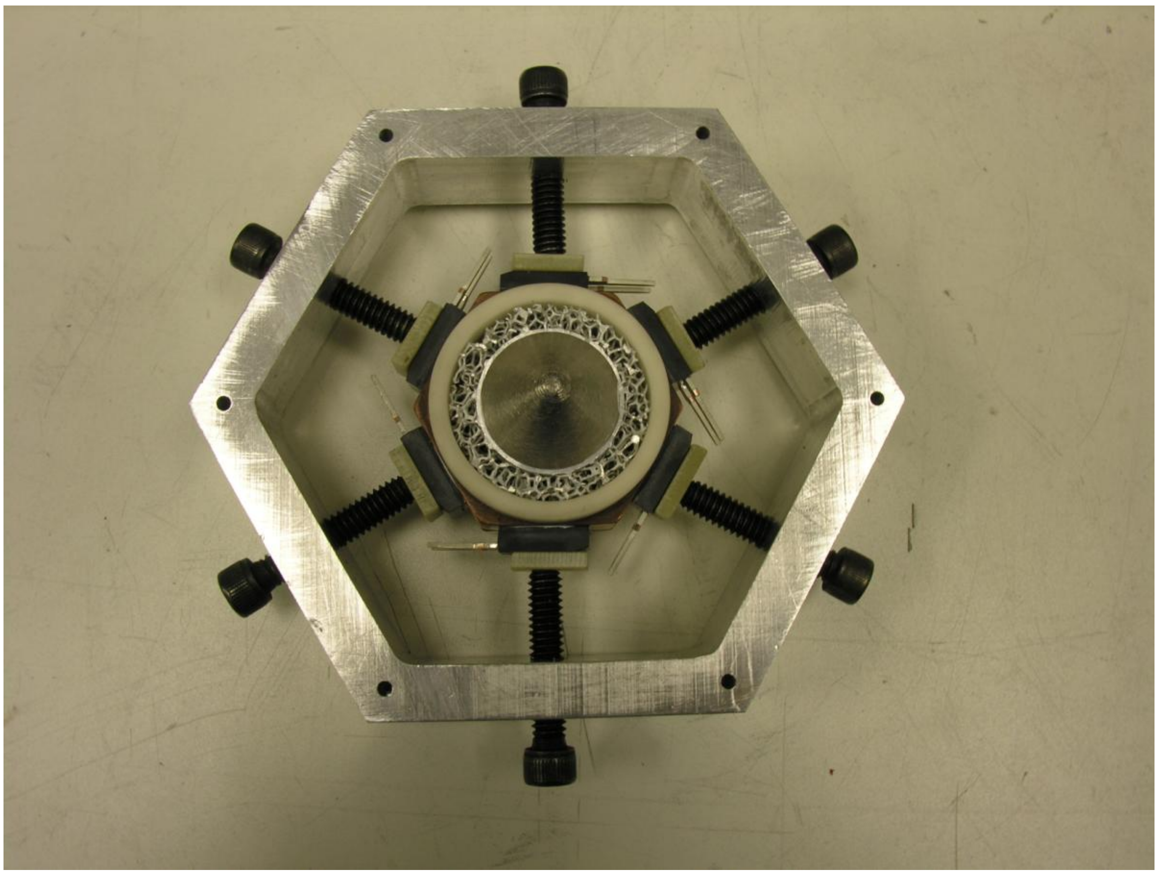

Figure 44. Annular structure in holding fixture prior to instrumentation

First, the four-hole substrate was tested. At the time of experimentation of this substrate, an insufficient number of thermocouples were available. The placement of these was judicious with careful consideration given to their relative location to device and to fluid hole location. Also noteworthy is the size of the thermocouples. All but the case temperature at location 1 was measured with 24 gauge thermocouples. Case #1 had a 20-gauge thermocouple (not shown).

Next, the annular substrate was tested, and improvements were made in the setup. Overall the annular substrate was installed in a similar manner, but a smaller gauge wire was used for the voltage measurement leads. The small diameter reduces the amount of heat that the leads can carry away from the device. Also temperatures were measured on all cases and wirebond flats.

The clamping fixture was then inserted into the same headers that were used for the pressure drop experiments. The fluid inlet temperature was measured with a thermistor. The fluid outlet temperature was taken as the average of two thermistors placed in different radial locations with respect to the substrate. The inlet gage pressure was monitored with a transducer. In this setup, no added benefit is gained from the differential pressure transducer because the flow rate and inlet pressure are held constant for the entire experiment. Thus, the differential transducer was removed. The entire test section assembly was insulated as shown in Figure 45. Also shown in Figure 45 are the power supply, fluid connections, and data acquisition system. The equipment specifications are in the Appendix. It should also be pointed out that the system is placed on an incline to ensure that the fluid fills without any bubbles the flow channels in the ceramic substrate.

This alternate experimental design offers the following advantages over the setup that was originally planned:

- Heat load devices could easily be replaced if they failed or if heat generation was not the same for all resistors. Soldered or sintered devices would not be easily replaceable because of the attachment technique and required wirebonding.

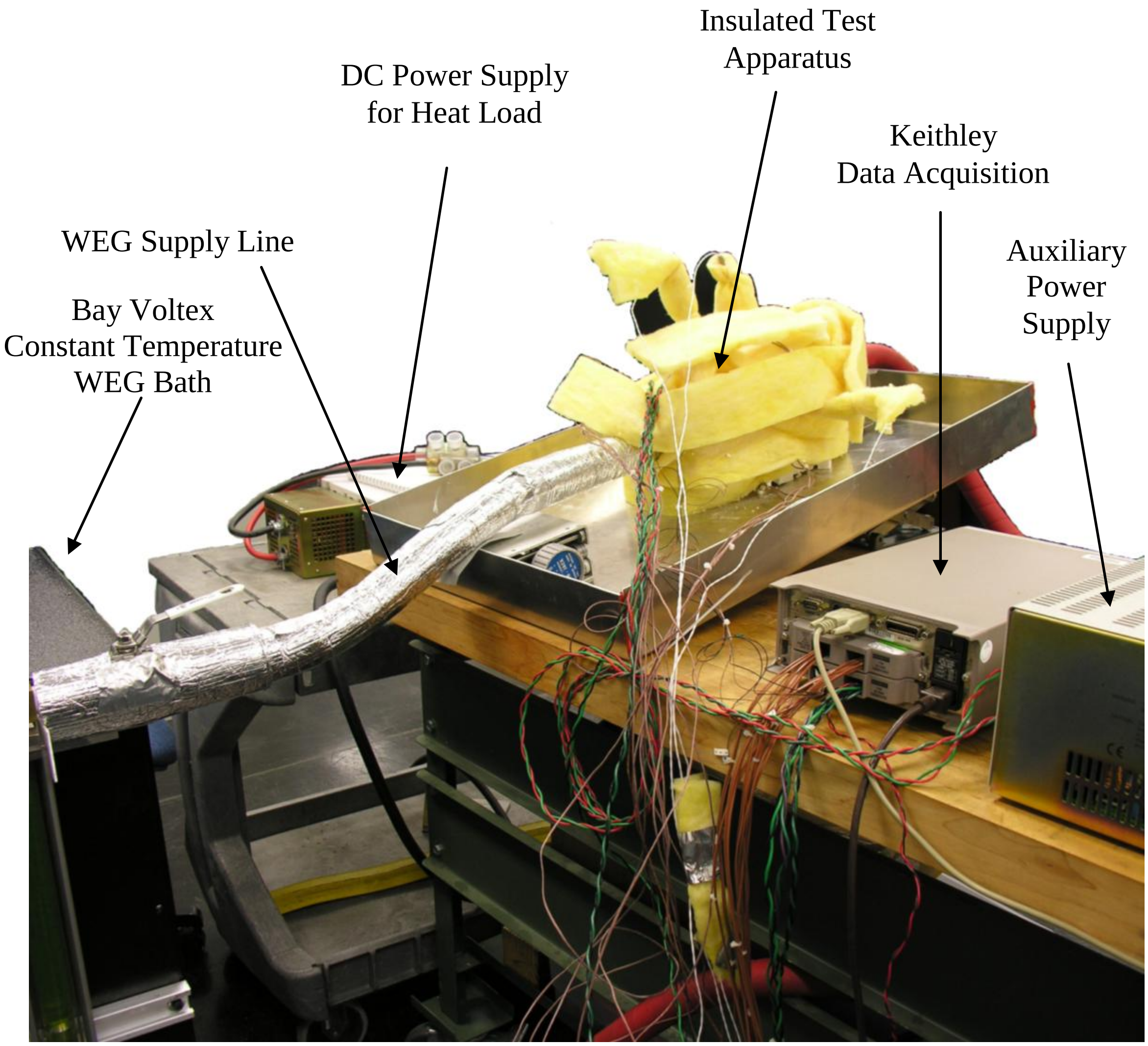

Figure 45. Photograph of the insulated test apparatus (see Appendix for device specifications)

- The fixture allowed for easy thermocouple placement and wire strain relief as shown in Figure 43.

The disadvantages of this setup were:

- Additional heat paths were created from the resistor to the ambient. Forcing heat to the fluid becomes more difficult.
- Electrical leads can conduct heat from the resistor to the ambient.
- The data reduction relies more heavily on the energy balance from the fluid side. Measuring bulk temperature at the outlet is difficult with limited number of probes.

Test Procedure

For each substrate, experiments were run over a range of inlet temperatures and power loads. Initially, the limiting factor was thought to be the resistor case temperature. The data sheet reported a junction-to-case thermal resistance of 2.08°C/W measured from the mounting surface of the resistor TO-220 clip mount package [53]. This surface was not available to instrument; thus, the outer case was used as the reference. The junction temperature was projected based on the power to the resistor and the documented junction-to-case thermal resistance; the projected junction was limited to 150°C.

It soon became evident that higher power operation would only be achievable with low temperature coolants (<75°C). At higher coolant temperatures, which are of most interest, insufficient heat was transferred to the fluid. After an initial set of data was collected, the resistors were run until the thermocouple at the case was 140 to 150°C or the power through the resistor was 55 W. The power limit keeps some safety factor imposed on the experiment. However, the assumption of a significant case-to-junction resistance was essentially ignored. Under this operational limit, much higher power levels were achievable at high coolant temperatures (90 – 105°C).

For subsequent runs with the four-hole and annular design, full power (55 W/resistor) was applied for coolant temperatures up to 90°C. At 105°C, the power was increased until the temperature limit on the case was reached. For each nominal inlet temperature, the pressure was maintained at 16 psi, and the rotameter was set to 18%.

This setting correlates to an average flow rate of 0.42 GPM, which is one-sixth of the maximum flow for the inverter.

Temperature Comparison

At each nominal inlet temperature, the entire experiment was allowed to come to a steady temperature with no power to the resistors. This operational point established a baseline from which to measure the temperature increase at each thermocouple location. At no power and low power, the average steady state temperatures were below the inlet temperature. Heat was lost from the fluid going out to the environment. A sample of the measured output is shown in Table 15. The reference run is the first row at no electrical power.

After power was applied, the experiment was allowed to come to a steady operational point before taking data. In the sample data, average steady state temperatures were measured at two different power levels. The experiment was then allowed to cool back to the baseline case, without power to the resistors, to confirm that the data baseline had not shifted during the experiment. The measured average temperatures were within 0.5% of the original reference case.

Because the measured fluid heat addition was initially negative, the total power assumed to be added to the fluid is adjusted from the baseline case. This value accounts for some of the system heat losses to the surroundings as compared to the measured electrical power. The adjusted heat addition rate was used in the heat generation term in the COMSOL models for comparison. Heat transfer is driven by temperature change. Therefore, to compare the computer simulation results with the experimental data, an appropriate temperature reference must be used. In this study, the most logical reference is the corresponding average temperature from the no power case. In the discussion to follow, the error reported is defined by:

$$\left(\frac{\Delta T_{COMSOL}}{\Delta T_{experimental}} - 1 \right) \cdot 100 , \tag{33}$$

$$\Delta T = \overline{T} - \overline{T}_{no\ power} . \tag{34}$$

Table 15. Sample data set for annular duct with an inlet temperature of 105°C

Measured Electrical Power (W)	Measured Heat Added (W)	Adjusted Heat Addition/ COMSOL Input (W)	Average Experimental Temperatures* (°C)		Average COMSOL Temperatures** (°C)		Model Error	
			Case	Flat	Case	Flat	Case	Flat
0.0	-80.0	0.0	94.8	98.2	105.0	105.0		
180.3	79.9	159.9	130.8	114.7	128.8	116.4	-34.0%	-30.9%
210.4	106.5	186.5	137.7	117.7	132.7	118.3	-35.5%	-31.7%
0.0	-77.2	2.8	95.3	98.6	105.0	105.0		

* Average of readings from all six thermocouples on respective surfaces (see Figure 43 and Figure 44 for example).

** Integrated average over the case and flat areas in the model.

Results and Discussion

When the projected junction temperature was used as the operational limit, insufficient heat was being transferred to the fluid. When the measured case temperature was used as the operation limit, much higher power levels were achieved and more heat was transferred to the 50/50 WEG. In addition, no failures occurred in the resistors. Given the power levels and case temperature, the resistors were operating well beyond their documented parameters.

Annulus

A sample output of FEA model for the annular structure is shown in Figure 46. This model is a one-twelfth symmetric section of the hexagon. The copper layer thickness reflects the average of the measured thicknesses on the actual substrate. The heat is applied as a boundary condition on the area of the footprint equal to the resistor size. The applied heat load is equivalent to the adjusted heat load measured on the fluid side of the experimental system. The flow parameters in the model reflect those determined from the pressure drop experiment, and the Brinkman-Forchheimer formulation was used for the flow field. Other material properties are held consistent with those established in Chapter 2. The inlet is specified at the appropriate temperature for run comparison. The outlet is set to convective flux, which allows for the energy in the flow to "escape" the model. All other boundaries are specified as insulated.

From this model, the average temperature was found on the resistor footprint. This location will be referred to as "Case". The average temperature was also found on the wirebond landing; hereafter known as "Flat". The steady state temperature from the no power case was then subtracted from the average temperature resulting in the total temperature rise for a given set of parameters. These temperature rises were then compared to the temperature rise measured from the experiment. As referred to earlier, the temperature rise in the experiment was calculated from the baseline case.

Figure 47 shows the deviation in the experimentation and the simulations as a percentage of the experimental results. The negative sign indicates that the COMSOL model results were below those measured. A comparison of the measured values

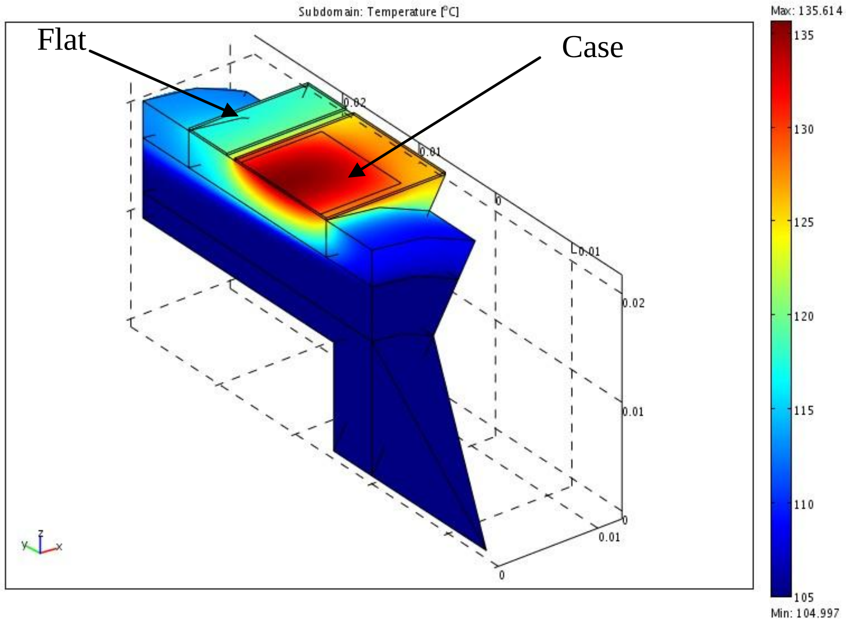

Figure 46. FEA output for annular structure at 105°C inlet

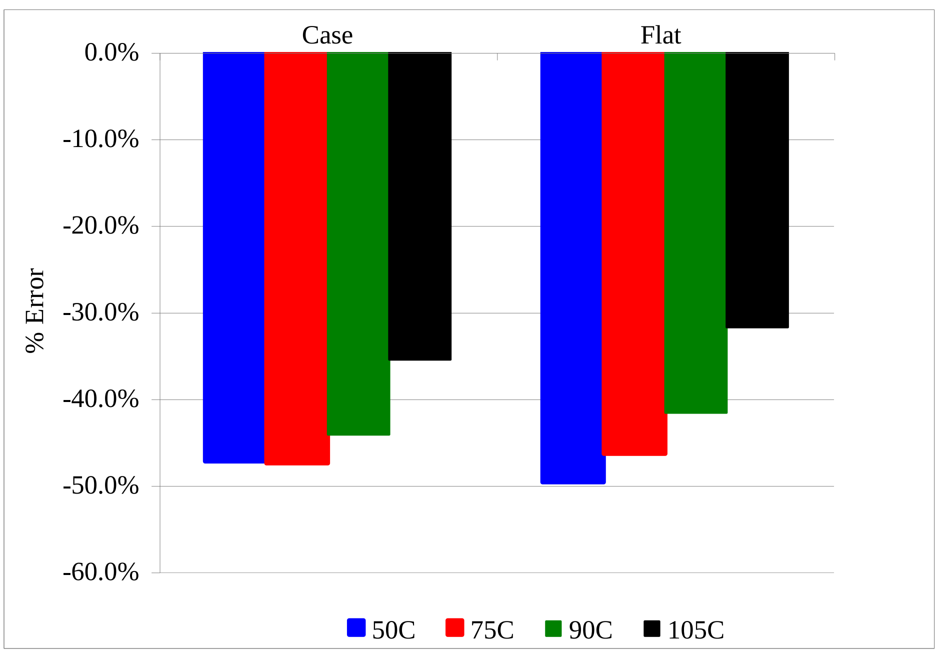

Figure 47. Temperature rise error between COMSOL and experiment for the annular structure

is also shown in Table 16. The absolute temperatures measured from the experiment are in the Appendix. The most significant conclusions in Table 16 are drawn from the "Flat" results. The case temperatures do not account for any contact resistance between the resistor and copper. The contact resistance can be a large contributor to the higher measured "Case" temperatures.

As inlet temperature increases, the error in the computer model decreases. This trend is thought to be physically related to the contact between the foam and the alumina substrate. The coefficient of thermal expansion for aluminum is three times greater than that of alumina. As the temperature increases, the foam will grow into the outer walls and provide more contact pressure, which will decrease the thermal resistance between the foam and substrate. Since the COMSOL model does not simulate an explicit contact resistance, the results would improve as the real contact resistance is decreased. Initially, this trend was also contributed to material properties, which were held constant for all models but had originally been evaluated near 105°C. A few models were run with variable fluid/foam properties evaluated at the respective inlet temperature and showed only a few tenths of a degree Celsius change. No significant error can be contributed to the temperature dependency of material properties.

Although the relative trends betweens varying inlet temperatures make sense, the large underestimation of wirebond flat temperatures requires more investigation. From a modeling perspective, several sources for the discrepancy can be identified. First, the predicted temperatures could be lower because less heat is being prescribed to the boundary than is actually passing into the ceramic substrate. The heat used in the model is measured from the fluid energy balance. The inlet temperature is measured close to the channel inlet 4 to 5 diameters upstream of the inlet, which is believed acceptable. The outlet temperature is also measured 4 or 5 diameters downstream; however, this distance may not be far enough removed to yield a good bulk temperature value. Furthermore, the thermistors were in stainless steel sheaths, which are attached to the header. The sheath sinks some of the heat from the thermistor to the header and ultimately results in a lower fluid temperature reading.

Table 16. Comparison of experimental and simulation data for annular structure

				Brinkman-Forchheimer $k_{alumina}$ = 25 W/m·K k_{foam} = 7.2 W/m·K		Brinkman-Forchheimer $k_{alumina}$ = 15 W/m·K k_{foam} = 2 W/m·K		Brinkman $k_{alumina}$ = 25 W/m·K k_{foam} = 2.5 W/m·K	
Nominal Inlet Temperature (^oC)	Electrical Power (W)	Heat Transfered to Fluid (W)		Average Case Temperature (^oC)	Average Flat Temperature (^oC)	Average Case Temperature (^oC)	Average Flat Temperature (^oC)	Average Case Temperature (^oC)	Average Flat Temperature (^oC)
50	331.3	250	Experimental	71.3	36.2	71.3	36.2	71.3	36.2
			COMSOL	37.6	18.2	66.9	35.9	49.7	29.3
			Error	-47.2%	-49.7%	-6.1%	-0.7%	-30.3%	-18.9%
75	332.25	253.3	Experimental	72.1	34.1	72.1	34.1	72.1	34.1
			COMSOL	37.9	18.3	67.0	35.8	50.3	29.7
			Error	-47.4%	-46.3%	-7.1%	5.0%	-30.3%	-12.9%
90	294.9	238.8	Experimental	63.7	29.3	63.7	29.3	63.7	29.3
			COMSOL	35.6	17.1	62.9	33.4	47.4	28.0
			Error	-44.1%	-41.6%	-1.3%	14.0%	-25.6%	-4.4%
105	210.4	186.5	Experimental	42.9	19.5	42.9	19.5	42.9	19.5
			COMSOL	27.7	13.3	48.8	25.8	37.0	21.9
			Error	-35.5%	-31.7%	13.7%	32.4%	-13.8%	12.4%

Along the same line of thought, the thermocouples used to measure the flat and cased temperatures have a large enough diameter lead that could conduct heat away from the thermocouple bead. The axial lead conduction results in lower measured thermocouple junction temperatures than what actual may be present. On the other hand, the change in temperature between operational points is the value of interest. Less error may be present in this temperature change than in the absolute value of temperature.

Reinstrumenting the experiment with finer gauge temperature measurement devices for the case and flat areas should help the accuracy and confidence in the measured data. Also locating finer thermocouples further downstream in a well-insulated tube could reduce the amount of error that is being created by the fluid temperature measurement.

Beside instrumentation error, another error source could be from the prescribed properties of the materials. The foam/fluid matrix properties were determined from best estimates out of literature. Now that experimental data is available for the explicit shapes, thermal conductivities of the metal foam/fluid subdomain and alumina were adjusted to produce temperature predictions that result in lower error as defined in this work. In these adjustments, Brinkman-Forchheimer flow model is held consistent with the effective flow properties found from the pressure drop data.

By changing the model heat source to a temperature boundary as measured in the experiment and examining the results, it was obvious that the model removed too much heat via the fluid. The two thermal conductivities were adjusted until the bulk temperature rise and total power input in the model better matched that of the experimentation. These adjustments resulted in new thermal conductivities for the fluid/foam matrix of 2 W/m·K and for the ceramic of 15 W/m·K. For the foam/fluid matrix, this is a decrease of 72%. For the alumina, this change is 40% lower than the original 25 W/m·K. The errors in the reduced data for these adjusted properties are in Figure 48 and Table 16.

The significant drop in foam thermal conductivity is contributed to the contact area between the foam structure and the ceramic substrate. The effective thermal

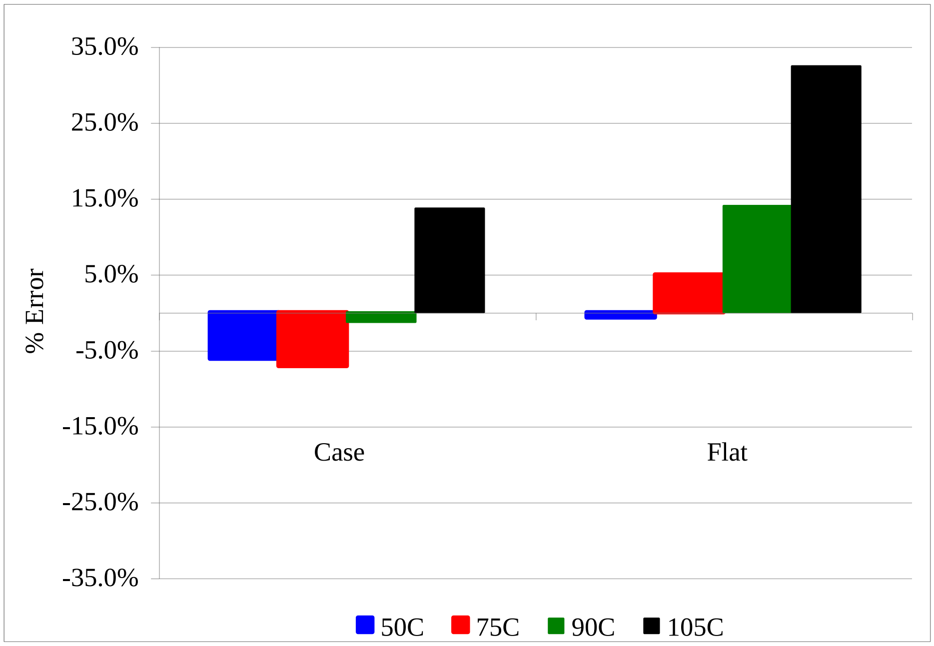

Figure 48. Relative error in adjusted Brinkman-Forchheimer model for annular structure, k_{foam} = 2 W/m.K, $k_{alumina}$=15 W/m.K

conductivity of the foam/fluid matrix is comprised of three components: thermal conductivity of the base metal, thermal conductivity of the working fluid, and the contact area of the foam to the substrate. The literature based thermal conductivity did not explicitly account for surface contact. The contact area between the foam and the ceramic substrate is small as shown in Figure 49. In the figure, the outer circumference of the annular foam section was inked and printed onto paper. The total visible contact area is less than 10%, which could be inferred from the foam's porosity. The effective conductivity of the duct region in the system must reflect this poor contact and thus is lower than the value suggested from literature for the isolated foam/fluid matrix.

The contact area can be influenced by assembly techniques, foam specifications, and manufacturing variations. Currently, the foam annulus was press fit into place. The press action caused the filaments and flat areas on the outer diameter of the foam to roll over and create point contacts between the metal foam and the substrate. The effective

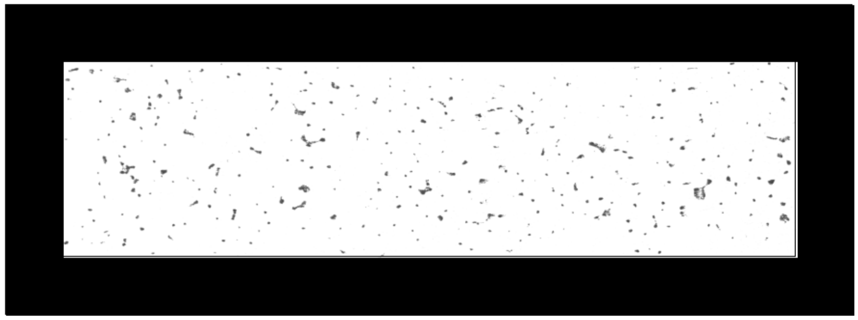

Figure 49. Inking of outer surface contact from aluminum foam annular insert

thermal conductivity could be improved by using a hot/cold assembly procedure so that the foam would grow into the wall. Then the foam would contact the substrate on small pads created at the intersecting webs of the foam structure. As the bond area improves, the effective thermal conductivity would increase to a value more typical of literature.

Another cause of the lower effective thermal conductivity was proposed by Prasad et al [28]. They suggest the effective thermal conductivity is dependent on the dominant heat transfer mechanism within the foam/fluid matrix. When convection from the foam dominates the conduction within the foam, the effective thermal conductivity trends toward the thermal conductivity of the working fluid. In this case, the implication would lower the thermal conductivity of the foam section.

Some variation from literature could be expected in the alumina; however, this much change over documented properties is not probable. The new model properties result in more conservativeness at the higher inlet temperatures. This model also over predicts the case temperature at 105°C inlet. Based on the thermal resistance argument, one would expect the case temperature to still be lower than the measured value.

The last source of error or under estimation in the COMSOL simulation may come from the flow model. Another set of models was solved by defining the flow under the Brinkman model. The Brinkman model was used for the annular structure because the coarse metal foam is only 2 or 3 pores thick as shown in Figure 50. Thus, the viscous shear effects near the wall are not as inhibited as they may be in denser foam with a lower

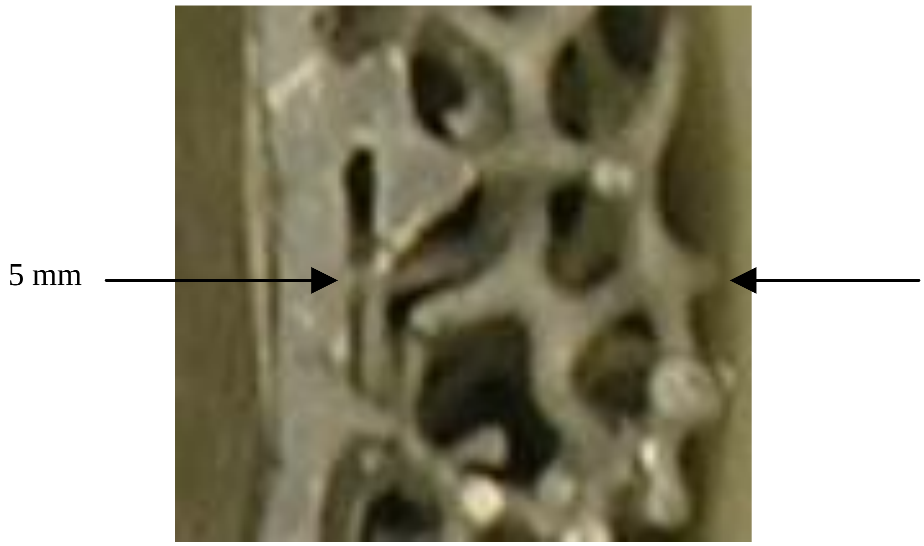

Figure 50. Close up view of foam annulus

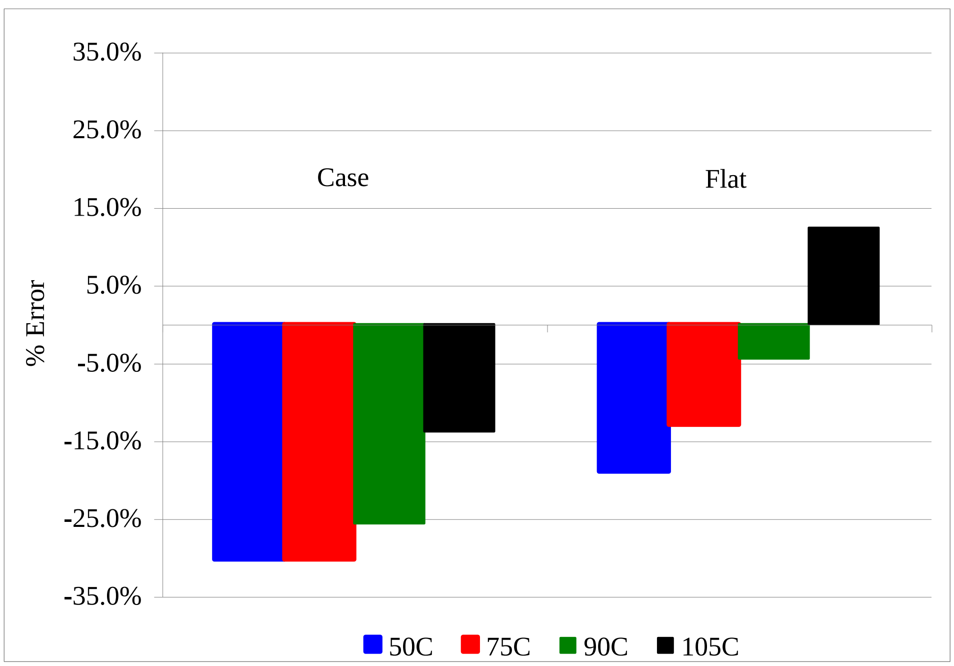

Figure 51. Relative error from Brinkman model for annular structure, k_{foam} = 2.5 W/m·K and $k_{alumina}$ = 25 W/m·K

porosity. Essentially, the Forchheimer correction is removed from the flow model, which will result in a lower pressure drop and less heat transfer to the fluid. For these models, the thermal conductivity of the alumina was left at 25 W/m·K, and the effective thermal conductivity of the foam was adjusted to 2.5 W/m·K. A comparison of models run under these conditions to the reduced experimental data is in Figure 51 and listed in Table 16. These properties and flow conditions still result in better agreement at 105°C as compared to the previously discussed models. They provide some conservativeness at the operating temperature of interest without drastically over shooting like in Figure 48.

Moreover, the case temperatures remain below the measured values to uphold the presence of a real thermal resistance. Also the thermal conductivity of alumina remains within more reasonable limits as compared to documented values. The Brinkman model with the parameters described above is considered the preferred model setup for the annular structure.

Four-hole

The data reduction process used for the annular case was used in evaluating the data from the four-hole design. To present the results, a numbering system is used to refer to geometric locations as shown in Figure 52 for a symmetric unit cell. The resistor footprint closest to the coolant channel is 1. The wirebond flat closest to the coolant channel is 2. The resistor footprint farther from the cooling channel is 3. The wirebond flat farther from the cooling channel is 4.

In Figure 53, the same data reduction process was followed for the four-hole design as for the annular structure. A table of these results is in Table 17. The data used to produce these results is in the Appendix. Again, the areas of most interest to verify the model parameters are locations 2 and 4 of the wirebond flats. The under estimates at location 1 and 3 were expected due to the thermal grease. Again as temperature increased, the models became more accurate but still resulted in lower of average temperatures as compared to the experimentation. Location 2 yields better results than location 4.

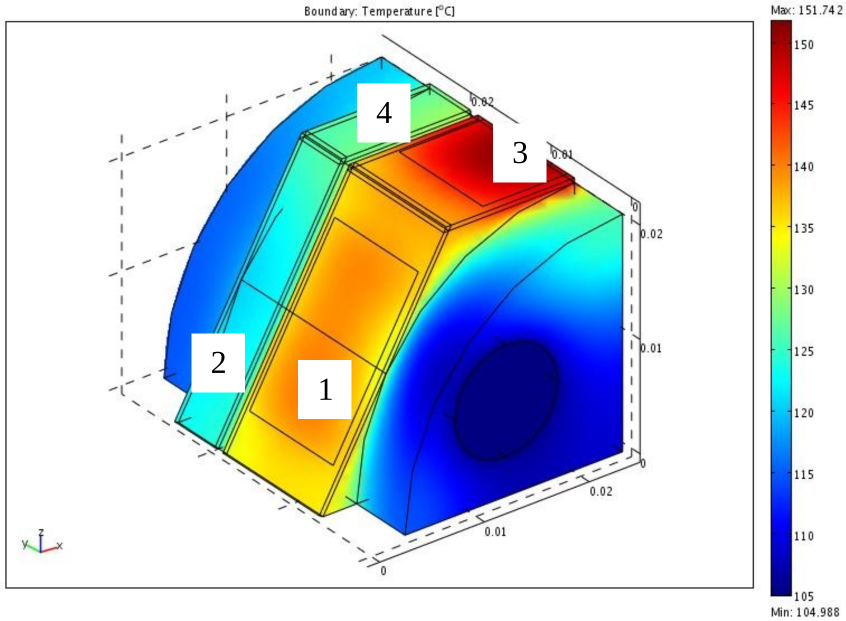

Figure 52. Sample FEA output for four-hole design

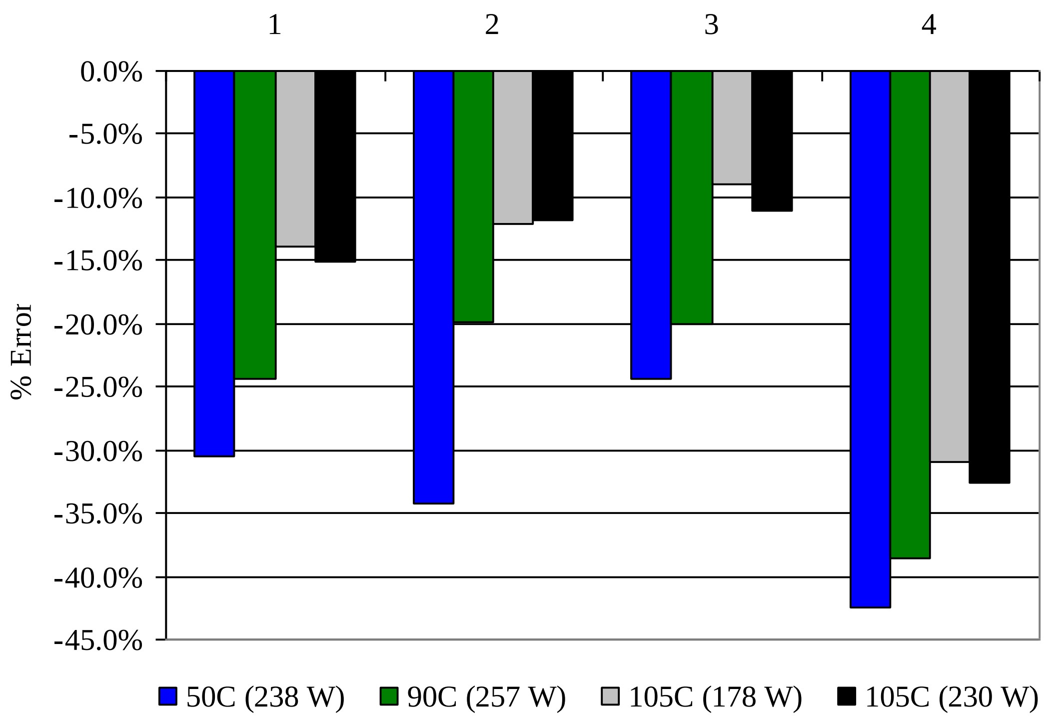

Figure 53. Initial four-hole COMSOL models error

Table 17. Comparison of original model results to experimental measurements for four-hole structure

Nominal Inlet Temperature (°C)	Electrical Power (W)	Heat added to Fluid (W)		Average Temperature at 1 (°C)	Average Temperature at 2 (°C)	Average Temperature at 3 (°C)	Average Temperature at 4 (°C)
50	329.8	238.1	Experimental	50.5	28.7	59.5	41.3
			COMSOL	35.1	18.9	45.0	23.8
			Error	-30.5%	-34.2%	-24.4%	-42.4%
90	181	146.3	Experimental	27.8	14.8	33.0	22.9
			COMSOL	21.4	11.5	27.5	14.4
			Error	-23.0%	-22.4%	-16.6%	-37.2%
90	330.7	257.1	Experimental	49.6	25.2	60.4	41.4
			COMSOL	37.5	20.2	48.3	25.4
			Error	-24.4%	-19.9%	-20.0%	-38.6%
105	211.1	178.2	Experimental	30.1	15.8	36.7	25.4
			COMSOL	25.9	13.9	33.4	17.5
			Error	-13.9%	-12.1%	-9.0%	-31.0%
105	270.5	230	Experimental	39.4	20.3	48.4	33.6
			COMSOL	33.4	17.9	43.1	22.6
			Error	-15.1%	-11.8%	-11.1%	-32.6%

In comparing the tables of the annular results to the four-hole results, the four-hole structure was able to handle more power at higher inlet temperatures. This result is interesting and may be attributed to several causes. One is the four-hole design had a slightly thicker copper cladding than the annular design. This would promote better heat spreading. Another is that the holes had 4 to 5 pores across the hole diameter to create more fluid mixing in the foam. This induced turbulence would help remove more heat from the substrate.

Again, changes to model parameters were sought to improve the model's representation of experimental results so that these parameters can be used to predict the thermal performance of future designs with confidence. The previous discussion about instrumentation error would apply in the four-hole design. Finer thermocouples and better accounting of the fluid energy balance may help the model to better match the experimental data.

The new thermal conductivities of the fluid/foam matrix and alumina were 2 W/m·K and 30 W/m·K, respectively. The fluid/foam thermal conductivity is the same as the first adjusted annular, and the thermal conductivity of the alumina is more in line with documented properties. The flow model for these simulations was the Brinkman flow with Forchheimer correction.

The results for the four-hole substrate with these updated material properties are in Figure 54. It was expected that the conservativeness in the model with the new properties would yield similar trends at both locations 2 and 4. However, location 2 was the only location to have higher temperatures. The under estimates at higher temperatures were only 4 – 5°C at location 4. Further adjustments in the four-hole model maybe required to make the predictions at location 4 more in line with location 2.

To examine possible error from the flow model, it was also adjusted with this design case. The Brinkman model was used with an effective foam thermal conductivity of 4 W/m·K. The thermal conductivity of the alumina was kept at the original value of 25 W/m·K. The results of these changes are in Figure 55.

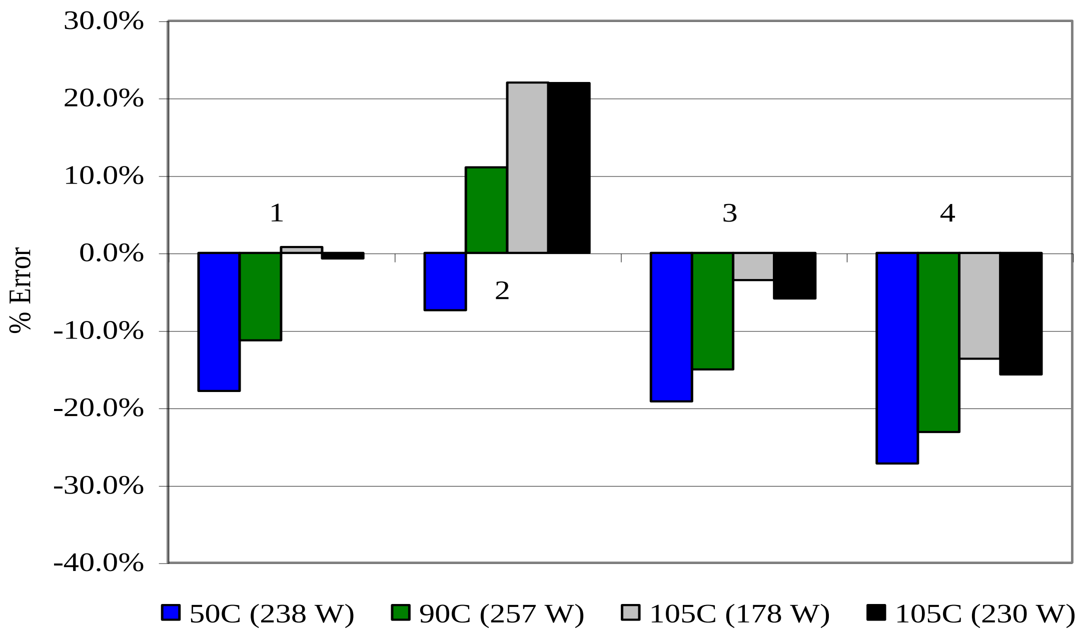

Figure 54. COMSOL model error for updated four-hole model with Brinkman-Forchheimer flow, k_{foam} = 2 W/m.K, and $k_{alumina}$ = 30 W/m.K

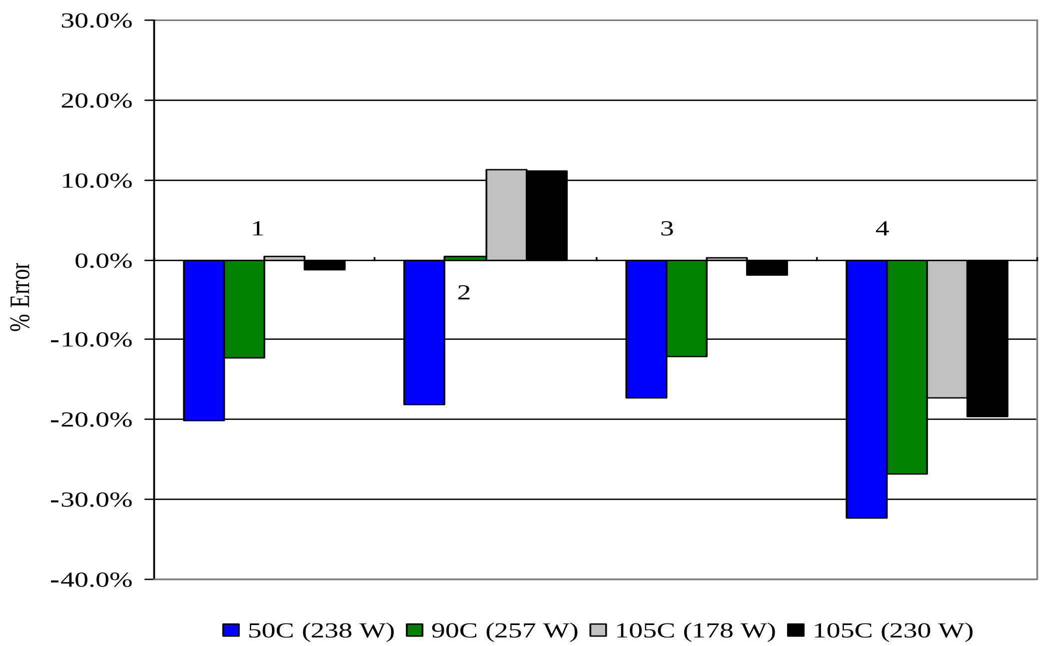

Figure 55. Error in Brinkman flow COMSOL model to experimental results where k_{foam} = 4 W/m·K, and $k_{alumina}$ = 25 W/m·K

Again, the average temperature at location 4 was under predicted despite the results being much closer for the average temperature at location 2 and 3 at the higher inlet temperatures. In fact, the under prediction at location 4 was worse than that from the Brinkman-Forchheimer model. The predicted thermal distribution at location 1 was similar for the Brinkman flow model with and without the Forchheimer correction with the Brinkman model predicting slightly lower temperatures than the Brinkman-Forchheimer model.

The thermal conductivity of the fluid/foam matrix could be reduced more in the Brinkman model to raise the temperature of location 4. This effect would also raise the predicted temperatures at the other locations, which might cause the average temperature under the resistor to be over predicted. Over estimating the case temperature would invalidate the thermal resistance assumption.

Even though location 4 is under estimated, the adjusted Brinkman-Forchheimer model appears to provide a better overall result for the thermal performance of the four-hole module. Some model consideration appears to be missing from the model as compared to experimental results. However, the error could also lie in the instrumentation.

In general the new model parameters, which were derived from the reduced experimental data, show that the fluid/foam matrix does not improve the effective thermal conductivity as much as originally believed. This effect may be improved by better assembly procedures to ensure better contact between the foam and ceramic substrate.

The suggested flow models are different for the two designs. This appears to be an effect of the size of the flow channel relative to the metal foam pore diameter. For the thin flow channel (2-3 pores wide) in the annulus, the center structure is not sufficient to suppress the viscous effects at the wall. Where as the larger channel (4-5 pores wide) in the four-hole design does help to flatten the velocity profile. The derived thermal conductivities of alumina are within 20% of each other. Some variation will exist in ceramic material properties because of the sintered nature of the product. The difference in the manufacturing temperature or pressure could cause this discrepancy.

Overall, these new models should provide a better basis for future predictions. Determining which flow channel geometry, annulus or four-hole, is better should only be made after the model corrections are applied to models that have equal thickness copper.

Chapter 6 - Updated Thermal Models

The final step in this design process is to apply the new model parameters to a model that includes sufficient geometric detail as described in Chapter 4. Those models utilized 1.27 mm thick copper plating. Over the elapsed time of a year, one major design change is the thickness of the copper plating. Despite several attempts, the vendor could not provide 1.27 mm of copper cladding. Learning from this process, the thickest metallization appears to be 0.3 mm (0.012"). Models based on the thickness of 0.3 mm and the best model parameters determined in Chapter 5 were executed. The results are present in this chapter.

Annulus

The results for the Brinkman model of the annular structure are in Table 18. Two cases were run. The first was at the original design load that equates to maximum heat load. In reality, this load may only be seen for a brief time. It was noticed during the experiment, that these structures have large thermal time constants because of ceramic's thermal inertia. The large time constant implies that the time to reach steady state far exceeds the operational time at peak load.

For this reason, a second thermal load was defined at the continuous load rating of 30 kW. The thermal load was taken from the experimental data in Figure 7 as an average of the operating points surrounding 30 kW output power. The average thermal load at this point was 1440 W. Dividing the heat loss between four switches and two diodes leads to 45 W/switch and 30 W/diode.

Note that neither solution is practical because the maximum fluid wall temperature exceeds the boiling point. For the alumina annular structure to work, its overall size will have to be increased.

Four-hole

The outcome of the four-hole design was similar as shown in Table 19. Both maximum fluid wall temperatures were above the boiling point of 50/50 WEG; thus, the

Table 18. Updated steady-state temperatures for annular structure with copper thickness of 0.3 mm

	Switch	Diode	Fluid Wall
Peak Load (55/36)	180	166.6	148.8
Cont Load (45/30)	166.5	156.2	140.9

Table 19. Updated steady-state temperatures for four-hole structure with copper thickness of 0.3 mm

	Switch	Diode	Fluid Wall
Peak Load (55/36)	177.4	173.5	158.6
Cont Load (45/30)	164.4	161.8	149

model is invalid. The overall size of the alumina structure will have to be increased in order to spread the heat more evenly to the flow channel.

The positive side is that if the fluid wall temperature can be decreased by 10-20°C then the device temperatures should fall accordingly. Then, the devices will be well within the design criteria for high temperature operation.

Possible improvements in the module assembly procedure and instrumentation may allow for better model parameters to be determined. However, until that work is complete, these parameters must be considered best practice.

Chapter 7 – Preliminary Inverter Design

In parallel with the experimental work, the overall inverter package was designed. Critical to any basic inverter design will be the manifold system used to supply WEG to the hexagonal modules. The initial simulations assumed that one sixth of the maximum allowable volumetric flow was possible through each module. The manifold design must distribute the flow evenly for the concepts discussed to be viable.

Two basic concepts were explored. The first design sought to place the modules inside of a hollow cylindrical capacitor. This technique has been used in previous projects [55] with great success in achieving reduced volume. The other basic design is to place the modules in a linear header and use a brick style capacitor.

Circular Manifold Design

In this cylindrical concept, the six modules would be evenly distributed in a round manifold and surrounded by a hollow cylindrical capacitor as show in Figure 56. In this picture, one manifold is removed for visual clarity. The phase leads would feed through one of the headers as shown in Figure 57. Some preliminary work was done on flow balance for this design. However, the total inverter package exceeded the target volume because of the outer diameter of the capacitor. The best power density for these designs was 10.4 kW/liter. This volume excluded an overall case and gate driver volume addition, which implies the ultimate specific power would be even smaller. Because this design did not meet the package design target of 12 kW/liter, it was not pursued any further.

Linear Header Design

In a parallel effort, a linear design was pursued. In this design, the six hexagonal prism modules were places in one row in a manifold. WEG would enter from one side and exit from the other. A picture of the package is in Figure 58 where one header is

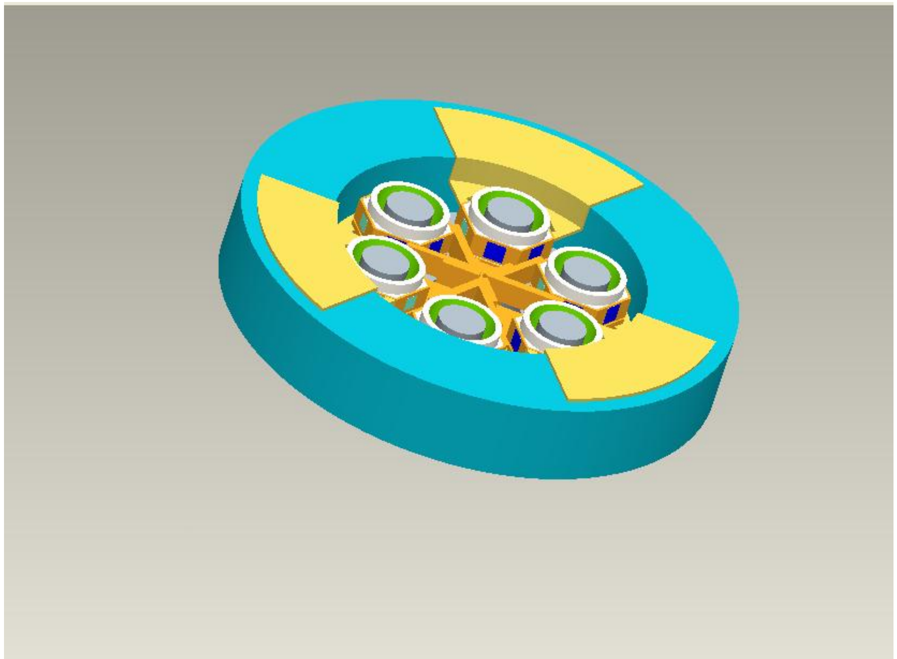

Figure 56. Cylinderical inverter package

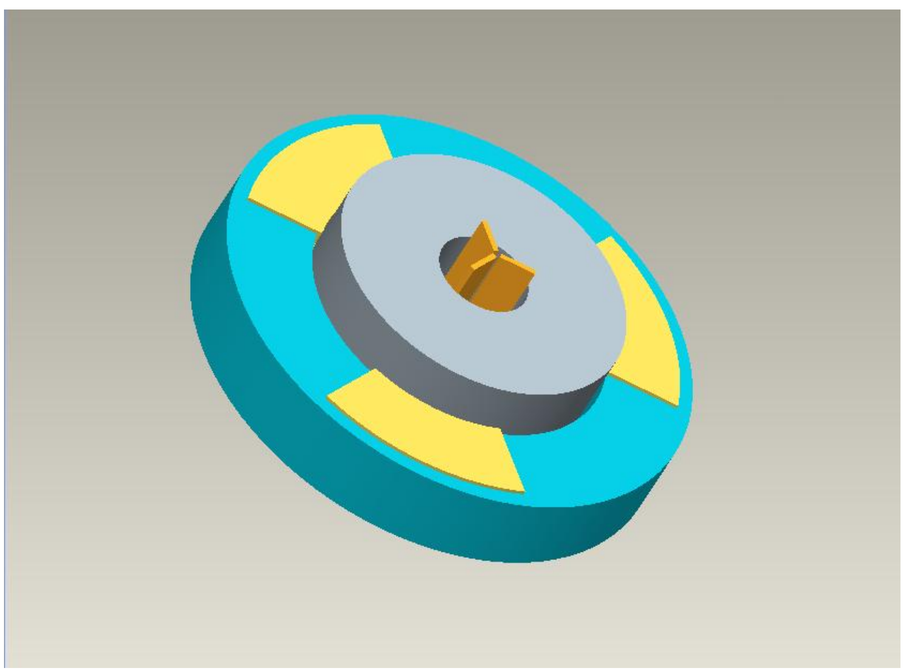

Figure 57. Cylinderical inverter package with phase bars

removed for visual clarity. This design greatly simplified the bus bar arrangement and allowed for the DC +/- bars to be laminated to reduce the electromagnetic interference (EMI). Figure 59 shows the complete package and provides a better representation of the phase connections.

The initial power densities for this design were 12.5 kW/liter, which exceeded the 12 kW/liter goal. For this reason, more fluid flow modeling was performed on this design. The manifold options that were explored are presented in the Appendix. The final configuration placed the inlet and outlet ports on the long sides of the headers. These ports are 90° from the axial flow direction of the substrates as shown in Figure 58. This location allows for the incoming fluid jet to impinge on a flat wall to then spread evenly to the porous channels.

After this design was presented to research sponsors, the stray inductance introduced by the electrical connection across the phase became an apparent concern. The stray inductance can lead to excessive EMI. Also, the bus attachment points were raised as an additional area for improvement. These suggestions along with the thermal model considerations have led to new investigations into octagonal structures that contain an entire inverter leg instead of the half leg investigated in this study. This type of structure will greatly simplify the electrical architecture, inverter assembly, and improve electrical performance. Future work will concentrate on using the simulation parameters and techniques confirmed in this research to explore the thermal feasibility of the second generation of direct-cooled ceramic substrates.

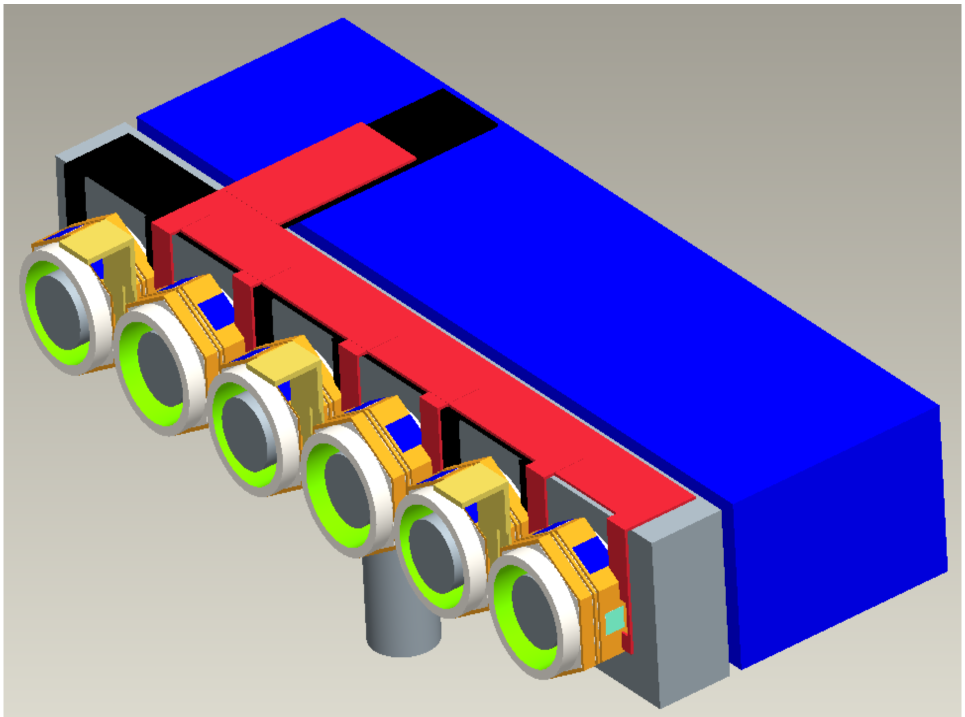

Figure 58. Linear package design

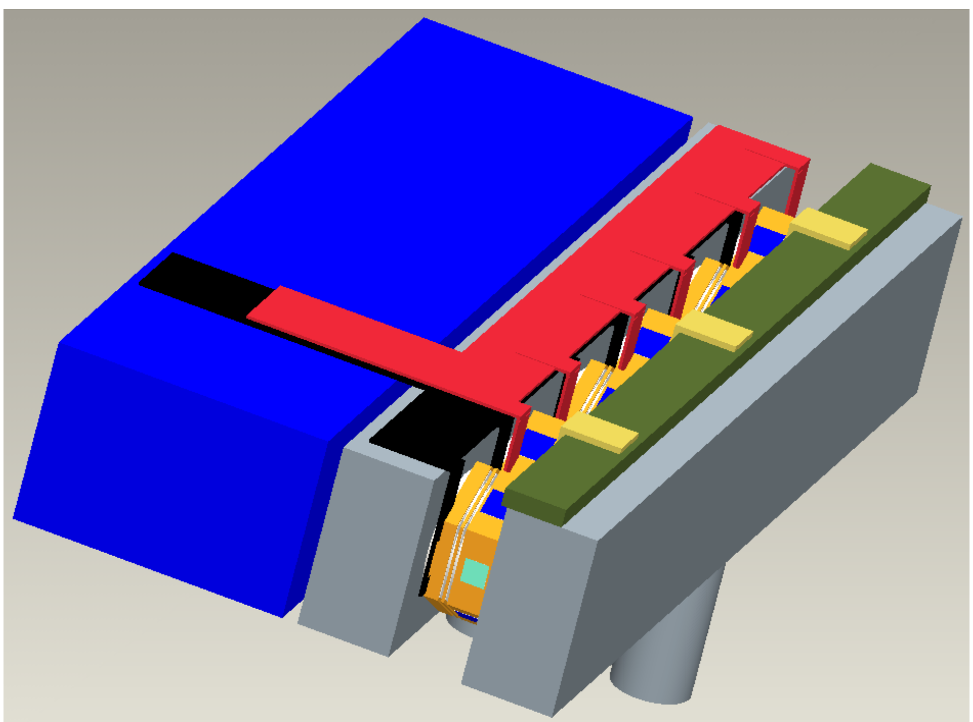

Figure 59. Complete linear inverter package

Chapter 8 – Conclusions and Recommendations

Unique designs of inverter packages were sought to enable operation with 105°C coolant. The proposed solution examined incorporating flow channels into the ceramic layer of the direct bonded copper substrate typically found in power electronic packages.

Four ceramic substrate materials were examined in the research. In general, the high thermal conductivity ceramics, AlN, BeO, and SiC, performed well. The lowest thermal conductivity ceramic, alumina, performed the poorest in initial designs. However, its low cost made it preferable for automotive mass manufacturing. In application areas, like defense, the superior performance of the other ceramic candidates may outweigh their increased costs, and AlN, BeO, and SiC should be considered.

In the free flow channel designs, the circular duct design proved to be the best shape for combined conduction and convective heat transfer. The circular duct performed better than rectangular and triangular ducts. Yet, the free flow design was not a viable option for the direct cooled substrate with 105°C WEG.

For alumina to result in a viable design, the overall cross-sectional area of the substrate must increase. Two channel designs demonstrated feasibility with larger alumina substrates. Metal foams were added to other flow channel geometries to enhance the effective thermal conductivity of the fluid. The duct geometries were an annular shape filled with aluminum foam and four discrete holes, 9.8 mm in diameter filled with aluminum foam.

The computational models of the annular and four-hole alumina substrate showed that the Darcy flow model resulted in the lowest temperature predictions. The Brinkman model resulted in the highest temperature distribution. The Brinkman model with the Forchheimer correction predicted temperature between the Darcy and Brinkman models. It is believed to be more realistic because it accounts for the added flow resistance that results from turbulence. From these simulations, the annular design appeared to be more robust than the four-hole design.

The pressure drop experimentation showed both foam inserts followed a Darcy-Forchheimer model over a wide operating range. However, the exact flow model behavior at the operating point of 2.5 GPM was not conclusive from the pressure drop data. The measured permeability for the annular structure was 9.64×10^{-8} m^2 with a Forchheimer drag coefficient of 0.072. The measured permeability for the four-hole design was 6.54×10^{-8} m^2 with a Forchheimer drag coefficient of 0.056. These measured flow parameters were within reasonable limits of other values reported in literature.

Because of the inconclusive interpretation of the pressure drop results, an alternative data reduction technique was implemented. This method produced nondimensional quantities that better agreed with the model. In future work, the flow parameters from this reduction method need to be implemented into the thermal models to reevaluate the model predictions.

The thermal validation experiment showed that the models under predicted the temperature distribution. This result was expected for the chip temperatures because of the contact resistance. For other measured temperatures, the difference was not expected. At 105°C, the simulations were closer to the experimental results than at lower coolant temperatures. This is attributed to better foam/substrate contact because of thermal expansion.

Alterations in the thermal conductivity of the metal/foam matrix, alumina, and prescribed flow model were made to produce model parameters that gave results that better reflected the reduced data. In both cases, the thermal conductivity of the foam was reduced from 7.2 $W/m \cdot K$ to ~2 $W/m \cdot K$. The effective thermal conductivity of the fluid/foam matrix reflects the quality of the contact of the foam with the ceramic substrate. Better assembly techniques need to be explored to ensure a positive thermal contact between the foam structure and the ceramic substrate.

It was found that the Brinkman model actually described the flow in the annular channel better at maximum operating flow rate. Foam structures with only 2-3 pores in thickness do not inhibit the boundary layer development. Therefore, the viscous shear effects should be included. The Brinkman-Forchheimer flow model best described the four-hole operation because its diameter is 4-5 pores wide.

The computer models for the annular and four-hole designs were reexcecuted with the updated model parameters from experimentation and a reduced copper cladding thickness. These models did not meet the design criteria. The cross-sectional area of the alumina substrate would need to increase again in order to meet the design criteria with a coolant of 105°C.

The overall inverter package was considered. A linear manifold layout gave the best flow distribution. The power density of this design exceeded the 12 kW/liter goal. Technical review of the inverter package raised concerns about stray inductance and EMI. Incorporating the entire inverter leg on one module would alleviate these losses. This would reduce the total number of substrates from six to three. The electrical layout would require two chips in the axial direction. Moving toward an octagonal shape would also help simplify the electrical connections. With the modeling parameters established in this research, further models can be developed to improve upon the initial designs with confidence.

List of References

[1] J. S. Hsu, R. H. Staunton, and M. R. Starke, “Barriers to the application of high temperature coolants in hybrid electric vehicles,” Oak Ridge National Laboratory, TM Report ORNL/TM-2006/514, 2006.

[2] R. W. Johnson, J. L. Evans, P. Jacobsen, and J. R. Thompson, “The changing automotive environment: High-temperature electronics,” *IEEE Transactions on Electronics Packaging Manufacturing*, vol. 27, no. 3, pp. 164–176, July 2004.

[3] N. R. Jankowski, L. Everhart, B. Morgan, B. Geil, and P. McCluskey, “Comparing microchannel technologies to minimize the thermal stack and improve thermal performance in hybrid electric vehicles,” *IEEE Transactions on Vehicle Power and Propulsion*, pp. 124–130, September 9-12 2007.

[4] N. Mohan, T. Undeland, and W. Robbins, *Power Electronics: Converters, Applications, and Design*, 3rd ed. New Jersey: John Wiley & Sons, Inc, 2003.

[5] S. C. Nelson and C. W. Ayers, “Testing of the SemiKron validation AIPM unit,” Oak Ridge National Laboratory, TM Report ORNL/TM-2005/44, January 2005.

[6] R. H. Wiles, A. A. Wereszczak, K. T. Lowe, and C. W. Ayers, “Direct cooled power electronics substrate,” Oak Ridge National Laboratory, US Patent Application 20090231812, September 2009.

[7] D. B. Tuckerman and R. F. W. Pease, “High-performance heat sinking for VLSI,” *IEEE Electron Device Letters*, vol. 2, no. 5, pp. 126–139, May 1981.

[8] W. Anacker, “Liquid cooling of integrated circuit chips,” IBM, IBM Technical Disclosure Bulletin Vol. 20, No. 9, February 1978.

[9] D. Nayak, L.-T. Hwang, I. Turlik, and A. Reisman, “A high-performance thermal module for computer packaging,” *Journal of Electronic Materials*, vol. 16, no. 5, pp. 357–364, 1987.

[10] N. R. Jankowski, L. Everhart, B. R. Geil, C. W. Tipton, J. Chaney, T. Heil, and W. Zimbeck, “Stereolithographically fabricated aluminum nitride microchannel substrates for integrated power electronics cooling,” *IEEE Transactions on Thermal and Thermomechanical Phenomena in Electronic Systems (ITHERM)*, pp. 180–188, May 28-31 2008.

[11] K. Exel and J. Schulz-Harder, “Water cooled DBC direct bonded copper substrates,” *IEEE Proceedings of Industrial Electronics Society*, pp. 2350–2354, 1998.

[12] C. Gillot, C. Schaeffer, C. Massit, and L. Meysenc, “Double-sided cooling for high power IGBT modules using flip chip technology,” *IEEE Transactions on Components and Packaging Technologies*, vol. 24, no. 4, pp. 698–704, December 2001.

[13] H. Baumann, P. Heinemeyer, W. Staiger, M. Topfer, K. Unger, and D. Muller, “Optimized cooling systems for semiconductor devices,” *IEEE Proceedings of Industrial Electronics Society*, pp. 2336–2341, 1998.

[14] K. Olesen, “Liquid cooled power modules for automotives,” Danfoss Silicon Power, http://www.ixlogic.ch/Danfoss/News/Shower%20Power%20Technical%20Note%20en.pdf, Technical Note, July 13 2009.

[15] K. Olesen, R. Bredtmann, and R. Eisele, “"Shower Power" new cooling concept for automotive applications,” Automotive Power Electronics, http://www.danfoss.com/NR/rdonlyres/E806D330-3A12-4A97AE6DFB58653DA752/0/ShowerPowerNewCoolingConceptforAutomotive_APE2006.pdf, June 2006.

[16] K. Olesen, R. Bredtmann, R. Eisele, and F. Osterwald, “"Power under the hood" increasing power density of inverters with a novel 3d-approach,” On-Line, http://www.danfoss.com/NR/rdonlyres/EF64FA19-F983-4183-84DA81C3B05FF08E/0/UnderthehoodpowermoduleassembliesAPE2009.pdf.

[17] J. Valenzuela, T. Jasinski, and Z. Sheikh, “Liquid cooling for high-power electronics,” *Power Electronics Technology*, pp. 50–56, February 2005.

[18] M. O’Keefe and K. Bennion, “Comparison of hybrid electric vehicle power electronics cooling options,” *IEEE Vehicle Power and Propulsion*, pp. 116–123, September 9-12 2007.

[19] D. Bharathan and K. Kelly, “An assessment of air cooling for use with automotive power electronics,” in *Thermal and Thermomechanical Phenomena in Electronic Systems, 2008. ITHERM 2008. 11th Intersociety Conference on*, May 2008, pp. 37–43.

[20] C. W. Ayers, “Thermal buffer heat sink for time-averaged operating conditions,” in *Annual Progress Report for the Advanced Power Electronics and Electric Machinery Program*. Department of Energy, 2007, pp. 13–20.

[21] K. T. Lowe, R. V. Arimilli, and C. W. Ayers, “Thermal buffer heat sink for time-averaged operating conditions,” University of Tennessee and Oak Ridge National Laboratory, subcontract report, 2007.

[22] P. Salvati, R. Brucchi, and A. De Medici, “Application note: Sinusoidal inverter using Semitop modules for electric vehicles applications,” SemiKron, Tech. Rep. [Online]. Available: http://www.semikron.com/internet/webcms/objects/pdf/-semitop_sinusoidal_inverter_%20for_ev.pdf

[23] “SIGC100T60R3,” Online, INFINEON Technologies, Data Sheet, January 2005.

[24] L. Marlino, “Flow rate numbers and temperatures for FreedomCAR goals,” Personal Communications, November 2007.

[25] “Meglobal: Ethylene glycol product guide,” On-line, http://www.meglobal.biz/literature/product_guides/MEGlobal_MEG.pdf, July 31 2008.

[26] A. Wereszczak, “Ceramic property data,” Personal Communications, October 2007.

[27] V. V. Calmidi and R. L. Mahajan, “The effective thermal conductivity of high porosity fibrous metal foams,” *Journal of Heat Transfer*, vol. 121, pp. 466–471, 1999.

[28] V. Prasad, F. A. Kulacki, and M. Keyhani, “Natural convection in porous media,” *Journal of Fluid Mechanics*, vol. 150, pp. 89–119, 1985.

[29] *COMSOL 3.5a Materials Library*, COMSOL Multiphysics.

[30] F. M. White, *Viscous Fluid Flow*, 3rd ed. McGraw Hill, 2006.

[31] ——, *Fluid Mechanics*, 5th ed. McGraw Hill, 2003.

[32] A. Bejan, *Convection Heat Transfer*, 3rd ed. John Wiley & Sons, Inc, 2004.

[33] F. P. Incropera and D. P. Dewitt, *Fundamentals of Heat and Mass Transfer*, 5th ed. John Wiley & Sons, Inc, 2002.

[34] F. P. Incropera, *Liquid Cooling of Electronic Devices by Single-phase Convection*, A. D. Kraus and A. Bar-Cohen, Eds. John Wiley & Sons, Inc, 1999.

[35] R. K. Shah and A. L. London, *Laminar Flow Forced Convection in Ducts*. New York: Academic Press, 1978.

[36] R. J. Phillips, "Forced-convection, liquid-cooled, microchannel heat sinks," Lincoln Laboratory, Massachusetts Institute of Technology, Tech. Rep. 787, 1988.

[37] *2D Axisymmetric Transient Heat Transfer*, COMSOL Multiphysics Modeling Guide Version 3.4, 2007.

[38] R. Wiles, C. W. Ayers, A. Wereszczak, and K. T. Lowe, "Direct-cooled power electronics substrate," Oak Ridge National Laboratory, Tech. Rep. ORNL/TM-2008/112, 2008.

[39] A. F. Mills, *Basic Heat and Mass Transfer*, 2nd ed., M. Horton, Ed. Prentice Hall, 1999.

[40] J.-P. Bonnet, F. Topin, and L. Tadrist, "Flow laws in metal foams: Compressibility and pore size effects," *Transport in Porous Media*, vol. 73, pp. 233–254, 2008.

[41] M. Kaviany, *Principles of Heat Transfer in Porous Media*, 2nd ed., F. F. Ling, Ed. Springer, 1995.

[42] J. L. Lage, "The fundamental theory of flow through permeable media from Darcy to turbulence," in *Transport Phenomena in Porous Media*, D. B. Ingham and I. Pop, Eds. Pergamon, 1998, vol. 1, pp. 1–30.

[43] D. A. Nield and A. Bejan, *Convection in Porous Media*, 2nd ed. Springer, 1999.

[44] T. Norton, "Modeling of corrugated graphite foam heat exchangers," Master's thesis, University of Tennessee, 2003.

[45] *Porous Media Flow Minicourse*. COMSOL, 2008.

[46] A. Amiri and K. Vafai, "Transient analysis of incompressible flow through a packed bed," *International Journal of Heat and Mass Transfer*, vol. 41, no. 24, pp. 4259 – 4279, 1998. [Online]. Available: http://www.sciencedirect.com/science/article/B6V3H-3WDK665-J/2/757df3c5c0993ebe4d64a2daef3ca15a

[47] A. Bhattacharya, V. V. Calmidi, and R. L. Mahajan, "Thermophysical properties of high porosity metal foams," *International Journal of Heat and Mass Transfer*, vol. 45, pp. 1017–1031, 2002.

[48] S. Miwa and R. T. Shripad, "Hydrodynamic characterization of nickel metal foam, part 1: Single-phase permeability," *Transport in Porous Media*, March 2009. [Online]. Available: http://www.springerlink.com/content/a87648558um1715k/

[49] "Quotation / specification quote: 6112r2 mercury mcht100-e1-k10-ps an air-cooled closed loop refrigerated fluid recirculator," BV Thermal Systems LLC, 1064 Woodland Ave. Suite K, Modesto, CA 95351, Tech. Rep., 2008. [Online]. Available: www.bayvoltex.com

[50] "Omega px105 series pressure transducer instruction sheet." [Online]. Available: http://www.omega.com/pptst/PX105.html

[51] Setra, "Installation guide model 230 wet/wet differential pressure transducer," Online. [Online]. Available: http://www.setra.com/tra/ins/pdfs/m230.pdf

[52] L. W. Jin and K. C. Leong, "Pressure drop and friction factor of steady and oscillating flows in open-cell porous media," *Transport in Porous Media*, vol. 72, pp. 37–52, 2008.

[53] "MP2060 Kool-Pak clip mount power film resistor," Caddock Electronics Inc, Tech. Rep., 2009. [Online]. Available: http://www.mouser.com/Passive-Components/-Resistors/Power-Resistors/_/N-2gra1?P=1z0x7asZ1z0wljoZ1z0vkni

[54] MatWeb, "G-10 fiberglass epoxy laminate sheet," Online, 2009. [Online]. Available: http://www.matweb.com/search/DataSheet.aspx?MatGUID=8337b2d05 0d44da1b8a9a5e61b0d5f85

[55] C. W. Ayers, J. C. Conklin, J. S. Hsu, and K. T. Lowe, "A unique approach to power electronics and motor cooling in a hybrid electric vehicle environment," in *Vehicle Power and Propulsion Conference, 2007. VPPC 2007. IEEE*, Sept. 2007, pp. 102–106.

[56] Keithley, "2700, 2701, 2750 multimeter/data acquisition/switch systems data sheet." [Online]. Available: http://www.keithley.com/data?asset=51943

[57] "Omega linear thermistor composite 44108 data sheet," 1988.

[58] S. J. Kline and F. A. McClintock, “Describing uncertainties in single sample experiments,” *Mechanical Engineering*, vol. 75, January 1953.
[59] R. S. Figliola and D. E. Beasley, *Theory and Design for Mechanical Measurements*, 3rd ed. John Wiley & Sons Inc, 2000.

Appendices

A.1. Sample Matlab code for shape factor determination of rectangular channels

```
% COMSOL Multiphysics Model M-file
% Generated by COMSOL 3.5 (COMSOL 3.5.0.494, $Date: 2008/09/19 16:09:48
$)
clc
clear all
close all

width=[.01 .011 .012 .013 .014 .015];
height=[.001 .002 .003 .004 .005 .006 .007 .008];
del=[.001921 .002061 .002215 .002384 .002569 .002769];

for ii=1:1:length(width)
    for jj=1:1:(length(height)-ii+1)
flclear fem

% COMSOL version
clear vrsn
vrsn.name = 'COMSOL 3.5';
vrsn.ext = '';
vrsn.major = 0;
vrsn.build = 494;
vrsn.rcs = '$Name:  $';
vrsn.date = '$Date: 2008/09/19 16:09:48 $';
fem.version = vrsn;

% Geometry
g1=curve2([-0.012,0.012],[0.020784609690826527,0.020784609690826527]);
carr={curve2([-0.012,0],[0.020784609690826527,0],[1,1]), ...
  curve2([0,0.012],[0,0.020784609690826527],[1,1]), ...
  curve2([0.012,-
0.012],[0.020784609690826527,0.020784609690826527],[1,1])};
g2=geomcoerce('solid',carr);
parr={point2(-0.0050,0.0207846096908265), ...
  point2(0.0050,0.0207846096908265)};
g6=geomcoerce('point',parr);
g7=rect2(width(ii),height(jj),'base','corner','pos',{-
width(ii)/2,(.012*sqrt(3)-height(jj)-del(ii))},'rot','0');

g8=geomcomp({g2,g7},'ns',{'g2','g7'},'sf','g2-g7','edge','none');

parr={point2(0,0.0207846096908265)};
g2=geomcoerce('point',parr);

% Analyzed geometry
clear p c s
p.objs={g6,g2};
p.name={'PT1','PT2'};
p.tags={'g6','g2'};
```

```
c.objs={g1};
c.name={'B1'};
c.tags={'g1'};

s.objs={g8};
s.name={'CO2'};
s.tags={'g8'};

fem.draw=struct('p',p,'c',c,'s',s);
fem.geom=geomcsg(fem);

% Initialize mesh
fem.mesh=meshinit(fem, ...
                  'hauto',5);

% Refine mesh
fem.mesh=meshrefine(fem, ...
                    'mcase',0, ...
                    'rmethod','regular');

% Refine mesh
fem.mesh=meshrefine(fem, ...
                    'mcase',0, ...
                    'rmethod','regular');

% Refine mesh
fem.mesh=meshrefine(fem, ...
                    'mcase',0, ...
                    'rmethod','regular');

% (Default values are not included)

% Application mode 1
clear appl
appl.mode.class = 'GeneralHeat';
appl.module = 'HT';
appl.shape = {'shlag(1,''J'')','shlag(2,''T'')'};
appl.sshape = 2;
appl.assignsuffix = '_htgh';
clear prop
prop.analysis='static';
appl.prop = prop;
clear bnd
bnd.type = {'q0','T','T'};
bnd.q0 = {0,0,1};
bnd.shape = 1;
bnd.T0 = {273.15,0,1};
bnd.ind = [1,1,2,2,2,3,1,3,2,1];
appl.bnd = bnd;
clear equ
equ.sdtype = 'supg';
equ.rho = 0;
equ.shape = 2;
equ.C = 0;
```

```
equ.k = 1;
equ.ind = [1];
appl.equ = equ;
fem.appl{1} = appl;
fem.frame = {'ref'};
fem.border = 1;
fem.outform = 'general';
clear units;
units.basesystem = 'SI';
fem.units = units;

% ODE Settings
clear ode
clear units;
units.basesystem = 'SI';
ode.units = units;
fem.ode=ode;

% Multiphysics
fem=multiphysics(fem);

% Extend mesh
fem.xmesh=meshextend(fem);

% Solve problem
fem.sol=femstatic(fem, ...
                  'solcomp',{'T'}, ...
                  'outcomp',{'T'}, ...
                  'blocksize','auto');

% Save current fem structure for restart purposes
fem0=fem;

% Integrate
I1(jj,ii)=postint(fem,'ntflux_htgh', ...
           'unit','W/m', ...
           'recover','off', ...
           'dl',[6,8], ...
           'edim',1)

 %Change to flux boundary
% (Default values are not included)
% Application mode 1
clear appl
appl.mode.class = 'GeneralHeat';
appl.module = 'HT';
appl.shape = {'shlag(1,''J'')','shlag(2,''T'')'};
appl.sshape = 2;
appl.assignsuffix = '_htgh';
clear prop
prop.analysis='static';
appl.prop = prop;
clear bnd
bnd.type = {'q0','T','q'};
```

```
bnd.q0 = {0,0,(1/.01)};
bnd.shape = 1;
bnd.T0 = {273.15,0,1};
bnd.ind = [1,1,2,2,2,3,1,3,2,1];
appl.bnd = bnd;
clear equ
equ.sdtype = 'supg';
equ.rho = 0;
equ.shape = 2;
equ.C = 0;
equ.k = 1;
equ.ind = [1];
appl.equ = equ;
fem.appl{1} = appl;
fem.frame = {'ref'};
fem.border = 1;
fem.outform = 'general';
clear units;
units.basesystem = 'SI';
fem.units = units;

% ODE Settings
clear ode
clear units;
units.basesystem = 'SI';
ode.units = units;
fem.ode=ode;

% Multiphysics
fem=multiphysics(fem);

% Extend mesh
fem.xmesh=meshextend(fem);

% Solve problem
fem.sol=femstatic(fem, ...
                  'init',fem0.sol, ...
                  'solcomp',{'T'}, ...
                  'outcomp',{'T'}, ...
                  'blocksize','auto');

% Save current fem structure for restart purposes
fem0=fem;

% Integrate
I2=postint(fem,'T', ...
           'unit','K', ...
           'recover','off', ...
           'dl',[6], ...
           'edim',0);
       S_Tmax(jj,ii)=1/I2
    end
end
```

A.2. Parametric study for flow channel in four-hole alumina design

The placement of the coolant channel in the four-hole design is more complex than simply centering the hole under one face. Because each hole is managing heat from two sources, the placement of the hour location and size in critical to the design's performance. This section explores the variations in dimensions and their effect on relevant temperatures.

A general dimensional drawing of the design is in Figure 60. L is one half of the length of a hexagonal side. α is the distance between the surface of the substrate and the fluid channel. ζ and β are the distances from the cylinder to the adiabatic planes of symmetry, respectively. While α must exceed 1.27mm, ζ and β must exceed half of that distance in order to satisfy manufacturing design limitations.

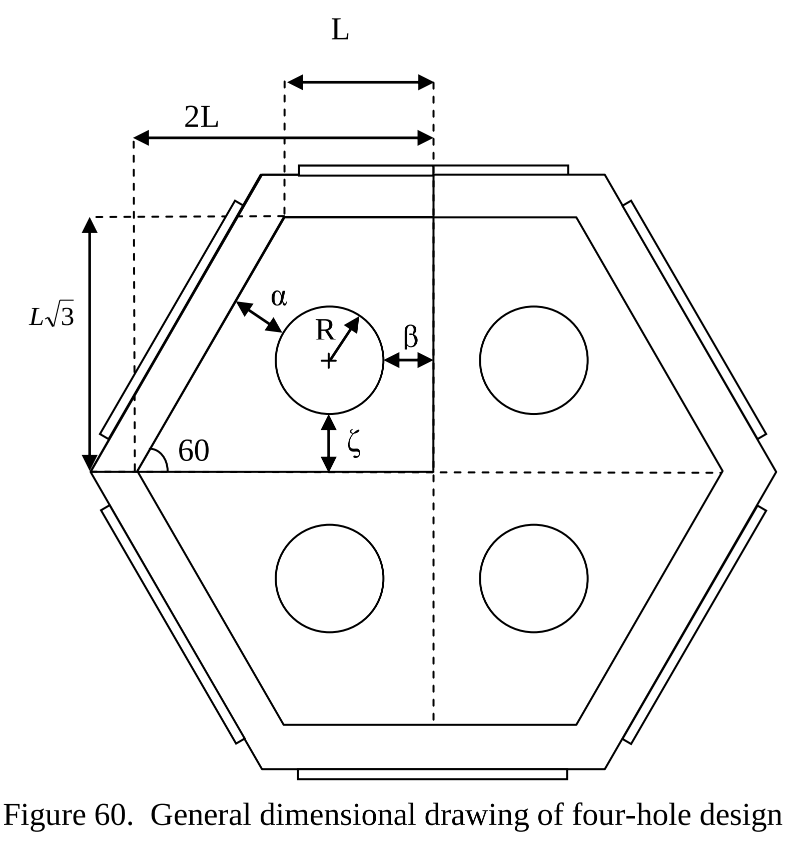

Figure 60. General dimensional drawing of four-hole design

The general approach to determining the best dimensions for the four-hole design was to start with the hole the minimum distance from hexagon side and translate it parallel to the side to exam the optimal placement to balance the heat load. This general motion is depicted in Figure 61. The offset from the hexagon's edge and the diameter of the hole were altered in several iterations to arrive at the best thermal performance. The first case used a hole radius of 3 mm and the minimum offset, α = 1.27 mm (0.050"). For initial designs, the heat load was uniform in both the side and top chip.

The results are in Figure 62. The top chip temperature decreases as the coolant channel moves farther from the center of the side chip. Likewise, the temperature of the side chip increases during the translation. The fluid temperature remains fairly constant until the center of the chip extends beyond the dimension of the chip. Then, the fluid wall temperature begins to decrease. An offset point exists where the top and side chip temperatures are essentially equal. This point is chosen as the optimum position of the coolant channel for the particular geometry parameters.

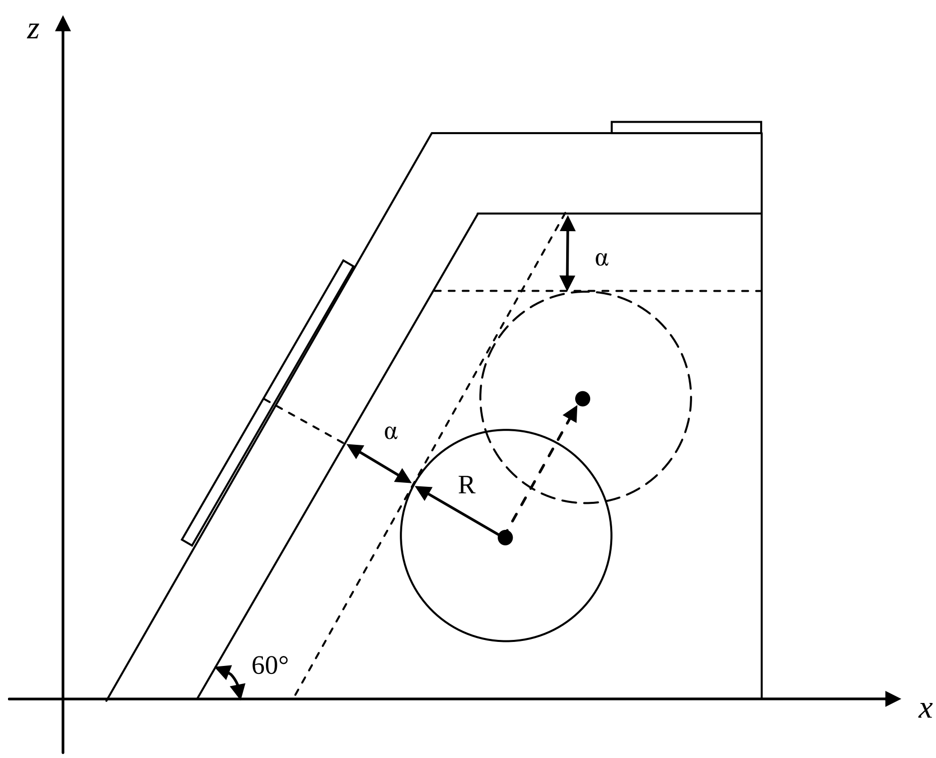

Figure 61. General motion of hole translation

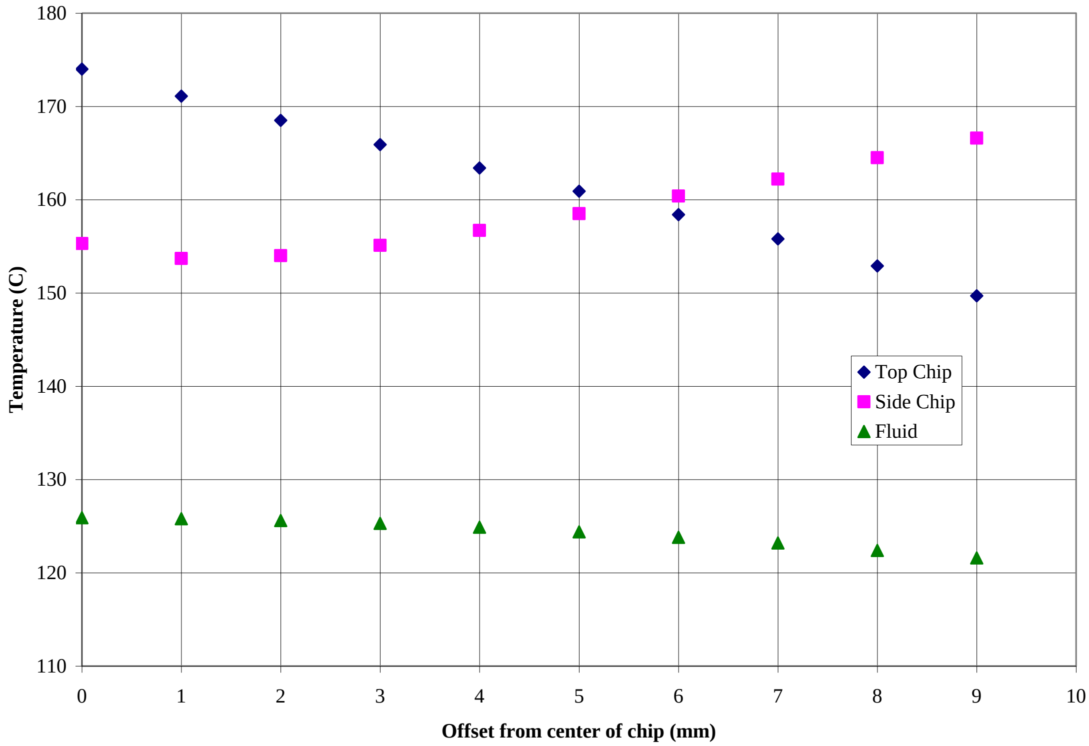

Figure 62. Design temperature results for 3 mm radius hole, α=1.27 mm

However, at the point of intersection, the maximum temperatures exceeded the design limit. A new parametric model was created with the coolant channel offset from the chip by 5.5 mm. In this model, the hole radius was increased parametrically from 3mm to 5 mm. Because the fluid temperature was sufficiently lower than the design criteria for these dimensions, the coolant channel radius was increased to provide more surface area for cooling to decrease the chip temperature. The hole distance from the hexagon side was increased to 1.91 mm to assure the fluid temperature would remain below 128°C since the hole velocity will decrease with increasing cross-sectional area. The results are in Table 20 with the lowest chip temperatures obtained with a radius of 4.9 mm. This radius also represents the maximum radius that does not exceed the maximum fluid design criteria.

Table 20. Results on increasing coolant channel radii at 5.5 mm channel offset from center of side chip

R (mm)	Top Chip (ºC)	Side Chip (ºC)	Fluid (ºC)
3	157.7	156.1	125.7
4	156.1	157.2	126.2
4.5	154.8	156.6	127.2
4.8	154.2	156.3	127.8
4.9	153.9	156.3	128.0
5	153.8	156.2	128.2

The new dimension for the hole and placement did not exhibit the desired temperature balance between the two chips; the maximum chip temperatures differed by 2.5°C. To make sure the offset distance was optimized, a channel of radius 4.9 mm was translated from the chip center toward the top chip in parallel with the hexagon side. Also for this case, the heat load was changed to the associated loading for the switch (55W) and diode (36W) instead of equal thermal loading which had been done up to this point for the four-hole design.

The results for this translation are in Figure 63. As a result of the proportional heat load, the desired cylinder placement shifts from the previous position to a 2 mm offset. At this point, the switch and diode are both near 150°C, and the temperature of the fluid is at 128.5ºC, which is slightly above the design criterion but is below the absolute maximum. This model satisfies the operating requirements.

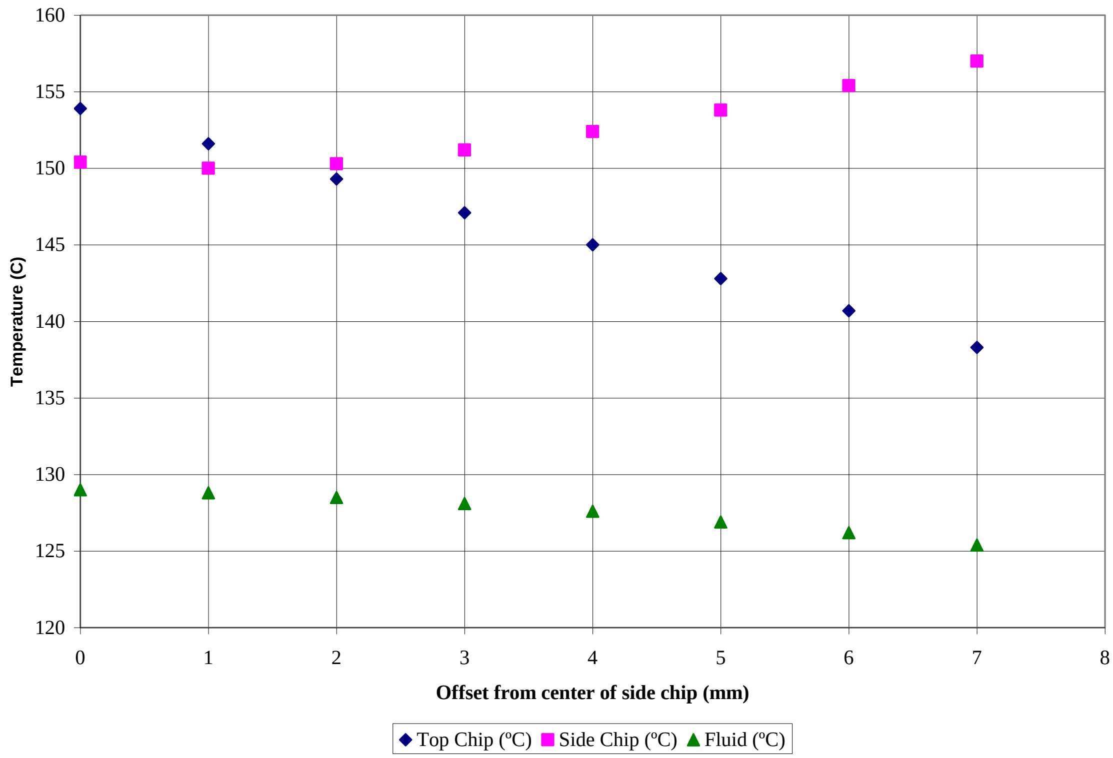

Figure 63. Results for translation of 4.9 mm hole with distributed load

A.3. Rotameter Calibration

The rotameter that is attached to the constant temperature bath (Bay Voltex) has to be calibrated for 50/50 water ethylene glycol (WEG). The factory calibrations are for water and air. To calibrate the rotameter, the internal reservoir had to be extended because of a low level cut out in the control system. The internal reservoir would only hold several cups beyond the low level cut out. The cut out limits the amount of liquid that can be pumped into a container for the calibration.

The calibration method consists of recording the time required to fill a graduated container to a predetermined mark. A large volume (3440 mL) of liquid was used as the calibration volume so that uncertainty in the timing, container level, and fill volume would be minimized. A schematic of the set up is in Figure 64.

While the Bay Voltex constant temperature bath comes up to temperature, the fluid bypasses the calibration container via the diverting valve. When the temperature settles at the set point, the fluid is redirected to Position 1 at the extended reservoir for collection. The flow control valve, which is located after the rotameter and before the diverting valve, regulates the flow rate. Once the flow rate stabilized at a rotameter scale reading, the flow is moved to Position 2 to begin the calibration. The time was recorded for the graduated cylinder to fill to a predetermined mark. This volume to this mark was measured to be 3440 mL. Once full, the fluid was diverted through the bypass, and the fluid flow rate was increased by opening the flow control valve. This procedure was repeated until enough data was collected to form a calibration curve. The data is documented in Table 21.

The results of the calibration procedure are shown in Figure 65. The calibration procedure was completed for five temperatures between 24.5ºC and 84.1ºC. More data was collected at the lower flow rates because this range will be the typical operating range of the unit for experiments.

Little to no variation is observed in the calibration for different temperatures. This invariance is contributed to only small changes in density over the range of temperature. From manufacturer's specifications, the density of 50/50 WEG at 25ºC and

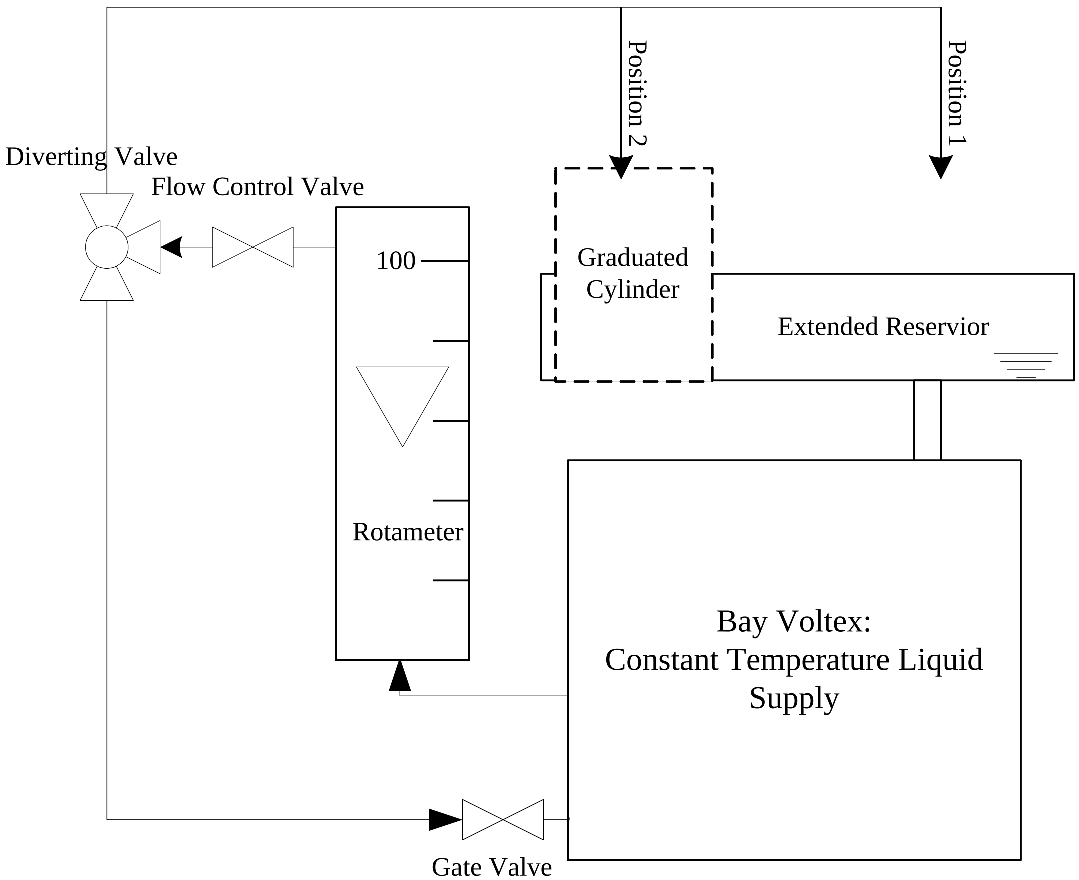

Figure 64. Schematic of rotameter calibration setup

Table 21. Experimental data for rotameter calibration

Average Temperature 24.5°C

Rotameter Scale	Time (s)	L/s	GPM
19.5	113.07	0.03	0.48
30	76.35	0.05	0.71
39.5	58.37	0.06	0.93
49.5	46.97	0.07	1.16
60	38.53	0.09	1.42
69	32.75	0.11	1.67
79	28.09	0.12	1.94
88	25.15	0.14	2.17
96.5	22.66	0.15	2.41

Average Temperature 48.8°C

Rotameter Scale	Time (s)	L/s	GPM
15	142.5	0.02	0.38
24	95.56	0.04	0.57
39.5	58.13	0.06	0.94
48	47.5	0.07	1.15
59	38.87	0.09	1.40
71.5	31.09	0.11	1.75
80	27.56	0.12	1.98
93	23.57	0.15	2.31

Average Temperature 71.3°C

Rotameter Scale	Time (s)	L/s	GPM
17	133.28	0.03	0.41
28	85.1	0.04	0.64
37	63.1	0.05	0.86
46.5	50.16	0.07	1.09
59	39.37	0.09	1.39
72	31.13	0.11	1.75
85.5	25.81	0.13	2.11
94	23.03	0.15	2.37

Average Temperature 84.1°C

Rotameter Scale	Time (s)	L/s	GPM
15.5	148.9	0.02	0.37
26	92.78	0.04	0.59
36	66.34	0.05	0.82
48	48.03	0.07	1.14
60.5	37.88	0.09	1.44
71.5	31.41	0.11	1.74
85	25.91	0.13	2.10
98	22.25	0.15	2.45

Average Temperature 25°C

Rotameter Scale	Time (s)	L/s	GPM
10.5	230.85	0.01	0.23
12	195.16	0.02	0.28
12.5	185.72	0.02	0.29
13.5	163.06	0.02	0.33
15.5	146.63	0.02	0.37
16.5	135.59	0.03	0.40
17	126.56	0.03	0.43
18	119.72	0.03	0.45
20	112.53	0.03	0.48
21	109.37	0.03	0.49
21.5	104.16	0.03	0.52
23	99.66	0.03	0.54
24	95.00	0.04	0.57
25.5	90.84	0.04	0.59
27	86.72	0.04	0.62

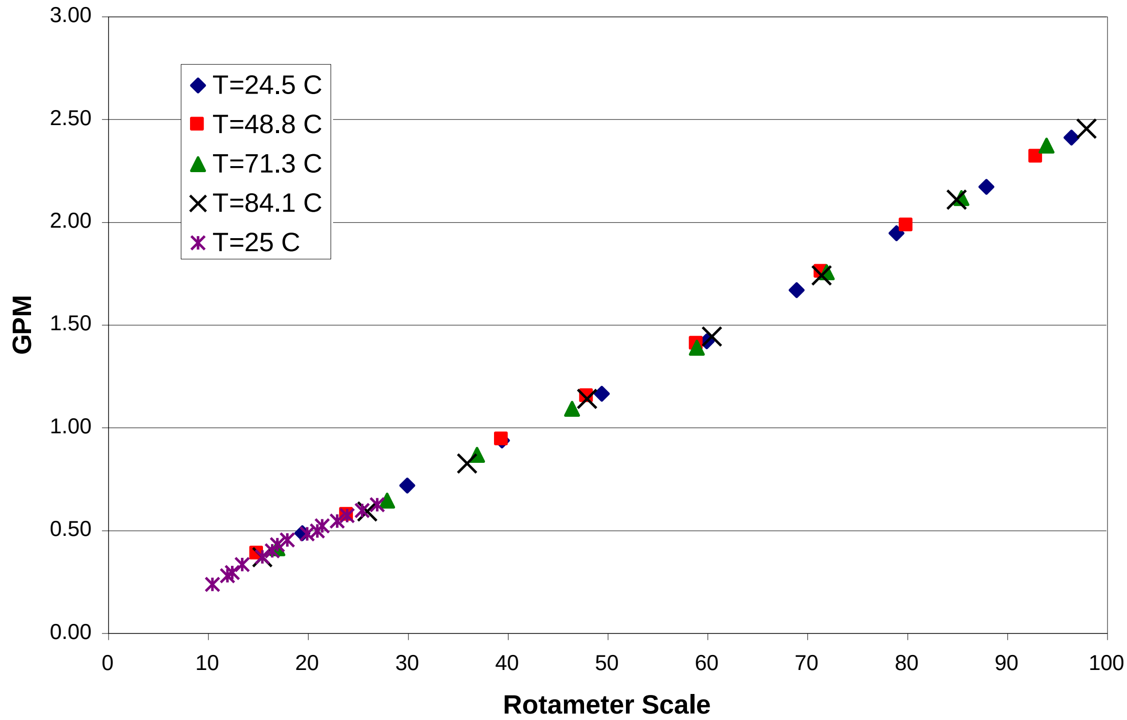

Figure 65. Measured rotameter flow rate at various temperatures

84ºC is 1062 kg/m^3 and 1023 kg/m^3, respectively [25]. Likewise, this calibration closely resembles the rotameter manufacturer's calibration for water because water's density only varies 6% from the density of 50/50 WEG.

Rotameters are typically considered linear devices. The linear regression for the data in Figure 65 is

$$Q = 0.0249(RMR) - 0.0334, \quad R = 0.9993$$

where Q is the flow rate in gallons per minute (GPM), RMR is the rotameter reading, and R is the correlation coefficient.

A.4. Equipment List and Sensor Specifications

SENTRA Differential Pressure Transducer

S/N: 3045719 4306

P/N: 2301002PD2F2DB

Range: 0-2 psi

Excitation: 9-30 VDC

Output: 0.05-5.05 VDC

Accuracy: ±0.25% FSO

Repeatability: 0.05% FSO

KEITHLEY 2700 Multimeter/Data Acquisition [56]

DC Voltage

Range: 1 V

Resolution: 1.0 μV

Accuracy: 0.0025% of reading + 0.0007% of range

Linearity: 0.0002% of reading + 0.0001% of range

Temperature (thermocouples)

Resolution: 0.001ºC

Accuracy: 1ºC

Resistance

Range: 100 kΩ

Resolution: 100 mΩ

Accuracy: 0.0080% of reading + 0.0010% of range

NIST traceable calibration: TMI - 1008924

Omega PX105 Series Pressure Transducer [50]

Excitation: 8-20 VDC

Output: .85-6.25 VDC

Range: 0-25 psi

Linearity: ±0.5 %FSO

Hysteresis: ±0.25 %FSO

Accuracy: ±1 %FSO

Omega Linear Thermistor Composite 44108 [57]

Operating Range: -40 to 150ºC

Resistance: ±1% @ 25ºC

±1% @ 100ºC

Temperature: ±0.2 ºC @ 25ºC

±0.3 ºC @ 100ºC

Thermocouples

Type T, 24-gage, glass insulated

OMEGA #: 5SRTC-GG-T-24-72

Resistors

Kool-Pak Clip Mount Power Film Resistor[53]

Part #: MP2060-1-1

Power Rating: 60 W, 250 V max

1 ohm, 1% tolerance

Film to Case thermal resistance: 2.08°C/W

Operating Temperature: -55 to 150°C

Thermal Grease

Thermalcote 250

Current Probe

Tektronix TCPA400

Amplifier, AC/DC Current Probe

NIST traceable calibration: TMI - B010349

Output: 1 mV/A

Auxiliary Power Supply

Tenma 72-6856 Triple Power Supply 300 W

Adjustable Output: 35 V, 4A

Main DC Power Supply

Xantrex XPR 60-100

Input: 208 3-phase

Output: 60 V, 100 A DC

A.5. Pressure Drop data

Table 22. Reduced pressure drop data for annular duct

Duct Inlet Velocity (m/s)	Pressure drop (Pa)	
	25°C	100°C
0.314	1001.2	
0.298	1028.2	675.2
0.281	951.3	576.7
0.264	828.6	504.0
0.247	730.0	423.6
0.230	651.7	362.1
0.214	576.6	301.5
0.197	481.4	250.6
0.180	426.3	204.1
0.163	365.0	160.4
0.147	312.0	127.4
0.130	250.8	93.2
0.113	206.2	77.3
0.096	166.0	57.9
0.079	129.9	25.4
0.063	136.6	12.1
0.046	101.8	11.5
0.029	84.6	-15.1

Table 23. Reduce pressured drop data for the four-hole duct design

Duct Inlet Velocity (m/s)	Pressure drop (Pa)	
	25°C	100°C
0.488	2459.8	
0.462	2220.5	
0.436	2043.8	1404.2
0.410	1823.6	1254.7
0.384	1663.8	1093.7
0.357	1507.0	926.7
0.331	1314.7	767.1
0.305	1150.1	640.2
0.279	989.3	533.3
0.253	902.7	464.4
0.227	761.0	342.0
0.201	654.1	297.0
0.175	502.8	186.0
0.149	392.0	137.2
0.144	378.6	
0.139	358.3	
0.134	349.9	
0.128	330.6	
0.123	319.0	91.5
0.118	287.8	
0.113	278.5	
0.108	257.3	
0.102	245.1	
0.097	212.2	48.7
0.092	193.2	
0.087	187.4	
0.082	170.5	
0.076	147.8	
0.071	132.5	28.0
0.066	114.0	
0.061	99.5	
0.055	71.3	
0.050	69.8	
0.045	65.6	11.5

A.5. Uncertainty Analysis

The error in the experimental data comes from three main sources: instrumentation error, error in the data collection, and error in the data reduction. In general, the pressure drop in the foam is found by subtracting the pressure difference across the whole channel with no foam from the pressure difference measured across the substrate with foam present for each measured point, *i*.

$$\Delta P_{i,\,foam} = \Delta P_{i,total} - \Delta P(u)_{substructure,\,LS} \tag{35}$$

where $\Delta P_{i,foam}$ is the discrete reduced pressure drop across the foam, $\Delta P_{i,total}$ is the discrete pressure drop measured across the whole substrate with foam, and $\Delta P(u)_{substructure,\,LS}$ is a regression line that was fit to the pressure drop data with no foam after the measured experimental bias was removed. The regression line was subtracted from the total pressure drop data instead of a point-by-point comparison because of large standard deviations in the no-foam data. The total pressure measured across the substrate with foam was corrected by a measured instrumentation bias or offset.

$$\Delta P_{i,\,total} = \Delta P_{i,\,differential} - \Delta P_{offset} \tag{36}$$

To determine the uncertainty in these measurements, the Kline-McKlintock method was used [58]. The uncertainty expressions are given below and categorized by the source of the error.

$$\omega_{\Delta P,\,foam} = \sqrt{\left(\omega_{\Delta P,total}\right)^2 + \left(t_{m,95\%} S_{xy,substructure}\right)^2} \quad \text{data reduction/ data collection} \tag{37}$$

$$\omega_{\Delta P,total} = \sqrt{\left(\omega_{\Delta P,differential}\right)^2 + \left(\omega_{\Delta P,offset}\right)^2} \quad \text{data reduction} \tag{38}$$

$$\omega_{\Delta P,differential} = \sqrt{\left(\omega_{\Delta P,instrument}\right)^2 + \left(t_{m,95\%} S_{\bar{x}}\right)^2} \quad \text{data collection/ instrument error} \tag{39}$$

$$\omega_{\Delta P,offset} = \sqrt{\left(\omega_{\Delta P,instrument}\right)^2 + \left(t_{m,95\%} S_{\bar{x}}\right)^2} \quad \text{data collection/ instrument error} \tag{40}$$

$$\omega_{\Delta P,instrument} = X\sqrt{\left(\omega_{transducer}\right)^2 + \left(\omega_{DMM}\right)^2} \quad \text{instrument error} \tag{41}$$

$$\omega_{transducer} = \sqrt{\left(e_{repeatability}\right)^2 + \left(e_{accuracy}\right)^2} \quad \text{instrument error} \tag{42}$$

$$\omega_{DMM} = \sqrt{\left(e_{linearity}\right)^2 + \left(e_{accuracy}\right)^2 + \left(e_{readability}\right)^2} \quad \text{instrument error} \tag{43}$$

Eqs. (42) & (43) incorporate the reported error in the instrumentation of the digital multimeter (DMM) and in the differential pressure transducer. The manufacturer's specifications are listed for these devices in the Appendix. These errors are based on percentages of the reading and thus vary for each data point. They combine in Eq. (41) to form the total instrumentation error. X in Eq. (41) is the nominal sensitivity of the transducer, 2757.1 Pa/V, to translate the error based on voltage to error in units of pressure. Error in the data manipulation is accounted for in Eqs. (37) - (40). A student t-test is used to find the 95% confidence band of the reduced data [59].

A.6. Addendum to Pressure Drop Experimental Results Analysis

For each duct design the measured pressure drop was divided by the length of the foam section and respective viscosity which was corrected for temperature. These adjusted pressure drops were plotted against inlet velocity. At 25°C a linear portion of the data could be identified for both designs. A linear regression was fit to each section and permeability was found from this portion of each graph by comparison to Darcy's Law. Then, a Darcy-Forchheimer model was developed for the data at 25°C and 100°C. The Forchheimer drag coefficient was adjusted in each case to match the curvature of the respective data. This curve fit led to four drag coefficients which are dependent on the temperature of the fluid. Finally, a small zero offset was adjusted on the experimental data such that the linear regression line crossed the y-axis at 0. This adjustment helps account for error in the original data reduction and allows the model and experimental data to have the same reference point for the nondimensional friction factor.

For the new data reduction method, the same definition of Reynolds number was used for porous media. The expression in Eq. (27) is noted here as a reminder. However, the definition for friction faction has been altered in the new data reduction. Because the Forchheimer drag coefficient is not necessarily constant for differing fluid temperatures, it is now included in the friction factor expression

$$\mathrm{Re}_{pm} = \frac{\rho u C_f \sqrt{\kappa}}{\mu}, \tag{27}$$

$$f_\kappa = \frac{-\nabla p \sqrt{\kappa}}{\rho C_f u^2}. \tag{44}$$

If the Darcy-Forchheimer model is used to express the pressure gradient, the friction factor reduces to:

$$f_{\kappa_{D-F}} = -\frac{\sqrt{\kappa}}{\rho C_f u^2}\left(-\frac{\mu}{\kappa} - \frac{\rho C_f |u|}{\sqrt{\kappa}}\right)u = \frac{\mu}{\rho C_f u \sqrt{\kappa}} + 1 = \frac{1}{\mathrm{Re}_{pm}} + 1. \tag{45}$$

If the Darcy model is used to express the pressure gradient, then the friction factor reduces to:

$$f_{\kappa_D} = -\frac{\sqrt{\kappa}}{\rho C_f u^2}\left(-\frac{\mu}{\kappa}\right)u = \frac{1}{\mathrm{Re}_{pm}}. \tag{46}$$

For the annular duct shape, Figure 66 shows the friction factor results. The reduced data follows the Darcy-Forchheimer model much closer than the original analysis. The permeability is 17% lower than the permeability found in the original analysis. The drag coefficient is 17% lower at 25°C and 14% lower at 100°C with respect to the original parameter.

Figure 67 shows the results for friction factor for the four-hole duct pattern. The changes in permeability and Forchheimer drag coefficients are more significant for the four-hole pattern. The permeability is 51% lower and the drag coefficient is 63% lower at 25°C than the original four-hole flow parameters. The flow in this duct pattern results in Reynolds numbers that extend further to the left into the Darcy flow regime. The data in this region was assumed to be the linear region, which determined the permeability. Since the data does lie in the Darcy region, the assumption proves to be valid.

From the above figures, the Darcy regime contributes to more than 50% of the friction factor up to $\mathrm{Re}_{pm} = 1$. Past this point, the Forchheimer drag term contributes to the majority of the friction factor. The blue lines in both figures denote the maximum allowable inlet velocity for the two duct designs at 105°C. Because of the lower permeability, the four-hole operational point is further to the left as compared to the annular duct operational point. The Reynolds number at this point is 0.83, which implies the form drag is not as dominant as the viscous drag. The Reynolds number for the annular duct at maximum allowable operation is 1.44, which implies the form drag is the dominant pressure drop term. In all cases, it appears that the Darcy-Forchheimer model with the new parameters detailed in Table 14 will adequately describe the flow field behavior.

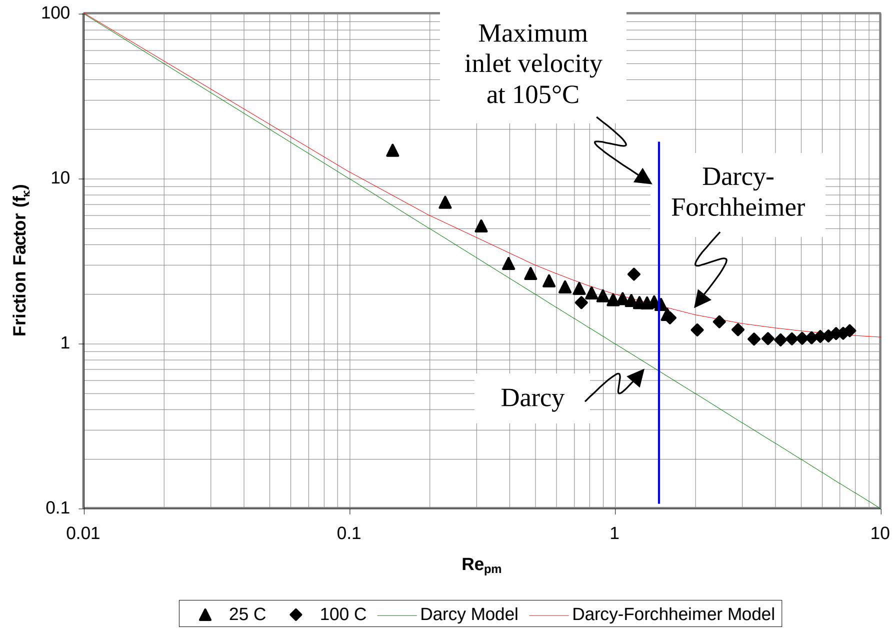

Figure 66. New friction factor results for annular duct, $\kappa = 7.97\text{x}10^{-8}$ m^2, $C_{f,25°C} = 0.060$, $C_{f,100°C} = 0.062$

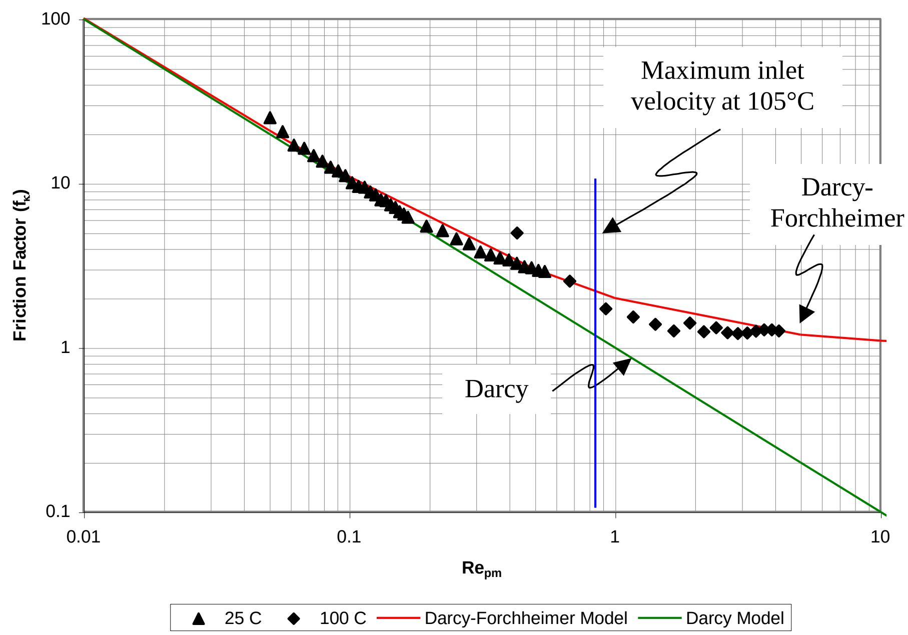

Figure 67. New friction factor results for four-hole duct pattern, $\kappa = 3.22\text{x}10^{-8}$ m^2, $C_{f,25°C} = 0.021$, $C_{f,100°C} = 0.036$

A.7. Measured Data from Thermal Model Validation

Table 24. Measure thermal data from annular duct design

Measured Electrical Power	Measured Heat Added	Adjusted Heat Addition/ COMSOL Input	Inlet Temperature	Average Experimental Temperature ©	
				Case	Flat
0.0	-80.0	0.0	104.4	94.8	98.2
180.3	79.9	159.9	104.6	130.8	114.7
210.4	106.5	186.5	104.7	137.7	117.7
0.0	-77.2	2.8	104.4	95.3	98.6
0.0	-54.6	0.0	89.8	82.2	85.0
294.9	184.1	238.8	90.9	145.9	114.3
0.0	-36.6	0.0	75.4	70.0	72.0
332.3	217.0	253.5	76.8	142.1	106.1
0.0	-23.7	0.0	51.3	48.2	49.3
331.3	226.3	250.0	52.4	119.4	85.4

Table 25. Measured thermal data for four-hole duct design

Measured Electrical Power	Measured Heat Added	Adjusted Heat Addition/ COMSOL Input	Inlet Temperature	Average Experimental Temperature ©			
				1	2	3	4
0.0	-3.1	0.0	49.8	46.8	48.9	47.2	47.6
329.8	235.0	238.1	51.4	97.3	77.6	106.7	88.9
0.0	-4.3	-1.2	49.9	47.5	49.1	47.8	47.4
0.0	-35.2	0.0	90.1	87.0	87.0	80.6	82.0
181.1	111.1	146.3	90.9	101.8	101.8	113.6	105.0
330.7	221.8	257.1	90.5	112.2	112.2	141.0	123.4
0.0	-34.3	0.9	89.5	87.2	87.2	82.5	83.5
0.0	-37.2	0.0	104.0	91.9	100.5	93.2	94.7
84.5	39.0	76.3	104.2	104.0	107.0	107.9	104.8
121.7	65.4	102.6	104.4	109.1	109.7	114.2	109.2
211.1	141.0	178.2	104.6	121.9	116.3	129.9	120.1
270.5	192.7	230.0	104.8	131.3	120.8	141.7	128.3

A.8. Manifold Design

Four basic flow patterns were considered for the linear manifold design. All had inlet and outlet ports with a nominal size of 1". The position of these ports was altered to find the most even distribution of flow to the six half leg modules. The spacing of the modules in the manifold was dictated by the electrical layout. The four designs are described as:

1. End ports – inlet and outlet port are located on opposite ends (Figure 68). Mean free path of fluid through all six modules is equal.
2. Axial aligned ports – inlet and outlet port are positioned on the top and bottom of the manifolds (Figure 69). The ports are also in-line with the axial direction of the modules. Centerline of the ports is also aligned.
3. Axial aligned ports with diffuser plate – ports are in same physical position of manifold design 2 (Figure 70). The inlet manifold has an internal plate with small holes to create two chambers to even out the pressure distribution before entering the modules.
4. Side ports – inlet and outlet port are located in the middle of the long side of the manifold (Figure 71). They are oriented 90° to the axial direction of the modules. Flow impinges on flat wall to redistribute before flowing through modules.

The multi-physics modeling software COMSOL was also used to simulate the flow in the inlet and outlet manifold. The quality of the subsequent solutions was evaluated on their ability to balance the overall flow rate in the system and within each individual porous channel.

The annular shape was used exclusively in these simulations. At the time of this work, the experimental data was not complete. The annular channel had shown the most promise from the simulations and was favored for further investigation.

With a system flow rate of 2.5 GPM, the flow is turbulent in the inlet and outlet ducts of the system. The Reynolds number based on an inlet duct diameter of 1" is greater

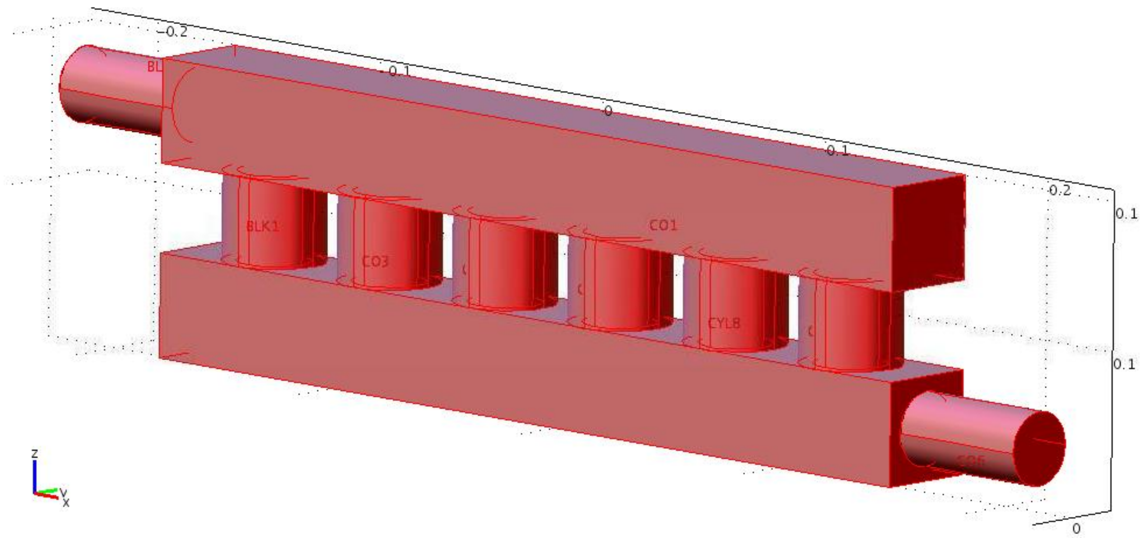

Figure 68. Design 1 - End port manifold

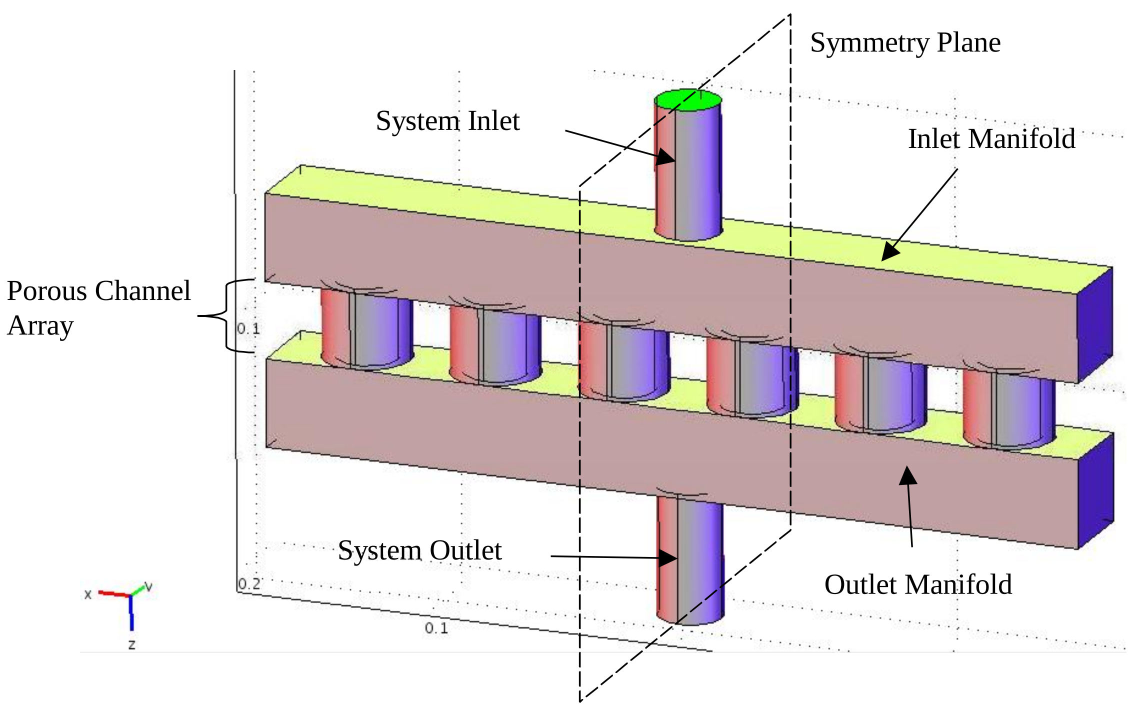

Figure 69. Design 2 – Axial aligned port manifold

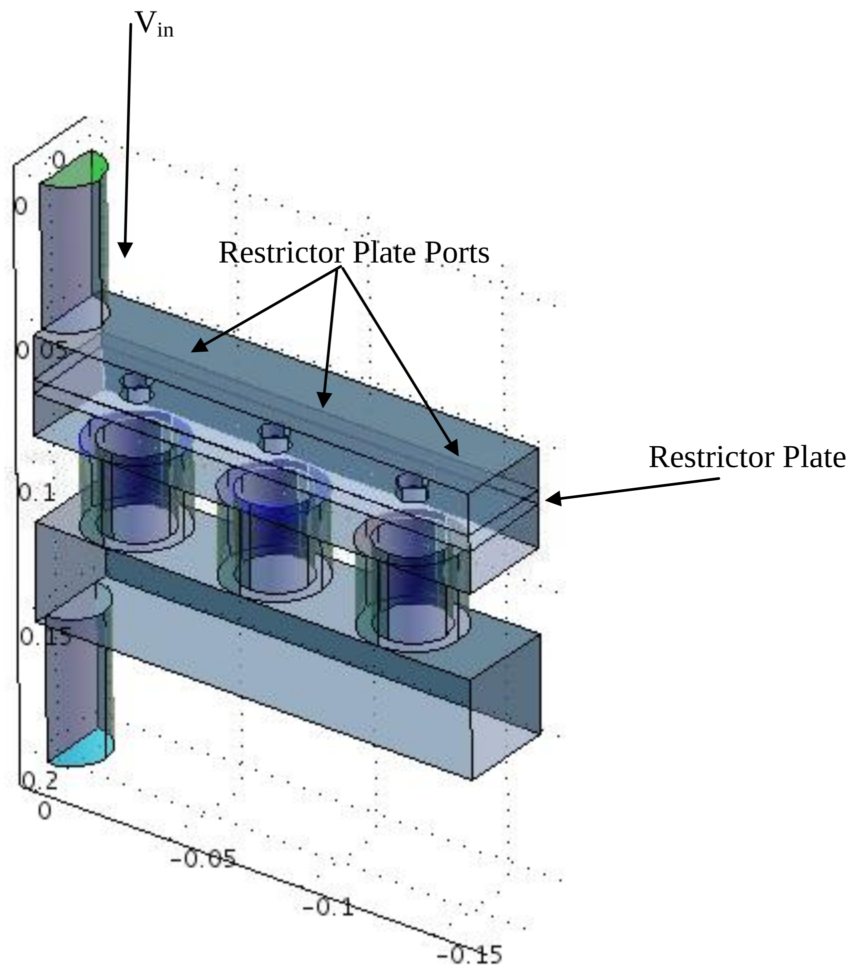

Figure 70. Design 3 – Axial aligned port manifold with diffuser plate

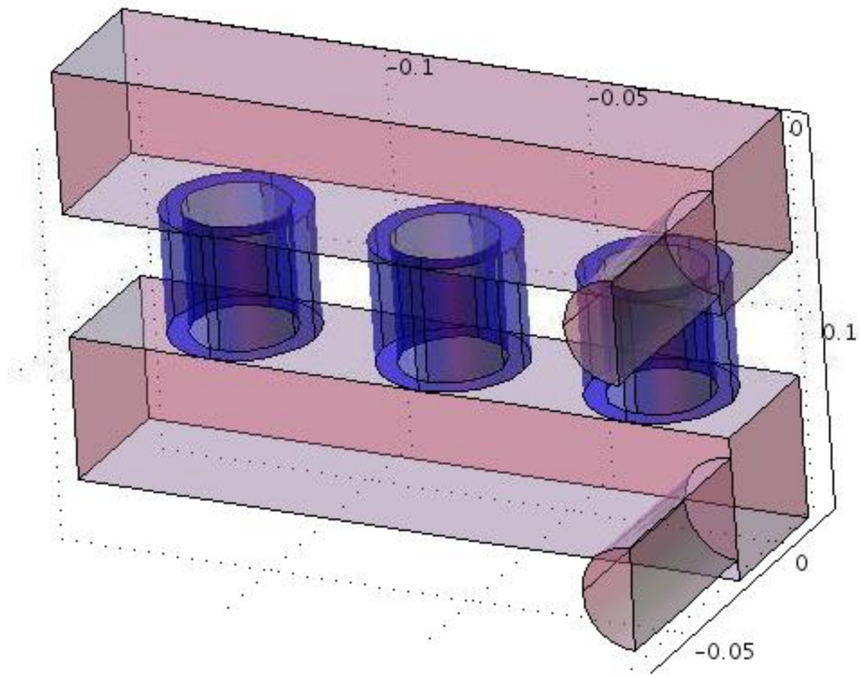

Figure 71. Design 4 – Half symmetry of side port manifold

than 13,000. A Reynolds number of 2300 marks the limit on laminar flow and transition to turbulence. However, the Reynolds averaged Navier-Stokes (RANS) equation set used for turbulence modeling in COMSOL does not present an obvious way to incorporate porous media effects. That being the case, the models presented here use the laminar incompressible Navier-Stokes equations, $Re_D < 2300$, where the effects of the porous media are readily implemented. Further investigation is necessary to determine the most effective way of implementing porous media conditions in the RANS equation set.

Even though the flow within the inlet port is turbulent at maximum flow, the flow within the porous channel is laminar. At maximum inverter flow, the Reynolds number for the annular channel based on hydraulic diameter is 942. Thus, the laminar model is valid for the flow through the porous media. If RANS could be coupled with the porous models, the turbulent model in the free stream would add to the overall pressure drop. Since a significant part of the overall drag, and hence the pressure drop, is presented by the porous media, the turbulent addition would only be small. Thus, the laminar model should provide adequate results for the overall flow distribution.

The incompressible Navier-Stokes (INS) equation set in COMSOL readily yields the Brinkman relation that incorporates the viscous shear effects into Darcy's model. For this study on manifold design, the values used for porosity (ε) and permeability (κ) were 0.90 and 1E-8 m^2, respectively. At this point in the research, solution methods for smaller permeabilities in the Forchheimer model had been obtained, but the reduced data from the pressure drop experimentation was not yet available. Eq. (24) was used to determine the Forchheimer drag coefficient and yielded a value of 0.167 for a porosity of 0.90. This value is on the high end of others reported in literature when compared to values in Table 13.

Even though a convergence strategy for obtaining solutions that incorporate the Forchheimer drag contribution had been developed, it applied to simple geometries. The full three-dimensional models, which are developed for the manifold modeling, present new challenges. In some of the cases presented, the analysis was limited to Navier-Stokes solutions. Much work is still required to obtain converged, mesh-independent solutions for full three-dimensional porous media models that couple free flow and Brinkman-Forchheimer flow.

Design 1 – End Port Manifold

The Navier-Stokes solution was the only converged solution for this manifold design. The inlet jet had a tendency to push more fluid toward the channels closer to the outlet port. The unevenness in the free flow balance makes drastic changes by the porous media unlikely.

In an alternate scheme not pictured, the outlet could be placed on the same end as the inlet (bottom left of Figure 68). This location would provide a path of least resistance in the porous channel closest to the inlet, which would create even more non-uniformity in flow distribution. This design was not given any further consideration based on this argument.

Design 2 – Axial Aligned Port Manifold

The main issue encountered in this design was the spread of the jet as it struck the wall normal to the inlet flow. The abrupt change in fluid momentum at the wall tends to jet the fluid into the center channels. The high velocities captured in the inner channel near the plane of symmetry are a result of direct feeding of the flow into that portion of the channel. An 8% variation existed between the central channels and the outer channels. The pressure drop across the entire design is small because of the low inlet velocity, $\Delta P = 11$ Pa. However, the pressure drop across the foam channel is 92% of the total pressure drop. This result supports the statements made earlier to justify the laminar models.

Design 3 – Axial Aligned Port Manifold with Diffuser Plate

For an improvement on Design 2, a restrictor plate was constructed at the mid-plane of the inlet manifold. This design restricts the flow to impinging on the solid plug in the center of each porous channel. Assuming that the fluid spreads evenly from its impact point on the solid plug of the porous channel, the flow into the channel from this point should be uniformly distributed. Coarse mesh Navier-Stokes solutions were obtained to acquire very rough estimations of the overall behavior of the fluid's interaction with the restrictor plate. Just as observed in Design 2, the flow diverges at the restrictor plate and favors the inner ports. It was determined that the ports in the restrictor plate needed to be smaller at the center channels and larger toward the outer channels.

While the concept seems as though it will sufficiently satisfy the design requirements, no reliable solution with the inclusion of porous media has been obtained thus far. Likewise no pressure drop data is available to report.

Design 4 – Side Port Manifold

This design has favorable packaging attributes. Since the flow enters and exits the manifold on one side only, the electronics may be isolated from potential exposure to liquid. The inlet flow impinges on the opposing side of the manifold; however, the flow does not force itself directly into the porous media channels. More room exists for the flow to even out prior to entering the annular regions.

When modeled, the same unbalance in the center channels was encountered in this design as was observed in Design 2. The benefit of this design is in its computational stability. This model has been refined to produce accurate results relative to the criteria mentioned earlier. Unlike Design 2, the integrated flow rate at the inlet plane of the porous channels was relatively uniform despite the high local velocities observed at the porous media inlet plane. This uniformity was observed over a parametric sweep of the inlet Reynolds number.

The integrated porous channel flow rate fell within 2.3% of the design criteria for each porous channel during the parametric study. For this design, the pressure drop across the foam section accounted for 88% of the total pressure drop of 25 Pa. Again, this large percentage of pressure drop across the foam section helps to show that laminar models should yield initial conclusions that can be extended to turbulent flow with some confidence.

Conclusions

The position of the system outlet relative to the inlet is important is balancing the flow among porous channels. The best design among the four explored was Design 4. This design resulted in the most conclusive modeling and showed that the flow rate through each channel was well balanced. The porous media evenly redistributes any inlet velocity deviations within each channel. This design also fits well with the overall inverter packaging scheme. It allows for the fluid to enter and exit in close proximity such that the fluid may be isolated for other electronic components.

Vita

Kirk Townsend Lowe was born in Kingsport, TN, on August 5, 1981. Raised in Kingsport, Kirk attended Thomas Jefferson Elementary School and Ross N. Robinson Middle School. He graduated as salutatorian from Dobyns-Bennett High School in 2000. Kirk pursued his Bachelor's of Science in Mechanical Engineering at the University of Tennessee in Knoxville, TN. He graduated *summa cum laude* with his degree in 2004. During these studies, he worked as a co-op student with Shaw Industries in Dalton, GA, and an undergraduate research assistant at Oak Ridge National Laboratory's National Transportation Research Center (NTRC) in Knoxville.

Kirk continued his graduate education at the University of Tennessee in Knoxville while maintaining his research assistantship at NTRC. He will receive his Doctor of Philosophy degree in Mechanical Engineering in December 2009.

Kirk plans to join the research staff at Bettis Atomic Power Laboratory in Pittsburgh, PA, as a senior design engineer in early 2010.